Max-Planck-Institut für Meteorologie
Max Planck Institute for Meteorology

Sea Level and Hydrological Mass Redistribution in the Earth System: Variability and Anthropogenic Change

Felix Landerer

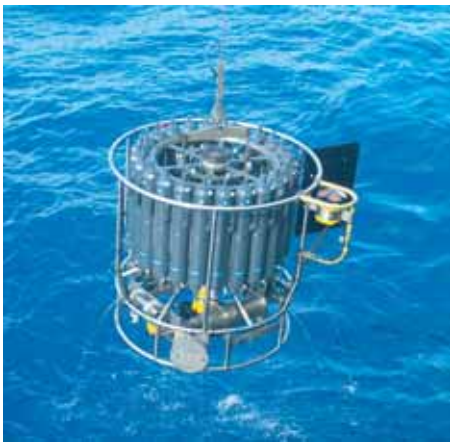

Berichte zur Erdsystemforschung 47/2007

Reports on Earth System Science

Hinweis

Die Berichte zur Erdsytemforschung werden vom Max-Planck-Institut für Meteorologie in Hamburg in unregelmäßiger Abfolge herausgegeben.

Sie enthalten wissenschaftliche und technische Beiträge, inklusive Dissertationen.

Die Beiträge geben nicht notwendigerweise die Auffassung des Instituts wieder.

Die "Berichte zur Erdsystemforschung" führen die vorherigen Reihen "Reports" und "Examensarbeiten" weiter.

Notice

The Reports on Earth System Science are published by the Max Planck Institute for Meteorology in Hamburg. They appear in irregular intervals.

They contain scientific and technical contributions, including Ph. D. theses.

The Reports do not necessarily reflect the opinion of the Institute.

The "Reports on Earth System Science" continue the former "Reports" and "Examensarbeiten" of the Max Planck Institute.

Anschrift / Address

Max-Planck-Institut für Meteorologie
Bundesstrasse 53
20146 Hamburg
Deutschland

Tel.: +49-(0)40-4 11 73-0
Fax: +49-(0)40-4 11 73-298
Web: www.mpimet.mpg.de

Layout:

Bettina Diallo, PR & Grafik

Titelfotos:
vorne:
Christian Klepp - Jochem Marotzke - Christian Klepp
hinten:
Clotilde Dubois - Christian Klepp - Katsumasa Tanaka

Berichte zur Erdsystemforschung 47/2007

Sea Level and Hydrological Mass Redistribution in the Earth System: Variability and Anthropogenic Change

Dissertation zur Erlangung des Doktorgrades der Naturwissenschaften
im Departement Geowissenschaften der Universität Hamburg
vorgelegt von

Felix Landerer
aus Berlin

Hamburg 2007

Reports on Earth System Science 47/2007

ISSN 1614-1199

Felix Landerer
Max-Planck-Institut für Meteorologie
Bundesstrasse 53
20146 Hamburg
Germany

Als Dissertation angenommen
vom Departement Geowissenschaften der Universität Hamburg

auf Grund der Gutachten von
Prof. Dr. Jochem Marotzke
und
Prof. Dr. Jürgen Sündermann

Hamburg, den 13. Juli 2007
Prof. Dr. Kay-Christian Emeis
Leiter des Departements für Geowissenschaften

ISSN 1614-1199

Sea Level and Hydrological Mass Redistribution in the Earth System: Variability and Anthropogenic Change

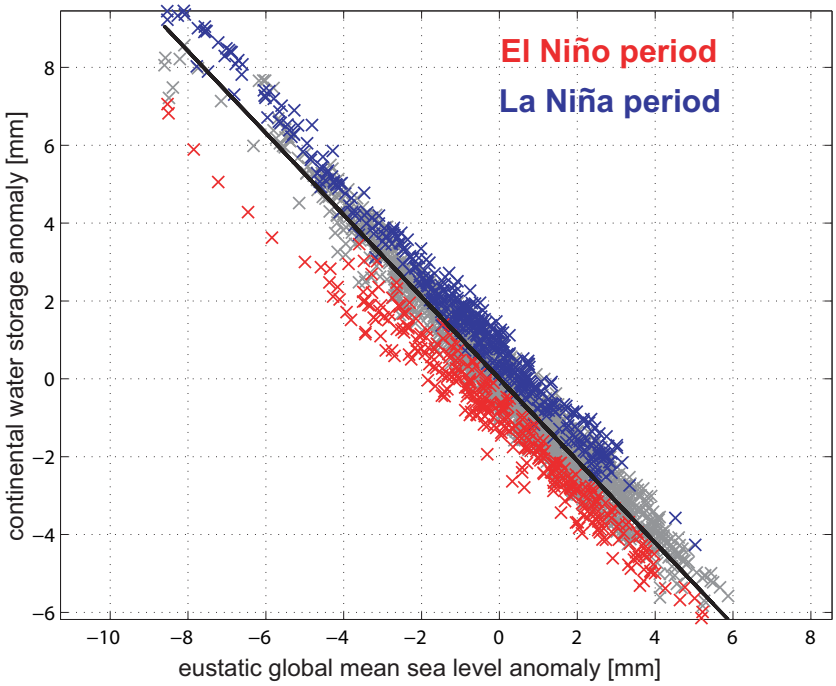

Felix Landerer

Hamburg 2007

Abstract

In this thesis, I use simulations with a coupled climate model to examine the geophysical mechanisms and implications of natural and anthropogenic sea level changes.

I find that eustatic sea level variability is mainly balanced by continental water storage. The correlation with the El Niño–Southern Oscillation (ENSO) is not significant for eustatic sea level, weakly significant for continental water storage and steric sea level, and strongly significant for atmospheric water vapor content. Large changes in eustatic sea level and continental water storage can occur concurrently with individual ENSO events, but the sign and amplitude vary depending on large-scale precipitation patterns. The low-degree harmonics of the global geoid (C_{21}, S_{21}, C_{20}), which are linked to the Earth rotation vector (C_{21}, S_{21}: polar motion; C_{20}: length-of-day), show a mixed response to the global water mass load anomalies. Correlation with ENSO is significant for S_{21}, with dynamic ocean bottom pressure and soil moisture variability as the main causes. Correlation with ENSO is also significant for C_{20}, with soil moisture and atmospheric loading variability as the main causes. Correlation with ENSO is not significant for C_{21}.

In the simulated warming climate, sea level rise is strongest in the Arctic Ocean due to enhanced fresh water input. Changes in sea level are weakest in the Southern Ocean due to a partial compensation between dynamic and steric sea level changes. A complex tripole pattern of anomalous sea level in the North Atlantic Ocean correlates highly with the combined subtropical and subpolar baroclinic gyre transport, but only weakly with the slowly decreasing meridional overturning circulation (MOC). Therefore, observations of North Atlantic sea level cannot be utilized for robust monitoring of MOC changes.

A distinct pattern of ocean bottom pressure changes emerges with ocean thermal expansion: mass is redistributed within the ocean such that bottom pressure increases over shallow shelf areas, and decreases over deep ocean areas. A newly developed conceptual redistribution model explicitly links steric sea level to ocean bottom pressure changes through horizontal mass redistribution without changing the total ocean mass. The simulated net movement of mass closer towards Earth's axis of rotation leads to a decreasing length-of-day with rising steric sea level. Since the mass redistribution is not rotationally symmetric, significant polar motion is also excited. The polarization of this simulated polar motion is similar to the polarization of observed decadal polar motion. However, polar motion inferred from observed thermal expansion over the last 50 years is too small to account for the observed polar motion over the last 50 years, suggesting that other mechanisms play an important role in exciting decadal polar motion. Nonetheless, my results demonstrate that the oceans are capable of exciting nontidal polar motion and length-of-day signals on decadal and longer periods.

Contents

Sea level is important as a metric for climate change as well as in its own right. We are in the uncomfortable position of extrapolating into the next century without understanding the last. (Munk, 2002)

1 Introduction

1.1 Motivation

Sea level varies on a wide range of time-scales, and due to a variety of processes. Large changes of the global mean sea level are intimately linked to shifts in the mean climate state - for example, since the Last Glacial Maximum about 20000 years ago, sea level has risen by over 120 m due to the melting of large ice sheets (Church et al., 2001). During the last 6000 years global mean sea level has varied on centennial time scale by less than 0.3 to 0.5 m based on geological data (Church et al., 2001). Based on global reconstructions of tide gauge measurements, average sea level has risen 1.7 ± 0.3 mm yr^{-1} in the 20th century (Church and White, 2006). This change is due both to an increase of the total ocean mass, e.g., from glacial melting, and to a decrease of the mean ocean density, e.g., mean warming or freshening of the ocean. However, independent observations of the individual climate contributions to sea level fall short of the total observed 20th century signal by about 0.7 ± 0.7 mm yr^{-1} (Solomon et al., 2007). The observed sea level rise for the recent decade of 1993 to 2003 is 3.1 ± 0.7 mm yr^{-1}, and for this period the observed sea level rise and the observed individual contributions agree to within known errors, with changes in ocean mass and ocean density contributing about equally to the signal. However, it is not clear whether the recent faster rate reflects natural variability, or an increase of longer-term trends (Solomon et al., 2007).

In face of anthropogenic climate change, it is expected that the oceans will take up a large fraction of the heat added to the climate system. Water has a heat capacity that is about three orders of magnitude larger than air (e.g., Gill, 1982), and it is estimated that since 1955, ocean warming has accounted for more than 80% of the changes of the energy content in the climate system (Solomon et al., 2007). As the oceans warm, their density decreases and thus their volume increases, without changing the total ocean mass. This process is referred to as steric sea level rise, its rate depending largely on the rate at which heat is removed from the surface layers into the deeper ocean. Thus, steric sea level change is also a very important measure of the change in total energy content of the Earth's climate system. As anthropogenic warming is projected to continue into the decades and centuries to come, it will also likely influence sea level through changes of the

total ocean mass by adding or removing water from the oceans. This process is referred to as eustatic sea level change (e.g., Cazenave and Nerem, 2004). While the current mass balance of mountain glaciers and the Greenland ice sheet suggest a contribution to sea level rise, the case for the Antarctic ice sheet is less clear (Solomon et al., 2007).

Steric and eustatic sea level also vary naturally on seasonal to decadal time-scales. For example, models and observations agree that volcanic eruptions typically lead to a rapid significant cooling and hence falling steric sea level, and the subsequent recovery over years to decades can significantly affect other long-term trends (Church et al., 2005). Observations of ocean heat content also suggest considerable interannual to decadal variability, but climate models typically exhibit much less variability of ocean heat content. It is not clear if this is a shortcoming of the models, or a problem of too few hydrographic observations (Gregory et al., 2004). Eustatic sea level also varies naturally on seasonal to decadal time-scales, because water can be stored very effectively on land in the soil, as groundwater, or as snow (Cazenave and Nerem, 2004). Eustatic sea level change thus also reflects variability of the large-scale hydrological cycle.

The determination of anthropogenic sea level trends in observations obviously requires knowledge about the processes and mechanisms that drive natural sea level variability, as well as the typical time-scales and amplitudes involved. The socioeconomic importance of sea level change is evident considering that as of 1998, over half the population of the planet - about 3.2 billion people - lived and worked in a coastal strip just 200 kilometers wide (Hinrichsen, 1998).

1.2 Observation and Simulation of Sea Level Change

Before the advent of high-precision satellite altimetry in the early 1990ies, sea level changes were determined from tide gauge measurements, but their geographically sparse distribution and location close to land most likely introduced some serious bias into these measurements, such that local corrections due to relative tectonic movement must be done carefully to yield useful estimates of sea level change (Cazenave and Nerem, 2004). Sea level observations with satellite altimetry overcame this problem, and now measure local sea level with a near global coverage. Local sea level as such is merely a diagnostic measure of a variety of physical processes. The local gradient of the sea surface height is dynamically linked to large-scale oceanic flow through the geostrophic balance. Thus, changes of the local sea surface height gradient reflect changes of the large scale oceanic flow (e.g., Gill, 1982), and the detection of regional sea level change provides in principle an easy measure of an otherwise hard to obtain ocean state. Model simulations suggest that projected sea level change is geographically highly non-uniform, reflecting the geo-

graphically varying density changes and ocean circulation changes (Church et al., 2001). Regionally, the deviation from the global mean sea level change can be well over 100% for current rates of global mean changes (Cazenave and Nerem, 2004; Church et al., 2001). Obviously, knowledge of potential regional sea level change is of great importance for coastal planning when considering regional coastal impacts of sea level rise. The most recent simulated patterns of sea level change from different models have now more similarity than in previous comparisons of climate change projections (e.g., Church et al., 2001), but considerable differences between models remain. Interannual variability is one possible explanation (Solomon et al., 2007).

The nature of a global mean sea level change (steric or eustatic) cannot be determined from measuring sea level alone. Whether a sea level signal is of steric or eustatic origin must be determined from direct measurements of either one. Determination of steric changes in principle require the sampling of temperature and salinity in the ocean in four dimensions (three in space, one in time), and eustatic changes require in principle a 'weighing' of the total ocean.

In terms of hydrographic temperature and salinity profiles, the global ocean is notoriously undersampled, both in space and in time. Especially the southern hemisphere and the deep ocean in general suffer from a lack of observations, and it has been suggested that the undersampling overestimates global mean steric sea level variability, since ocean models do not agree with observation in this respect (Gregory et al., 2004). Of course, it cannot be ruled out that models lack important dynamic aspects and simply underestimate oceanic heat content variability (Gregory et al., 2004). In terms of ocean mass changes, this metric can be achieved by measuring and inverting changes of Earth's geopotential field. This strategy is pursued with the Gravity Recovery and Climate Experiment (GRACE) satellite mission (Chambers et al., 2004), which has been under way since 2003 (Tapley et al., 2004). However, the geoid is an equipotential surface that integrates a variety of other geophysical processes, both on and below Earth's surface, and these other processes must be subtracted (either from observations or models) before making any inference about ocean mass change from gravity data.

Independent constraints on sea level change come from astronomic observations. Melting of glaciers and large ice sheets (and the corresponding eustatic sea level rise) can effectively cause changes in Earth's moment of inertia (Eubanks, 1993). With the requirement that the total nontidal angular momentum of the Earth must be conserved, changes in the moment of inertia are balanced by corresponding changes of Earth's angular velocity, effectively measured as the length-of-day (LOD). If the surface mass redistribution is not rotationally symmetric, this would additionally result in a movement of the pole of rotation (polar motion, PM) such that equatorial oblateness is maximized (Munk, 2002). Changes

in Earth rotation are indirectly linked to changes in Earth's geopotential field. Specifically, the degree-two geopotential Stokes coefficients are very important because they are linked to polar motion and length-of-day (e.g., Chao, 1994), effectively providing two independent methods to determine large-scale mass redistribution in the Earth system. As such, Earth rotational constraints have typically been associated with eustatic sea level signals (Chao, 1994). As noted by Munk (2002), the observations of steric and eustatic sea level change are in conflict with the astronomic observations: either steric sea level change is severely underestimated, traditional estimates of sea level change (steric and eustatic) are too high, the astronomic constraints on the eustatic rise are not valid, or any one combination of these points (or none). This discrepancy has been recognized as the 'sea level enigma' (Munk, 2002).

Since observational estimates of sea level change and their Earth rotational implications lead to apparently contradictory results, it is essential to understand the physical processes involved, both in terms of natural variability and anthropogenic forcing. 'Sea level' involves all components in the Earth system, because water is exchanged between the oceans, atmosphere and continents on all time-scales. Fully coupled climate models are the tool of choice for simulating and studying sea level change as an essential step toward resolving the enigma. The ECHAM5/MPI-OM Earth system model used here does not require flux adjustments, has sufficiently high resolution, and includes a land surface and run-off scheme, which allows for a realistic simulation of the large-scale climate, both in the ocean and in the atmosphere. Of course, no model is perfect. The simulated climate state must be continuously checked against observations for consistency. Not only will this lead to better models, but one may hope to gain knowledge along the way (Müller and von Storch, 2004). I would like to point out here that the current knowledge of ice sheet dynamics is still very limited, so that neither the Greenland nor Antarctic ice sheet are dynamically coupled in ECHAM5/MPI-OM, effectively excluding cryospheric variability from this study.

1.3 Thesis Objective

The objectives of this thesis arise from the open issues and questions in terms of sea level change noted in the previous section. With the Earth system model ECHAM5/MPI-OM as a tool, I investigate the following research questions in this thesis:

Natural Variability

- Can a fully coupled climate model simulate the observed seasonal cycling of water between the oceans, atmosphere and continents?

- Can the El Niño-Southern Oscillation (ENSO) as an important, large-scale coupled ocean-atmosphere mode, generally be associated with a sea level change, and if so, does this sea level anomaly have an eustatic contribution and how is it balanced? What is the ENSO-related water budget of the continents and atmopshere?

- Can hydrological mass redistribution from the El Niño-Southern Oscillation generally be associated with a significant degree-two geopotential signal, and if so, what are the geographical patterns and contributions in the atmosphere and on the continents that lead to this anomaly?

Anthropogenic Signals

- What are the dynamic processes that lead to the projected geographical pattern of sea level change? In particular, in light of an expected slow down of the meridional overturning circulation (MOC) in the North Atlantic under anthropogenic warming (e.g., Marotzke, 2000), can the observation of regional sea level change in the North Atlantic be utilized to detect changes of the MOC?

- What is the horizontal and vertical structure of the contribution to steric changes? How do temperature and salinity contribute to this structure, and what mechanisms are involved?

Earth Rotational Signals

- Does the simulated sea level change under the IPCC-A1B scenario lead to detectable signals in ocean angular momentum such as Polar Motion and Length-of-Day? What mechanisms of mass redistribution in the ocean are involved? Can this at least partially resolve the 'sea level enigma'?

1.4 Thesis Outline

The thesis is structured into four chapters, two of which have been published already, while the other two are in preparation for journal submission. Each chapter aims at answering a subset of the *Research Questions* brought up in the previous section. This structure implies that each chapter can be read largely independently from the others; it also implies some recurrence of the contents, as each chapter contains its own introduction and description of pertinent model features and underlying theory.

- **Chapter 2** deals with seasonal and ENSO-related sea level variability and the associated hydrological mass redistribution. I analyze monthly values from 200 years

simulated with ECHAM5/MPI-OM, with no anthropogenic forcing present ('control run'). The analysis involves steric and eustatic sea level, dynamic ocean bottom pressure, continental water storage in the soil and as snow, and atmospheric water vapor and surface pressure. I use a lagged linear regression of monthly anomalies of all terms to determine their coupling with ENSO, and analyze the geographical patterns that evolve with ENSO. Finally, I calculate the individual as well as total degree-two geopotential signal of ENSO-related mass redistribution, and compare the results with observed signals. This chapter is in preparation for submission to *Journal of Geophysical Research*[1].

- In **Chapter 3**, I evaluate the simulated pattern of regional dynamic and steric sea level change in response to anthropogenic climate change as given by the IPCC-A1B scenario. In particular, I assess the relationship between sea level changes in the North Atlantic and the Atlantic meridional overturning circulation. Also, I calculate the pattern of steric sea level changes for temperature and salinity changes separately, examining the role of each and the processes that cause the response. This chapter has been published in *Journal of Physical Oceanography*[2].

- **Chapter 4** deals with ocean bottom pressure changes that evolve in the IPCC-A1B scenario. I derive a novel simple conceptual model that links ocean steric sea level changes to horizontal mass redistribution. I compare the simple conceptual model to the simulated pattern of bottom pressure changes, and I determine the implications for the length-of-day. This chapter has been published in *Geophysical Research Letters*[3].

- In **Chapter 5**, I extend the results of **Chapter 4** and examine the influence on Polar Motion by the pattern of simulated bottom pressure changes in a warming ocean. Additionally, I calculate relative ocean angular momentum changes due secular changes of the large-scale ocean circulation in the IPCC-A1B scenario. This chapter is in preparation for submission to *Geophysical Research Letters*[4].

- In **Chapter 6**, I summarize the main results of this thesis, and conclude with a brief discussion of possible future research developments from a modelling point of view

[1] Landerer, F. W., J. H. Jungclaus, and J. Marotzke, 2007: Non-Seasonal Variability in Sea Level, Hydrological Mass Redistribution, and Degree-Two Geoid Coefficients. *J. Gephys. Res.*, in preparation

[2] Landerer, F. W., J. H. Jungclaus, and J. Marotzke, 2007: Regional dynamic and steric sea level change in response to the IPCC-A1B scenario. *J. Phys. Oceanogr.*, **37**, 296-312

[3] Landerer, F. W., J. H. Jungclaus, and J. Marotzke, 2007: Ocean Bottom Pressure Changes Lead to a Decreasing Length-of-Day in a Warming Climate. *Geophys. Res. Lett.*, **34**, L06307, doi:10.1029/2006GL029106

[4] Landerer, F. W., J. H. Jungclaus, and J. Marotzke, 2007: Polar Motion and Length-of-Day: Expected Signals from the Warming Oceans. *Geophys. Res. Lett.*, in preparation

in the field of sea level change and hydrological mass redistribution in the Earth system.

2 Non-Seasonal Variability in Sea Level, Hydrological Mass Redistribution, and Degree-Two Geoid Coefficients

Abstract

We use 200 years of monthly data from a state-of-the-art coupled atmosphere-ocean general circulation model (AOGCM) to assess El Ninño-Southern Oscillation (ENSO) related climate variability of steric and eustatic sea level, hydrological mass redistribution, and the corresponding signals in the degree-two geoid coefficients (Stokes coefficients). The simulated seasonal cycle of eustatic and hydrological mass redistribution agrees very well with observed estimates; the simulated seasonal cycle of steric sea level is only about 75% that of the observed. The seasonal cycle removed, we then use lagged-regression analysis to find the relation of the non-seasonal anomalies with ENSO. Steric sea level varies significantly in phase with ENSO, but there is considerable interannual to decadal variability that cannot be linked to ENSO. We find that eustatic sea level is not significantly linked to ENSO, continental water storage has a weak signal with ENSO, and the atmospheric water vapor content is strongly linked to ENSO variability. However, due to the limited atmospheric water storage capacity, most non-seasonal eustatic sea level variability is balanced by continental water storage. Thus, we find large changes in eustatic sea level (up to 7 mm over 3 years) and continental water storage concurrently with some of the simulated ENSO events, but the sign and amplitude vary depending on the anomalous location of the large-scale precipitation over the oceans or over land. In this way, there is no systematic response of eustatic sea level to ENSO. Based on the geographical distribution pattern of non-seasonal water mass load anomalies, we find significant ENSO related variability in the S_{21} and C_{20} Stokes coefficients, but not a significant change in C_{21}. For S_{21}, the anomaly patterns of dynamic ocean bottom pressure and soil moisture are the main contributors to the combined signal; for C_{20}, the anomaly pattern of soil moisture has the largest contribution, followed by the anomaly pattern of atmospheric loading. Our results are not consistent with the attribution of the observed 1997/1998 C_{20} anomaly to ocean bottom pressure anomalies as a typical ENSO response, but instead point to the importance of continental water storage, especially soil moisture.

2.1 Introduction

The global hydrological cycle regulates the water mass exchange between the atmosphere, oceans and continents on seasonal to decadal time scales. Water is stored and cycled between these reservoirs through precipitation, evapotranspiration and river runoff. In the atmosphere, water is mainly stored in the form of water vapor, the holding capacity being mainly regulated by the air temperature (e.g. Gill, 1982). On the continents, water can be stored in various reservoirs, e.g. in rivers and lakes, in the soil and biomatter, or as snow (Cazenave et al., 2000). Any net imbalances between the continents and atmosphere is compensated by ocean mass variations, resulting in eustatic (mass related) sea level changes. Since the climate-related movement and distribution of water on Earth's surface directly changes the gravity field, monitoring this field from space with satellites can yield information on otherwise difficult to obtain quantities such as ocean bottom pressure or land water storage (Tapley et al., 2004). As these observational data have been available since 2002 from the Gravity Recovery and Climate Experiment (GRACE) satellite mission, it is important to compare them against geophysical models. The interpretation of gravity field solutions from GRACE requires an understanding of the interactions between the atmosphere, oceans and continents. Also, models must be utilized to distinguish intrinsic climate variability from ongoing anthropogenic changes, because detailed observations of the Earth's surface water distribution in an anthropogenically unperturbed climate do not exist.

Following typical convention (e.g. Cazenave and Nerem, 2004), we distinguish between *steric* (density-related), and *eustatic* (mass-related) sea level changes in this paper. Seasonal global mean sea level is greatly influenced by mass exchanges between the ocean and the atmosphere and continental water storage reservoirs (Chen et al., 1998; Cazenave et al., 2000). On interannual time scales, the El Niño-Southern Oscillation (ENSO) is a dominant mode of climate variability (e.g., McPhaden et al., 2006). It involves large-scale reorganizations of the atmosphere and ocean circulation that originate in the equatorial Pacific, leading to temperature and precipitation anomalies extending across the entire globe (Trenberth and Caron, 2000; Trenberth et al., 2005). The associated changes of the hydrological cycle and surface water distribution in turn affect Earth's gravity field on a variety of spatial and temporal scales. Long wavelength geodetic signals have been inferred from satellite laser ranging (SLR) in the form of low-degree spherical harmonic components. A prominent signal was the positive J_2 anomaly of 1997/1998 observed by Cox and Chao (2002), consistent with a mass transport from high to low latitudes. This anomaly coincided with a strong ENSO event, and also with a shift of the Pacific decadal oscillation (PDO). This strong ENSO event was also marked by a significant global mean

sea level anomaly (Nerem et al., 1999).

Based on an ocean model that assimilates observations, and observed snow and ice data for subpolar glaciers, Dickey et al. (2002) argued that a substantial part of the 97/98 J_2 anomaly can be attributed to dynamic ocean mass redistribution, and to subpolar glacial melting, but the dynamic links between the mass shifts and the climate anomalies could not be determined. Cox and Chao (2002), on the other hand, argued against ice sheet changes (from polar ice sheets as well as subpolar glaciers) as a major source for the observed 97/98 J_2 anomaly, because the implied global mean sea level signal would have been larger than observed. Additionally, the partial return of the observed J_2 toward normal values in 2001 was put forward as an argument against a dominant role for glacial melting, because the implied glacial melting and growing rates were not observed (Chao et al., 2003). Since observed variations in low-degree gravity coefficients could also be excited within the solid Earth, e.g. from core mantle coupling, it is necessary to distinguish the contribution of the fluid surface layer to non-seasonal low-degree gravity coefficients.

Based on TOPEX/POSEIDON measurements and ocean model results, Nerem et al. (1999) concluded that the observed global mean sea level anomaly of 97/98 was mainly of thermosteric origin. They also found a positive global mean anomaly of precipitable water in the atmosphere, suggesting that the increased atmospheric water vapor reduced the outgoing long wave radiation, thus increasing ocean heat content, and raising sea level accordingly. On the other hand, Willis et al. (2004) reported in their objective analysis of oceanic hydrographic profiles that large amounts of heat were redistributed within the ocean during the 1997/1998 El Niño, but they did not find a net global heat gain or loss, leading to the conclusion that the observed global mean sea level anomaly was mainly of eustatic origin. Regardless of its nature, ENSO related sea level changes can significantly affect sea level rise estimates, in turn requiring long measurements for a robust determination of the anthropogenic warming signal (Nerem et al., 1999).

Thus, there appear to be two major issues that remain unclear in terms of sea level changes and large-scale hydrological mass redistribution in relation to ENSO: first, can ENSO generally be associated with a global mean sea level anomaly, and if so, does the sea level anomaly have a eustatic contribution, and how is it balanced? Second, can ENSO related mass redistribution generally be associated with a significant low degree geopotential signal, and if so, what are the geographical patterns and contributions of the individual storage reservoirs that lead to this anomaly?

Assessing the water cycling between reservoirs from observations is usually accomplished by combining independent data sets for the ocean, atmosphere and continents, and the uncertainty in each can be quite large (Cazenave et al., 2000). In what follows, we explore the seasonal and non-seasonal water cycling in the Earth system with a state-of-the-art

climate model, focusing on ENSO related signals. Because the model is unconstrained by observations, we cannot compare the results directly to observations since there is no phase agreement with particular observed events. Instead, our approach aims to understand typical magnitudes and mechanisms of ENSO related hydrological signals. Coupled global atmosphere-ocean general circulation models have been extended to include land-surface and river routing schemes, which allow for the storage of water in the soil and as snow. The main challenge in understanding (and simulating) the water cycling between the different reservoirs is to close the total water budget dynamically, implying consistent fresh water fluxes between all reservoirs. Although many of the governing processes of the hydrological cycle on land are still poorly understood (and thus highly parameterized in their numerical representation), state-of-the-art models offer the advantage of consistent water fluxes between the hydrological reservoirs, avoiding the need for artificial flux or mass adjustments. Additionally, climate models have a global coverage, which in light of large-scale ENSO teleconnections is essential to capture the total Earth system response (Hughes and Stepanov, 2004; Trenberth et al., 1998).

The paper is structured as follows: In Sec. 2.2, we describe the pertinent model features and behavior, as well as some theoretical aspects. In Sec. 2.3, we compute the seasonal cycle of sea level and the water budget. We then use linear regression analysis to determine the ENSO relation of non-seasonal steric and eustatic sea level, the global mean of each individual water reservoir, and the geographical pattern of all water storage and sea level terms. We then compute the response of the degree-two geoid components to the geographical pattern of the mass load anomalies. A discussion of our main results then follows in Sec. 2.4. We conclude this paper with a summary of our main findings in Sec. 2.5.

2.2 Model Description and Theory

2.2.1 The ECHAM5/MPI-OM Model

In this study, we use monthly data from 200 years of a climate simulation computed with the coupled ECHAM5/MPI-OM atmosphere-ocean general circulation model that also served as the unperturbed reference climate for the IPCC 4th assessment report projections (Meehl et al., 2007). No anthropogenic or volcanic forcing is included; the concentrations of well-mixed greenhouse gases are set to the standard year 1860 values. The ocean component MPI-OM uses an orthogonal curvilinear grid with its North Pole shifted to Greenland to avoid a singularity at the geographical North Pole. The vertical resolution is 40 levels, 20 of which are distributed over the upper 700 m; partial grid cells

resolve the bottom topography. Horizontally, the resolution gradually varies between 12 km near Greenland and 180 km in the tropical Pacific. MPI-OM (Marsland et al., 2003) is coupled to the ECHAM5 atmosphere model (Roeckner et al., 2003) at T63 horizontal resolution ($1.875^\circ \times 1.875^\circ$) with 31 vertical levels; the top atmospheric level is at 10 hPa, so that stratospheric processes are not taken into account. The coupling of the atmosphere to the ocean requires no flux adjustments. A dynamic/thermodynamic sea ice model with viscous-plastic rheology is embedded in MPI-OM. More details on the ocean model formulation can be found in Marsland et al. (2003) and Jungclaus et al. (2006). Note that the ocean component has not yet reached its equilibrium state in this simulation, as the ocean heat content exhibits a drift of about 2.6×10^{21}J/year, corresponding to a drift in thermosteric sea level of about 0.4 mm/year. This is largely related to insufficient Antarctic Bottom Water formation, resulting in a slow warming of intermediate and deep waters (Jungclaus et al., 2006; Landerer et al., 2007c). The trend weakens over time, as the model appears to slowly approach an equilibrium state. Therefore, we apply a quadratic drift correction to the heat content and steric sea level terms, rather than a simple linear fit (root mean squared error (RMSE) for linear fit: 2.60×10^{22} J; RMSE for quadratic fit: 2.27×10^{22} J).

On the continents, surface runoff and drainage are calculated by a runoff scheme (Dümenil and Todini, 1992), and fed into a hydrological discharge (HD) model (Hagemann and Dümenil, 1998), with the limitation that growing and melting of land ice is not considered, effectively excluding cryospheric variability in the simulations. Over the ice sheets, mass balance is achieved by routing precipitation (minus evaporation) that falls on the ice sheet to the nearest ocean grid point as runoff. Continental water can be stored as snow or in the soil; the maximum soil moisture bucket depth extends to about 2 m, and varies according to land surface parameters (Hagemann, 2002); groundwater storage is not accounted for.

As stated in the introduction, an important motivation for the use of a fully coupled climate model is the consistency of fresh water fluxes between all reservoirs and the implied conservation of mass. The conservation of mass in terms of water storage requires that

$$\frac{\Delta(M_{oce} + M_{atmo} + M_{conti})}{\Delta t} = 0, \tag{2.1}$$

where M_{oce}, M_{atmo} and M_{conti} are the fresh water storage terms for the ocean, atmosphere and continents, respectively. Here, we compute M_{oce} by integrating the global net freshwater flux over the oceans, and atmospheric storage M_{atmo} is the total atmospheric water content. The change in continental water storage is given by the budget

$$\Delta M_{conti} = (P - E - R)\Delta t, \tag{2.2}$$

where P is precipitation, E is evaporation and R is runoff over land. In ECHAM5, water on the continents is stored in the form of soil moisture and snow. However, some surface water directly enters into the lateral flow scheme of the HD model. Also, the HD model temporarily stores runoff and drainage fluxes in buffer reservoirs that account for the residenc times of water in the different flow processes within a HD model gridbox (over-land flow, basal flow), and betwen gridboxes (S. Hagemann, 2007, personal communication). The latter may also be interpreted as the water stored in the river network. As the buffer reservoir terms are not saved to disk in the standard ECHAM5 configuration, we need to correct for them to close the mass budget (Eq. 2.1). Note that the mass balance is maintained during the simulation, but we must reconstruct the 'residual runoff' water from the balance between eustatic sea level, atmopsheric water storage, and water storage in the soil and snow on the continents; the amplitude and relevance of this 'residual runoff' term is discussed in sections 2.2 and 2.3.2.

In this paper, we will distinguish between total ocean mass variations and local ocean mass variations, which are associated with dynamic ocean mass redistribution, but leave the global ocean mass unchanged. As will become clear shortly, ocean mass load is synonymous to ocean bottom pressure, the two being related linearly. Some implicit model assumptions warrant a more detailed description of the calculation of ocean bottom pressure; in our derivation, we follow Ponte (1999).

The integration of the hydrostatic equation over the whole water column gives

$$p_b = g \int_{-H}^{\eta} \rho dz + p_a \approx g\rho_0\eta + g \int_{-H}^{0} \rho dz + p_a, \tag{2.3}$$

where g is the mean surface gravitational acceleration, p_a is the surface atmospheric pressure, ρ is the density, and η the sea surface height above a reference level. Under the inverted barometer (IB) assumption, which holds on time scales longer than a few days (Wunsch and Stammer, 1997; Ponte et al., 1991), it can be shown without loss of generality that $\eta = \eta_{IB} + \eta_{dyn}$, i. e. the IB term plus an ocean dynamic signal η_{dyn} related to pressure, wind, or any other forcing. The IB term is defined as

$$\eta_{IB} = \frac{1}{g\rho_0}(\overline{p_a} - p_a), \tag{2.4}$$

where p_a is the area averaged pressure over the global oceans. Equation 2.3 then reduces

to

$$p_b = g\rho_0\eta_{dyn} + g\int_{-H}^{0}\rho dz + \overline{p_a}. \tag{2.5}$$

In MPI-OM, the model dynamics do not include forcing from p_a, and the sea surface height η_{dyn} is given by the vertically integrated continuity equation in the Boussinesq approximation:

$$\frac{\partial\eta}{\partial t} + \frac{\partial U}{\partial x} + \frac{\partial V}{\partial y} = Q_\eta(\phi,\lambda) = P - E + R. \tag{2.6}$$

Here, U and V are the vertically integrated zonal and meridional flows, respectively; ϕ is latitude, λ is longitude. The forcing term $Q_\eta(\phi,\lambda)$ represents surface freshwater flux due to precipitation (P), evaporation (E) and river run-off (R). At time steps of one month, the prognostic SSH field is recentered to a zero global mean. Therefore, the continuity equation (2.6) implies volume conservation (Gill, 1982) in the ocean; while this formulation yields correct relative horizontal SSH gradients, Greatbatch (1994) showed that two spatially uniform, but time-varying correction terms must be applied to the calculated sea level to make up for missing physics in the model: one is the 'steric correction', accounting for any net expansion or contraction of the global ocean due to changes in the density structure; the second correction is 'eustatic' and accounts for global net freshwater fluxes by adding a uniform layer of water over the oceans determined from the global integral of $Q_\eta(\phi,\lambda)$ over time. Since both corrections are spatially uniform, they have no influence on the models dynamics. Note also that tidal forcing is not included in present MPI-OM setup.

Dividing Eq. 2.5 with $g\rho_0$ gives the normalization of bottom pressure in units of meters of equivalent water column height, which we use throughout the rest of this paper (the use of a constant density ρ_0 is consistent with the Boussinesq approximation made in the ocean model). Introducing the eustatic correction term into Eq. 2.5 then leads to

$$\frac{p'_b}{g\rho_0} = \eta'_{dyn} - \eta'_s + \overline{\eta'_a} + \overline{\eta'_Q}, \tag{2.7}$$

where the prime indicates the anomaly relative to a time mean or an unperturbed state; all quantities on the right hand side are in units of equivalent sea level height. The term $\eta'_s = \rho^{-1}\int\rho' dz$ is the steric height anomaly, $\overline{\eta'_a}$ is the bottom pressure contribution due to changes of the mean atmospheric mass over the oceans (subsequently referred to as atmospheric ocean loading), and $\overline{\eta'_Q}$ represents the bottom pressure contribution due to total ocean mass changes (or eustatic sea level changes). Thus, in a stratified ocean, sea

level and bottom pressure can be very different (Condi and Wunsch, 2004). Generally, steric effects become more important at longer periods and towards the equator, indicating that oceanic variability in these regions is more baroclinic, whereas the shallow ocean is characterized by barotropic variability (Vinogradova et al., 2007). Consequently, the term $\eta'_{dyn} - \eta'_s$ represents bottom pressure variations due to dynamic ocean mass redistribution at constant global ocean mass, which we will refer to as the bottom pressure or dynamic bottom pressure in this paper. The seasonal dynamic bottom pressure variability in MPI-OM is similar to that found by Condi and Wunsch (2004): high variability is found in Northwest Pacific, Southern Pacific, and high latitude Atlantic Oceans (not shown). Through Eq. 2.7, we can thus differentiate between contributions to ocean bottom pressure from changes of dynamic bottom pressure, eustatic sea level and mean atmospheric mass loading over the oceans.

2.2.2 Simulated El Niño-Southern Oscillation

The tropical Pacific climate variability is well represented in space and time in the coupled climate model ECHAM5/MPI-OM (Guilyardi, 2006; Jungclaus et al., 2006). The structure of interannual SST anomalies is well simulated, but the magnitude of the variability is generally overestimated by a factor up to 1.4 (Jungclaus et al., 2006); the dominant frequency of the simulated tropical Pacific Ocean variability is between 3.5 and 4 years, which is sufficiently close to observations. This warrants the analysis of water storage anomalies in the atmosphere, ocean and on land related to ENSO by means of simple linear regression. The precipitation response in ECHAM5 to ENSO events realistically captures most aspects of the local and remote precipitation distribution, although the simulated amplitude is somewhat too large (Hagemann et al., 2006). Also, the model does not fully reproduce the observed precipitation response to ENSO variability over the Indian Ocean and Africa (Hagemann et al., 2006).

For the following regression analysis, we use the Nino3 index. It is defined as monthly sea surface temperature anomalies, averaged over the region extending from 5°S-5°N and 150°W-90°W (Trenberth, 1997). We identify an El Niño (positive values) or La Niña (negative values) event if the 5-month running-average of the index exceeds one standard deviation for at least 6 consecutive months (Fig. 2.1); the 5-month running-average is used to smooth out variations in sea surface temperature not associated with ENSO. El Niño episodes are usually accompanied by sustained warming of the central and eastern tropical Pacific Ocean and a decrease in the strength of the Pacific trade winds. During El Niño, rainfall diminishes over the western equatorial Pacific Ocean, and increases over the eastern half of the tropical Pacific Ocean, consistent with a weaker Walker circulation.

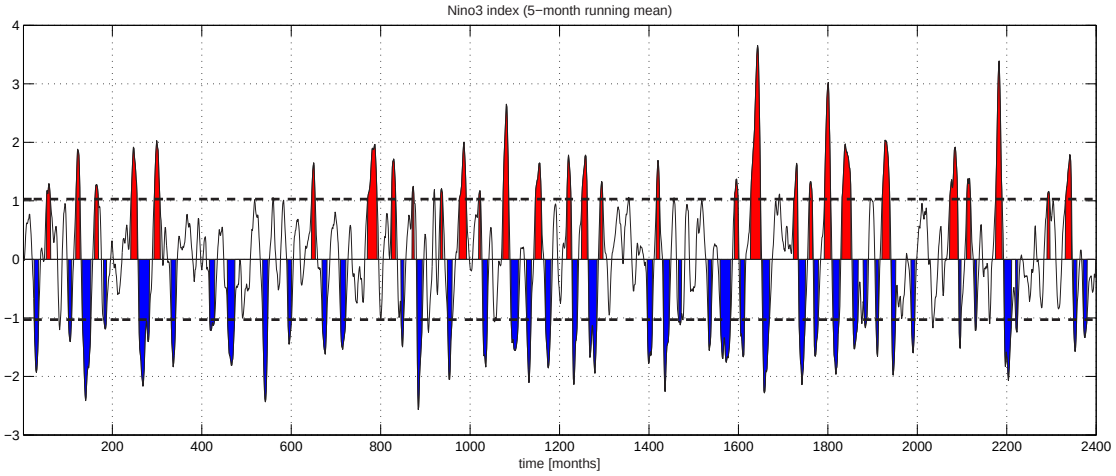

Figure 2.1: *Five-month running mean of the simulated Nino3 index. The dashed line is the 1-σ standard deviation; El Niño (red) and La Niña events (blue) are defined as periods where the index exceeds 1 σ for at least 6 consecutive months.*

La Niña episodes are associated with stronger Pacific trade winds and warmer sea surface temperatures in the western tropical Pacific Ocean, while waters in the central and eastern tropical Pacific Ocean become cooler during this period. An El Niño event is often followed by a La Niña event. Note, however, that El Niño and La Niña events do not necessarily scale linearly, and individual ENSO events may deviate from each other in their overall climate impact.

The atmospheric surface pressure-based Southern Oscillation Index (SOI) is used in some of the cited references to describe ENSO related climate variability; in the present ECHAM5/MPI-OM simulation, the correlation between SOI and Nino3 is -0.73 (5-month running mean applied to each index); therefore, the following regressions on the Nino3 index are approximately equal to regressions on the SOI index, but with reversed sign.

2.2.3 Geopotential and Stokes Coefficients

Earth's geopotential field U can be expanded into spherical harmonics given by (Heiskanen and Moritz, 1967)

$$U(\phi,\lambda,r) = \frac{GM}{r}\left[1+\sum_{l=2}^{\infty}\sum_{m=0}^{l}\left(\frac{R}{r}\right)^{l}\overline{P}_{lm}(\sin\phi)(C_{lm}\cos m\lambda + S_{lm}\sin m\lambda)\right], \quad (2.8)$$

where r is the distance from Earth's center, ϕ is latitude, λ longitude, G the gravitational constant, M Earth's mass and R Earth's mean radius; $\overline{P}_{lm}(\sin\phi)$ are the fully normalized associated Legendre polynomials of degree l and order m (Eubanks, 1993), and C_{lm} and

S_{lm} are the so-called Stokes coefficients. The coefficients C_{lm} and S_{lm} are related to the Earth's density distribution $\rho(\phi, \lambda, r)$ via

$$\left\{ \begin{matrix} C_{lm} \\ S_{lm} \end{matrix} \right\} = \frac{1}{(2l+1)M} \int_V \rho(\phi, \lambda, r) \left(\frac{r}{R}\right)^l \overline{P}_{lm}(\sin\phi) \left\{ \begin{matrix} \cos(m\lambda) \\ \sin(m\lambda) \end{matrix} \right\} dV. \tag{2.9}$$

For surface mass load variations $\Delta q(\phi, \lambda)$, the thin shell approximation reduces Eq. 2.9 to the fully normalized degree-two Stokes coefficients as the surface integral of mass load changes $\Delta q(\lambda, \phi) = p_b' g^{-1}$ at each grid point, given by (Chen et al., 2003)

$$\left\{ \begin{matrix} \Delta C_{lm} \\ \Delta S_{lm} \end{matrix} \right\} = \frac{(1+k_l)}{(2l+1)M} \int_S \Delta q(\lambda, \phi) \overline{P}_{lm}(\sin\phi) \left\{ \begin{matrix} \cos(m\lambda) \\ \sin(m\lambda) \end{matrix} \right\} dS, \tag{2.10}$$

where $dS = R^2 \cos\phi d\theta d\lambda$, k_l is the Love number. For the degree-two coefficients (l=2), we take as $k_2 = -0.301$ (Chen et al., 2005). The Love number takes into account the yielding of the solid Earth to the surface mass load changes, assuming an elastic load response (Wahr et al., 1998). This assumption should be realistic on ENSO time-scales. The fully normalized associated Legendre polynomials of degree 2 and order $m = (0, 1)$ are given by (Heiskanen and Moritz, 1967)

$$\begin{aligned} \overline{P}_{20}(\sin\phi) &= 0.5(3\sin(\phi)^2 - 1) \\ \overline{P}_{21}(\sin\phi) &= 3\sin(\phi)\cos(\phi). \end{aligned} \tag{2.11}$$

Measurements of time varying gravity such as the GRACE mission then allow for the inversion of Eq. 2.10 to determine the surface mass load distribution $\Delta q(\phi, \lambda, t)$ via (Wahr et al., 1998)

$$\Delta q(\phi, \lambda, t) \approx \frac{R\rho_E}{3} \sum_{l=2}^{l_{max}} \sum_{m=0}^{l} \frac{(2l+1)}{(1+k_l)} \overline{P}_{lm}(\sin\phi)(C_{lm}(t)\cos m\lambda + S_{lm}(t)\sin m\lambda), \tag{2.12}$$

where ρ_e is the average density of the Earth (5517 kg m^{-3}); for GRACE, l$_{max}$ is typically 120, equivalent to a horizontal wavelength of about 300 km.

In the case of a spatially uniform eustatic sea level change Δh, as well a uniform inverted barometer response of equivalent sea level change Δh, Eq. 2.10 can be simplified to

$$\left\{ \begin{matrix} \Delta C_{lm} \\ \Delta S_{lm} \end{matrix} \right\} = \Delta h \rho_0 \frac{(1+k_n)}{(2l+1)M} \int_S F(\lambda, \phi) \overline{P}_{lm}(\sin\phi) \left\{ \begin{matrix} \cos(m\lambda) \\ \sin(m\lambda) \end{matrix} \right\} dS, \tag{2.13}$$

where Δh is in meters, ρ_0 is the mean density of sea water, and $F(\lambda, \phi)$ is the ocean function with values of 1 over the ocean, and 0 over land. Based on the ECHAM5/MPI-

OM grid, the numerical constants for a uniform sea level change are then

$$\left.\begin{array}{l}\Delta C_{21}\\ \Delta S_{21}\\ \Delta C_{20}\end{array}\right\} = \Delta h \rho_0 \times 1.0^{-10} \times \left\{\begin{array}{l}4.76\\ 7.62\\ 7.22\end{array}\right. \tag{2.14}$$

Thus, compared to S_{21}, C_{21} is about 40% less sensitive to a global mean eustatic sea level change, or similarly, to a global mean inverted barometer anomaly.

The degree-two Stokes coefficients are directly proportional to surface mass load induced Earth rotational excitations, given by the so-called effective angular momentum functions (Barnes et al., 1983; Chen, 2005). Note that $C_{l0} = -J_l/\sqrt{(2l+1)}$, as J_l is used instead of C_{l0} in some of the cited references. From the integration kernel in Eq. 2.10 it is readily inferred that a decrease in C_{20} means a net transport from high to low latitudes; nodal lines of C_{20} are at $\pm 35.3°$. Stokes coefficients do not allow a unique inversion to trace back the origin of their anomalies, but they place an integral constraint on possible mass load distributions. Especially on seasonal to interannual time scales, it is expected that the main signal comes from the surface water distribution from the hydrological cycle (Tapley et al., 2004). Note that mass conservation in the Earth system between the atmosphere, ocean and continental water storage terms is necessary for the correct determination of low-degree Stokes coefficients (Chen, 2005; Gross et al., 2004). Quantitatively, mass balance is particularly important for the degree-one and degree-zero coefficients, but may still affect the global budget for the degree-two coefficients considerably (Chen, 2005).

2.2.4 Linear Regression

We use a linear least squares approach to project the monthly water storage and degree-two coefficient anomalies on the Nino3 index (normalized by its standard deviation) for lags up to ± 60 months with one-month increments; positive lags mean that the Nino3 index leads the sea level, water storage or bottom pressure anomaly. The significance (set here to 95%) of the regression is computed from the regression model's F-statistic by testing against the null hypothesis that there is no regression relationship between the variables (von Storch and Zwiers, 1999).

This estimate depends on the degrees of freedom in the time series, which for truly independent samples is equivalent to $N - 2$, where N is the total sample size. However, not all samples in the present analysis are truly independent. Intrinsic low-frequency variability or low-pass filtering (e.g. applying a running mean, as used here) introduces serial correlation into the time series, which would make any statistical test less stringent (Trenberth, 1984). The degrees of freedom is reduced to the effective number of independent

observations N_{eff}, defined as (Trenberth, 1984)

$$N_{\text{eff}} = N\frac{\Delta t}{T_0}. \tag{2.15}$$

Here, Δt is the sampling interval, and T_0 denotes the time between effectively independent observations. There are various possibilities (and difficulties) in estimating T_0 (von Storch and Zwiers, 1999). For large numbers of observations N, and under the assumption of a process with a red spectrum, we can approximate T_0 by

$$T_0 = \frac{1+\alpha}{1-\alpha}, \tag{2.16}$$

where α is the product of the lag-1 autocorrelation values of two processes X_t and Y_t (Trenberth, 1984). Intuitively, T_0 can be thought of as an integral time scale representing physical memory in the observations (von Storch and Zwiers, 1999).

2.3 Results

2.3.1 Seasonal Cycles of Water Budgets and Sea Level

For the assessment of ENSO related variability in Earth's water mass budget, we need to subtract the seasonal cycle from all relevant water storage reservoirs and sea level terms. In this section, we compare Earth's average seasonal water reservoir budget as simulated by ECHAM5/MPI-OM with published observational or other simulated estimates. A correct representation of the seasonal cycle is necessary in order to have faith in the amplitudes of deviations from the monthly values.

We compute a monthly climatology of ocean mass variation, continental hydrology (split into snow depth and soil moisture), atmospheric water storage and steric sea level, as well as the standard deviation for each month from a total of 2400 simulated months (200 years)(Fig. 2.2 and Tab. 2.1); all values listed in Table 2.3.1 are in units of equivalent sea level height, so their magnitudes can be directly compared. Note that we need to subtract a drift of -0.142 mm/yr of the integrated fresh-water flux over the ocean, which would otherwise lead to an unphysical mass loss in the ocean; all other reservoir fields do not require drift corrections. For the atmospheric water storage, we only use the vertically integrated water vapor. We do not include vertically integrated cloud water and cloud ice in the present analysis, because their contribution to the water mass budget is a factor of about 1000 less important than vertically integrated water vapor in ECHAM5 (not shown).

As a reference for the seasonal cycle of water budgets, we use values published by

Source	ECHAM5/MPI-OM	Observations
Total sea level	7.0±3.5 mm (Oct)	4.3±0.4 mm (Oct)
Non-Steric	9.1±2.8 mm (Sep)	9.0 mm (Sep)
Steric	3.6±2.4 mm (Apr)	5.0 mm (Mar)
Atm. water vapor	2.2±0.6 mm (Dec)	2 mm (Dec)
Snow	4.1±0.01 mm (Aug)	7 mm (Aug)
Soil moisture	5.7±2.1 mm (Aug)	2.6 mm (Sep)
Sum continental	10.0±2.1 mm (Oct)	9.0 mm (Sep)
Heat content	2.93×10^{22}J (Apr)	4.5×10^{22}J (Apr)

Table 2.1: *Maximum amplitude and standard deviation for the given month of the individual reservoir storage and contribution to sea level, determined from the climatological seasonal cycle in ECHAM5/MPI-OM; all values in units of equiv. sea level height. Reference values are from Cazenave et al. (2000), except for heat content, which is from Gleckler et al. (2006).*

Cazenave et al. (2000) (more references and recent values can be found in Chambers et al. (2004) and Lombard et al. (2006)). While the mass budget of the ocean can be inferred from observations (sea level from altimetry minus steric contribution), water storage over land is not directly measured due to sampling problems in both space and time (Cazenave et al., 2000). Rather, land surface models are typically driven with observed meteorological data (e.g. precipitation and temperature), and water storage in the soil and as snow is estimated from the models. Gravity based measurements of continental water storage are now solving this limitation and measure land water storage changes from an inversion of gravity field anomalies more directly (Tapley et al., 2004). The total continental water mass signal in ECHAM5/MPI-OM, comprised of snow and soil moisture, compares well with those of Cazenave et al. (2000). However, the partitioning between soil moisture and snow is quite different (about 3 mm difference). As the coupled model ECHAM5/MPI-OM used in the present study simulates slightly more total snow mass than the stand-alone ECHAM5 atmosphere model (E. Roeckner, pers. communication), which was found to accurately portray amplitude and phase of the seasonal cycle in snow depth (Roesch and Roeckner, 2006), we can only speculate what causes this difference. Soil moisture and snow mass are probably the least well observed (or often crudely approximated) water storage quantities, so error bars should be quite large. However, the agreement of the total continental storage between Cazenave et al. (2000) and ECHAM5/MPI-OM is a good indicator that we simulate a reasonable seasonal cycle of the water budgets. Since the ice sheets are not dynamically coupled in our simulation, their mass is time-invariant, and we cannot include their contribution to sea level variations in the mass balance analysis. Cazenave et al. (2000) estimate a seasonal sea level contribution of Antarctica of about 3 mm (maximum in December), and a Greenland seasonal sea level contribution of about

0.6 mm (maximum in July); however, the error bars on both estimates are still rather large. The estimated atmospheric water storage agrees well with observations, but has the smallest contribution to the seasonal water storage cycle.

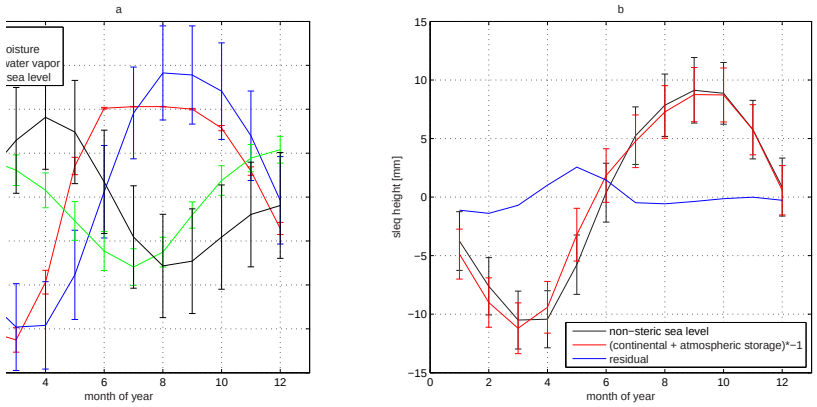

Figure 2.2: *a): seasonal sea level contribution from atmospheric water vapor (green), soil moisture (blue), snow (red), and steric sea level (black). b): sum of seasonal atmospheric and continental terms (red), eustatic sea level (black), and difference between them (residual, blue). In a) and b), bars indicate the monthly standard deviation. Units: mm of equiv. sea level.*

As explained in Sec. 2.2.1, not all continental water storage terms necessary to close the water storage budget are available as model output. We have to estimate the missing term a posteriori from the difference of oceanic storage minus continental (soil moisture and snow) and atmospheric storage (Fig. 2.2b). This 'runoff residual' has a maximum sea level contribution of about 2.5 mm in May, indicating that during this time, more precipitation enters runoff directly without being stored in the soil or as snow. Note that total runoff and the 'runoff residual' are correlated with 0.72 (not shown).

The seasonal signal of steric sea level is representative of the seasonal cycle of ocean heat content, which is basically confined to the upper thermocline. Based on WOA04 observations, Gleckler et al. (2006) report a maximum of 4.5×10^{22}J in April, and a minimum of -3.9×10^{22}J in September. ECHAM5/MPI-OM simulates too small a seasonal cycle of ocean heat uptake and release, which thus also causes the seasonal steric sea level to be underestimated, as described above. This behavior of ECHAM5/MPI-OM appears to be a typical shortcoming of numerical models, which tend to have too little seasonal to decadal ocean variability in terms of ocean heat storage (Gregory et al., 2004).

The total seasonal sea level signal in our simulation as the sum of steric and eustatic contributions is +7.0 mm in October, and -7.9 mm in April. This is larger than what is observed. Since the steric and eustatic sea level are about 180° out of phase, errors in the estimated steric (underestimated, +1 month lag) and eustatic (slightly too large)

Reservoir / Sea level term	σ [mm]	Min [mm]	Max [mm]	T_0 in months	N_{eff}
Non-Steric sea level	2.4	-8.6	5.9	62	39
Atm. water vapor	0.7	-1.7	2.3	56	43
Soil moisture	2.0	-4.6	8.1	63	37
Snow	0.2	-1.2	0.8	23	103
Runoff residual	0.9	-2.6	3.3	45	53
Wet atm. loading	0.5	-1.7	1.4	57	42
Dry atm. loading	1.2	-3.7	3.9	16	148
Steric sea level (hp-filtered)	1.8	-5.6	4.1	78	31
Total sea level (hp-filtered)	3.0	-13.3	6.6	60	40

Table 2.2: *Standard deviation, minimum/maximum non-seasonal values in units of mm of equivalent sea level, memory time scale T_0, and effective number of independent observations N_{eff} computed from Eq. 2.15 of monthly anomalies for individual water storage reservoirs, wet and dry atmospheric ocean loading, and steric sea level. A five-month running mean has been applied to all data.*

seasonal signal add up. However, it has to be kept in mind that averaging periods used to derive the seasonal signal from observations are shorter than in our simulations; further, observations are not fully global, and the observed values are sensitive to the extrapolation and mapping methods applied (Gregory et al., 2004; Lombard et al., 2006).

2.3.2 Regression of Non-Seasonal Water Storage, Sea Level and Atmospheric Loading on ENSO

In this section, we subtract the seasonal cycle and explore whether non-seasonal sea level and integrated water storage anomalies in any one of the reservoirs - atmosphere, ocean or continents - are correlated with ENSO. As pointed out in the introduction, it appears not to be clear from observations whether eustatic sea level varies with ENSO and if so, how such a eustatic ocean signal would be balanced. In order to facilitate comparison between the reservoirs, the water storage anomalies are integrated over each area, and scaled into equivalent meters of sea level height by dividing with the global sea surface area. The climatological monthly mean for each reservoir has been subtracted (Fig. 2.2; Sec. 2.2).

In terms of overall monthly anomalies, eustatic sea level and soil moisture have the largest amplitude range, and also the largest temporal variability (Tab. 2.2; Fig. 2.3 a and c). These two terms are correlated with $c = -0.88$, indicating that the largest fraction of non-seasonal water storage anomalies is balanced between these two reservoirs. Snow and atmospheric water vapor anomalies contribute considerably less to eustatic sea level (Fig. 2.3 b and d). In order to better understand their temporal behavior, we also compute the power spectral density of the monthly water storage anomalies for each reservoir using Thompson's multitaper method (Thompson, 1982). Most energy of monthly eustatic sea

level anomalies resides in 10-30 year band, with relatively little energy at ENSO relevant periods around 3-8 years (Fig. 2.3 a). Monthly soil moisture anomalies are characterized by somewhat higher frequencies in the band of 3-15 years (Fig. 2.3 c), and monthly anomalies of snow storage feature even more high frequency variability in the range of 2 to 10 years (Fig. 2.3 d). Atmospheric water vapor storage has a prominent spectral peak in the ENSO-relevant frequency band of 3-8 years, but considerable energy also resides at longer periods around 20 years (Fig. 2.3 b). Similar to the calculation of the seasonal cycle, we need to account for the 'runoff residual' to close the mass budget of the monthly anomalies (see Sec. 2.3.1). The monthly anomalies of this term are generally small, with larger amplitudes occurring concurrently with strong changes in soil moisture and snow storage (Fig. 2.3 e). Correcting the sum of soil moisture and snow storage with the 'runoff residual' does not alter the amplitude and phasing of the total continental storage significantly: the corrected continental storage term (soil moisture + snow storage - 'runoff residual') is correlated with the uncorrected continental storage term (soil moisture + snow storage) with c=0.92 (not shown). Note also that most variability in the 'runoff residual' is for frequencies of 10 years and longer (Fig. 2.3 e), indicating that its influence in terms of ENSO related continental storage variability is relatively minor.

For all storage terms in Fig. 2.3, we perform the linear regression on the Nino3 index (normalized by its standard deviation) for lags up to ± 60 months; the effective number of independent observations was calculated from Eq. 2.15 and is given in Tab. 2.2, together with the corresponding memory time scale as detailed in Sec. 2.2.4. From the total of 2400 monthly anomalies, only between 31 to 148 are actually independent. These estimates are rather conservative, making the significance test quite stringent, but it prevents incorrect rejections of the null hypothesis that there is no regression relation between the storage terms and ENSO. Non-steric sea level has no significant regression on Nino3 (Fig. 2.4 a), and the explained variance of the signal is below 6% at all lags (Fig. 2.4 b). As already indicated by its spectrum, the atmospheric water storage is significantly related to Nino3: lagging Nino3 by three months, the regression yields 0.6 mm/σ(Nino3), with an explained variance of almost 80%. At a lead of -15 months, atmospheric water storage is also significantly correlated with Nino3, but the explained variance drops to 15% (Fig. 2.4 c and d). Of the continental storage terms, soil moisture has a significant regression on Nino3 with about -0.85 mm/σ(Nino3) lagging Nino3 by five months, but snow storage does not have a significant regression at any lag (Fig. 2.4 e-h). Correcting the continental storage with the 'runoff residual' (Fig. 2.3 e) does not change these numbers significantly (Fig. 2.4 i-j): soil moisture is the only effective continental storage reservoir in terms of ENSO variability such that there is less water stored on land (positive sea level contribution) lagging El Niño by five months. Note, however, that while the regression coefficient for

continental water storage increases slightly to almost -1 mm/σ(Nino3) when the 'runoff' correction is applied, the explained variance of the monthly continental water storage anomalies drops from an already low 18% to about 15%. Thus, although eustatic sea level and soil moisture are the major storage reservoirs for the monthly anomalies, we conclude from Fig. 2.4 that non-seasonal water distribution between the two is not strongly coupled with ENSO. The results of the regression analysis can be nicely illustrated in a single plot (Fig. 2.5): since hydrologic water exchange is mainly balanced between soil moisture and eustatic sea level, storage anomalies in the two reservoirs project on each other with a slope of nearly minus one. However, El Niño and La Niña events (marked by the red and blue colors, respectively, in Fig. 2.5) do not separate along the regression line, but instead above and below, demonstrating that the atmospheric water storage as the remaining reservoir is tightly coupled to ENSO.

So far, we have considered the eustatic sea level signal and its balance. The total sea level response is likewise influenced by steric sea level anomalies, while ocean bottom pressure is influenced by global mean atmospheric loading anomalies over the oceans (see Sec. 2.2.1). Splitting the atmospheric ocean loading signal into its wet and dry parts, we find that the amplitudes of monthly anomalies of the dry signal can be about a factor 2 larger than the wet signal, and the dry signal contains considerably more high frequency variability compared to the wet signal (Tab. 2.2 and Fig. 2.7 a,d). Since the wet atmospheric ocean loading is simply the atmospheric water vapor integrated over the oceans, it is not surprising that the regression of this signal on Nino3 looks very similar to that of the total atmospheric water vapor content on Nino3 (Fig. 2.6 b). The explained variance increases to over 80%, so we can conclude that most of the atmospheric water vapor storage anomalies related to ENSO variability is located over the oceans, increasing ocean bottom pressure in a globally uniform way under the inverted barometer assumption. We will revisit this point in the discussion of the degree-two geopotential signals in Sec. 2.3.4. Thus, in terms of the total atmospheric ocean loading response (wet plus dry signal), the dry atmospheric ocean loading dominates and destroys much of the clear wet atmospheric ocean loading signal (Fig. 2.7b). There is still a significant regression of the full atmospheric loading on Nino3 at lags of $\pm$ 10 months, but the explained variance is only 10% (Fig. 2.7c).

Steric sea level changes have no global mean bottom pressure signal, but are a good proxy for ocean heat content, as the two are related through the equation of state. An altimeter measures the combined eustatic and steric contributions, so the relative size of each anomaly is important for the interpretation of the total signal. We have computed the steric anomalies here from the fully time-dependent density changes, as opposed to a climatological background salinity distribution (as is often done in observations due to sparse salinity measurements). At constant ocean mass, global mean salinity is also con-

stant, but since the equation of state is non-linear, the steric sea level could be influenced by redistribution of salt within the ocean. However, such effects are very small, so the global mean steric signal is almost entirely of thermosteric nature. In the present simulation, the correlation between monthly anomalies of ocean heat content and steric sea level is 0.95, the remaining 10% of unexplained variance between the two quantities thus being due to non-linear effects in the density of sea water.

The simulated non-seasonal steric sea level and heat content have considerable variability at periods of 20-25 years and longer (not shown), which is not related to ENSO. We remove this longer-period variability with a high-pass filter (cut-off frequency 25 yr^{-1}). The regression of the filtered global mean ocean heat content on Nino3 then shows a significant signal of about 2.9×10^{21} J/σ(Nino3) leading Nino3 by four months (Fig. 2.8 a, d); steric sea level has a maximum of about 0.7 mm/σ(Nino3) leading Nino3 by one month, with an explained variance of nearly 40% (Fig. 2.8 b, e; for the unfiltered anomalies, the value drops below 8%). The oscillatory behavior of the Nino3 SST anomalies is reflected in a damped, mirrored regression signal about 20 months after the main ENSO signal. The fact that the heat content regression leads the steric sea level regression by about 4 months could be due to the non-linearity on the equation of state. However, the relative lag difference is within individual regression error bars, making this inference somewhat uncertain. The regression of the combined sea level signal (sum of non-seasonal eustatic and steric contribution) on Nino3 yields a significant maximum response of about 1 mm/σ at 0 lag. However, the variance explained with ENSO of the combined sea level anomalies drops to 16% (Fig. 2.8 c, f).

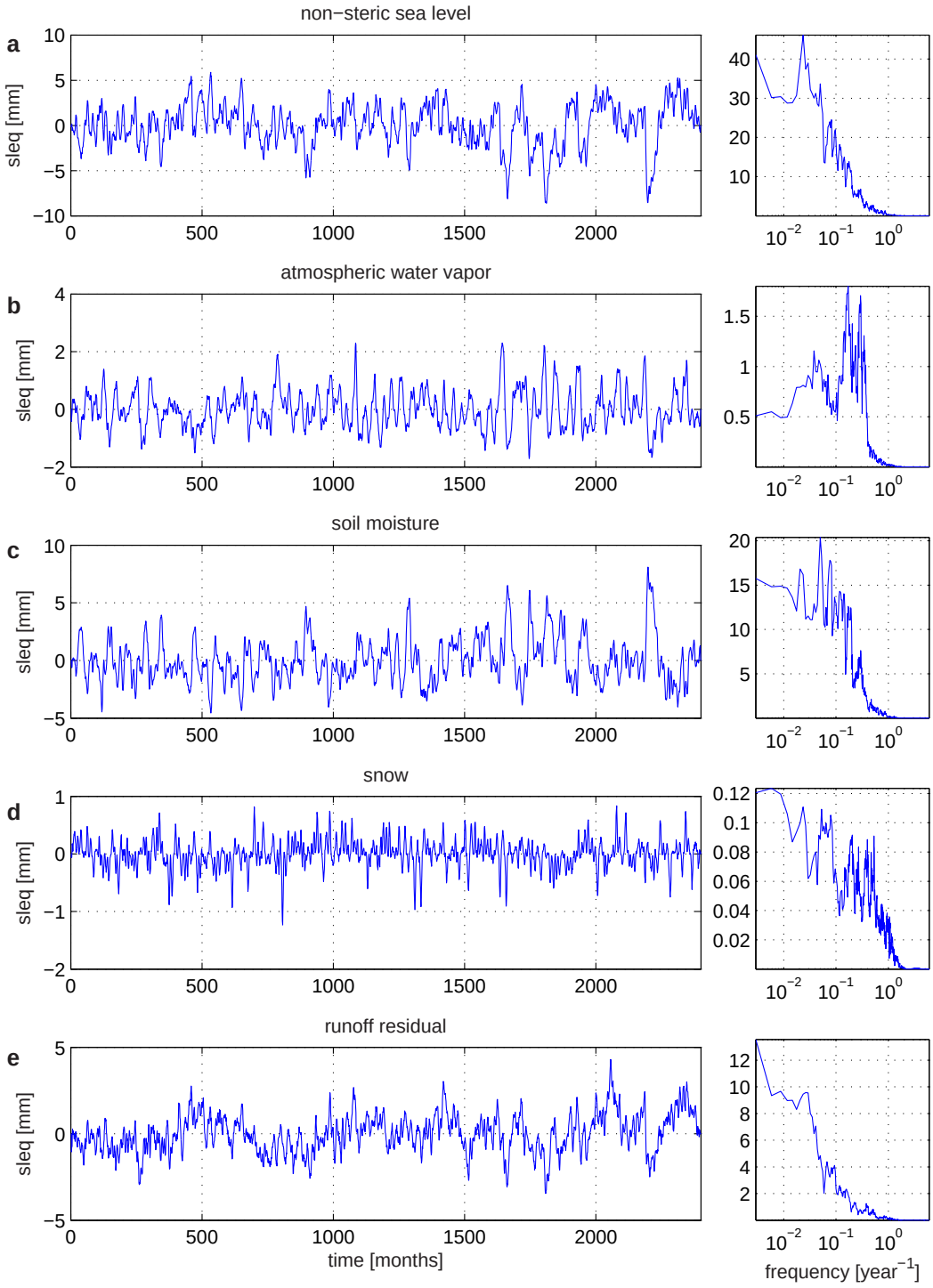

Figure 2.3: *Left panel: Non-seasonal monthly anomalies of eustatic sea level, atm. water content, soil moisture, snow, and 'runoff residual' (see text for discussion of this term); Units: mm of equiv. sea level height. Right panel: corresponding power spectral density of the time series on the left; frequency is given in years^{-1}.*

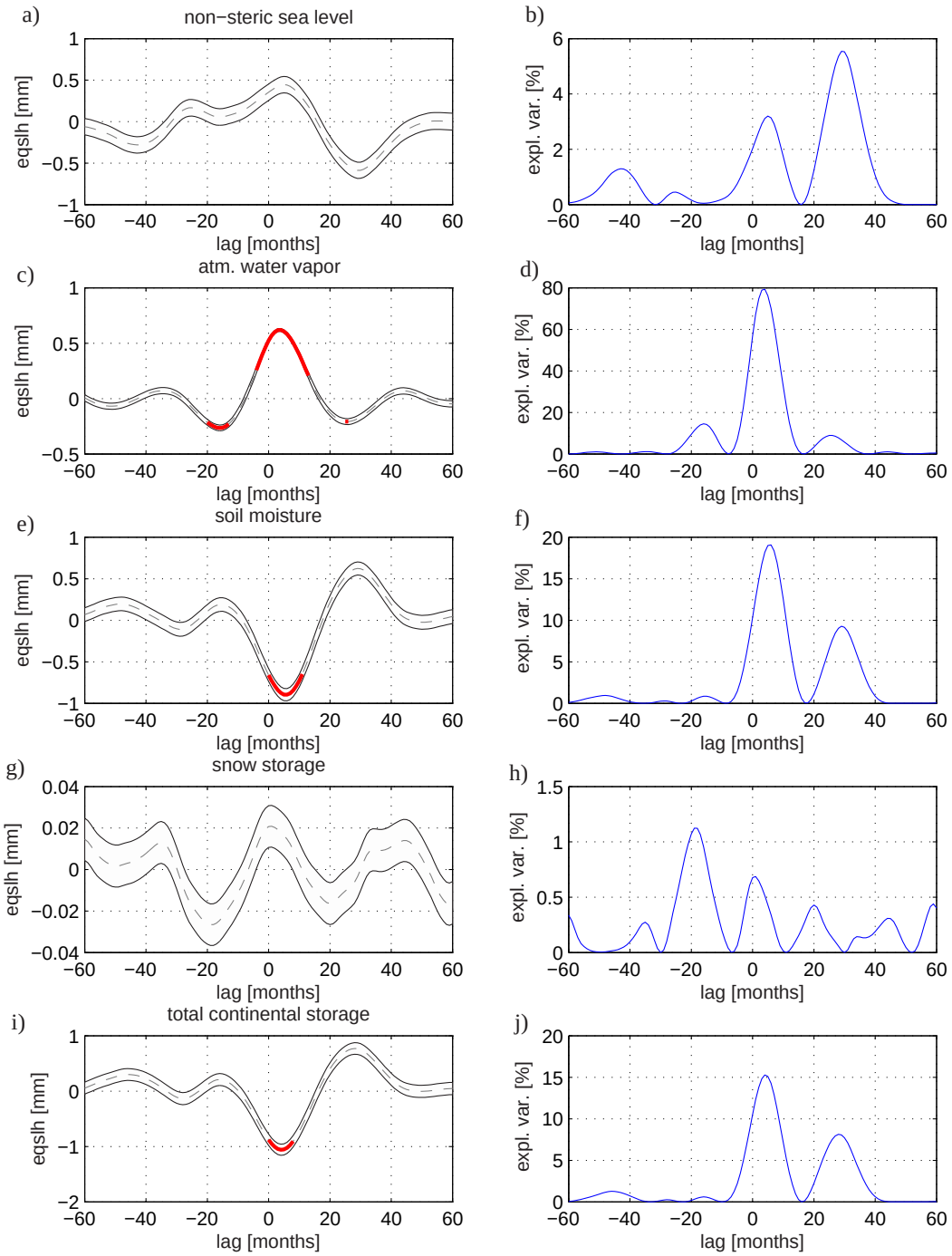

Figure 2.4: *Lagged regression coefficients (left panels) and explained variance (right panels) of eustatic sea level, atm. water vapor, soil moisture, snow and corrected continental storage (soil moisture + snow + 'runoff 'residual') on the Niño3 index. Solid red lines indicate that the regression coefficient is significant at the 95% level; the formal uncertainty of the regression coefficient is indicated by the shading.*

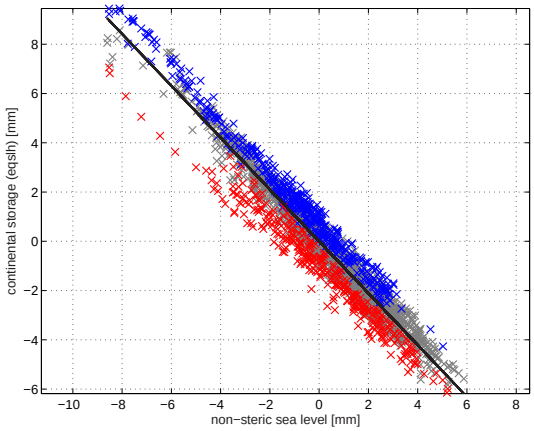

Figure 2.5: *Scatter plot of non-seasonal eustatic sea level vs. sea-level-equivalent soil moisture; five-month running mean applied. Blue colors indicate cold La Niña phases, and red colors warm El Niño phases (see also Fig. 2.1).*

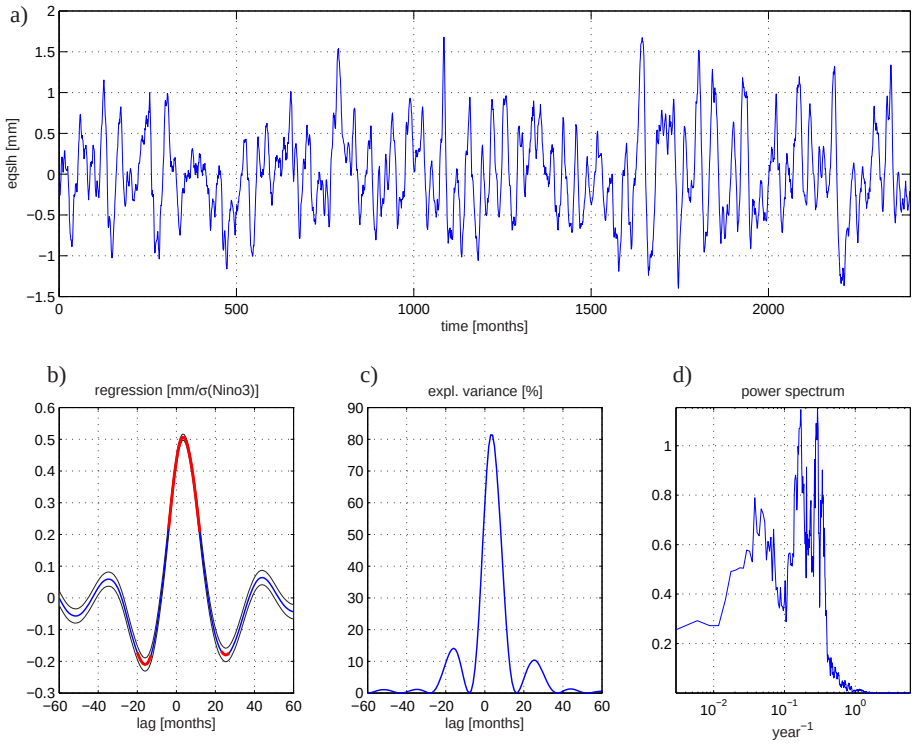

Figure 2.6: *Non-seasonal wet atmospheric loading signal over the oceans (sea level equiv. height); a) monthly non-seasonal anomalies; b) lagged regression on Niño3; c) explained variance of the regression; d) power spectrum.*

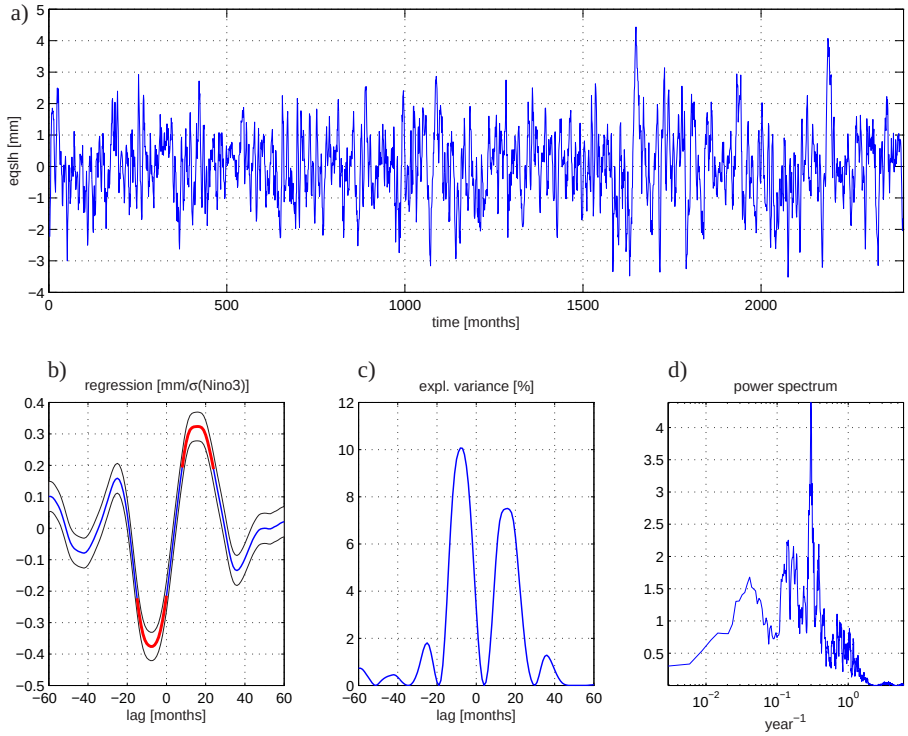

Figure 2.7: *Non-seasonal full (wet+dry) atmospheric loading signal over the oceans (sea level equiv. height); a) monthly non-seasonal anomalies; b) lagged regression on Niño3; c) explained variance of the regression; d) power spectrum.*

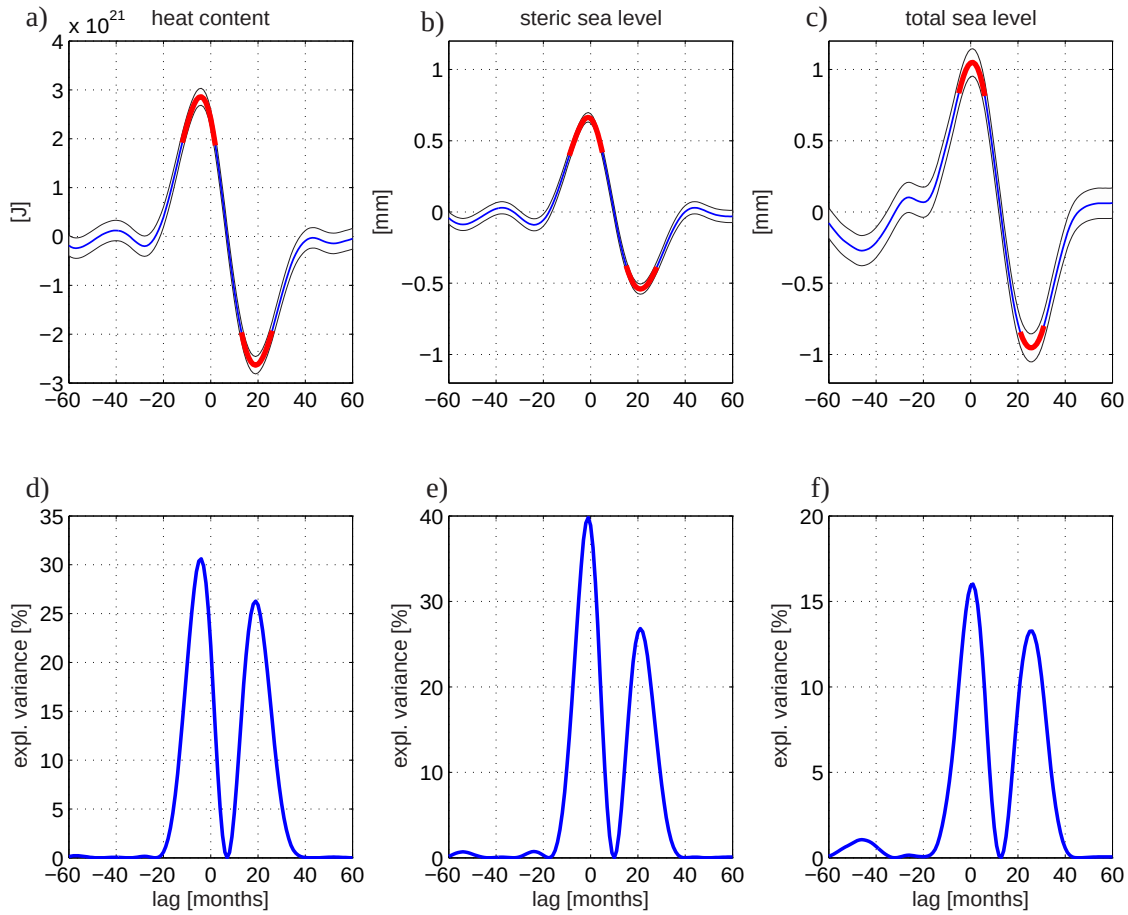

Figure 2.8: *Non-seasonal ocean heat content, steric sea level and total sea level (eustatic + steric) regressed on Nino3 for different lags. The red line indicates where the regression is significant above the 95% level.*

2.3.3 Regression of Non-Seasonal Global Loading Patterns on ENSO

So far, we have considered the integrated water storage anomalies of the individual reservoirs. This analysis yields information about eustatic global mean sea level (and thus ocean mass load) variability, but it does not resolve the local storage and loading anomalies. Also, dynamic ocean mass redistribution needs to be taken into account for the local ocean bottom pressure signal. In the following, we analyze the geographic pattern of sea level, water storage and bottom pressure anomalies, because the geographic location is essential for the computation of Stokes coefficients (Eq. 2.10).

Sea Level and Dynamic Ocean Bottom Pressure

While the eustatic sea level anomalies represent a uniform ocean bottom pressure anomaly, dynamic ocean mass redistribution leads to locally distinct bottom pressure signals. We start with analyzing the ENSO-related sea surface height anomalies, and estimate the dynamic bottom pressure anomalies from Eq. 2.7 (not including $\overline{\eta'_a}$ and $\overline{\eta'_Q}$). The sea surface height signal related to ENSO is well established (Nerem et al., 1999): during El Niño, sea level rises in the eastern and central Pacific Ocean, and falls in the western Pacific Ocean (Fig. 2.9 a). Since altimetric sea surface height is well correlated with heat content in the tropical Pacific Ocean region (Willis et al., 2004); this pattern mainly reflects the deepening and shoaling of the thermocline in the eastern/central and western Pacific Ocean, respectively. Accordingly, the simulated sea level signal is almost entirely explained by thermosteric anomalies (Fig. 2.9 c); halosteric anomalies, on the other hand, contribute very little to the sea surface height (Fig. 2.9 d). Only the western tropical Pacific Ocean features a noticeable halosteric anomaly of 2 mm/σ(Nino3), but this is still a factor 3 less than the corresponding thermosteric anomaly in this region.

Subtracting the steric from the dynamic sea level signal yields dynamic ocean bottom pressure. The largest bottom pressure signals appear on the shallow shelf areas (Fig. 2.9 e; we focus on the pattern lagging Nino3 by 4 months, because this is the dominant large-scale signal). On the Sunda shelf and on the shelves along the Australian north coast, bottom pressure changes are in opposite phase to ENSO with regressions up to -50 mm/σ(Nino3); on the Bering Sea shelf, bottom pressure changes are in-phase with ENSO, with a maximum amplitude of 20 mm/σ(Nino3). In the northwest Pacific Ocean basin we detect a small negative bottom pressure signal. This region is associated with relatively high bottom pressure variability, which resides largely in the semiannual period-band (Condi and Wunsch, 2004). Prominent signals are also visible northwest of Drake passage and southwest of Australia. While these regions are associated with large seasonal bottom pressure variability of 20 mm (RMS) (Condi and Wunsch, 2004), a smaller fraction of this

signal could arise from ENSO variability. From Figs. 2.9 a and e we can also conclude that ocean variability related to ENSO is mainly of baroclinic as opposed to barotropic nature, since there is little correspondence between the regression signals in sea level and dynamic bottom pressure.

An intriguing aspect of Fig. 2.9 e is the large scale pattern of positive bottom pressure anomalies in the Pacific Ocean, and negative anomalies in the Atlantic and Indian Oceans. It appears that the mass balance between these ocean basins is influenced by ENSO, although the amplitude of this large scale bottom pressure pattern is generally very small, with a maximum of only 2 mm. In their estimate of the ocean's seasonally varying *geoid* contribution, Wahr et al. (1998) found a qualitatively similar large scale pattern. The associated necessary mass transport between the basins is very small (about 4 orders of magnitude less than the typical Drake Passage transport (Wahr et al., 1998)). Our result here suggests that at least part of this inter-basin mass transfer is related to ENSO processes (or, more generally, related to tropical Pacific Ocean variability).

Except for the tropical Pacific Ocean and the Sunda and north Australian shelves, most of the large scale bottom pressure regression signals explain less than 5% of the non-seasonal bottom pressure variance. Along the tropical Pacific Ocean, the explained variance increases up to 30%, but the bottom pressure signals are very small at 0-4 mm/σ(Nino3); on the Sunda and north Australian shelves, the explained variance increases up to 55-60%, and the bottom pressure signals reach amplitudes of 40-50 mm/σ(Nino3). In previous work, we have shown that steric sea level changes arising from deeper ocean layers involve a horizontal mass redistribution within the ocean, and can thus contribute to regional mass load (and thus geoid) changes, contrary to what is sometimes stated (Landerer et al., 2007b). In particular, this mechanism can account for the high amplitude bottom pressure signal on the shallow shelf areas.

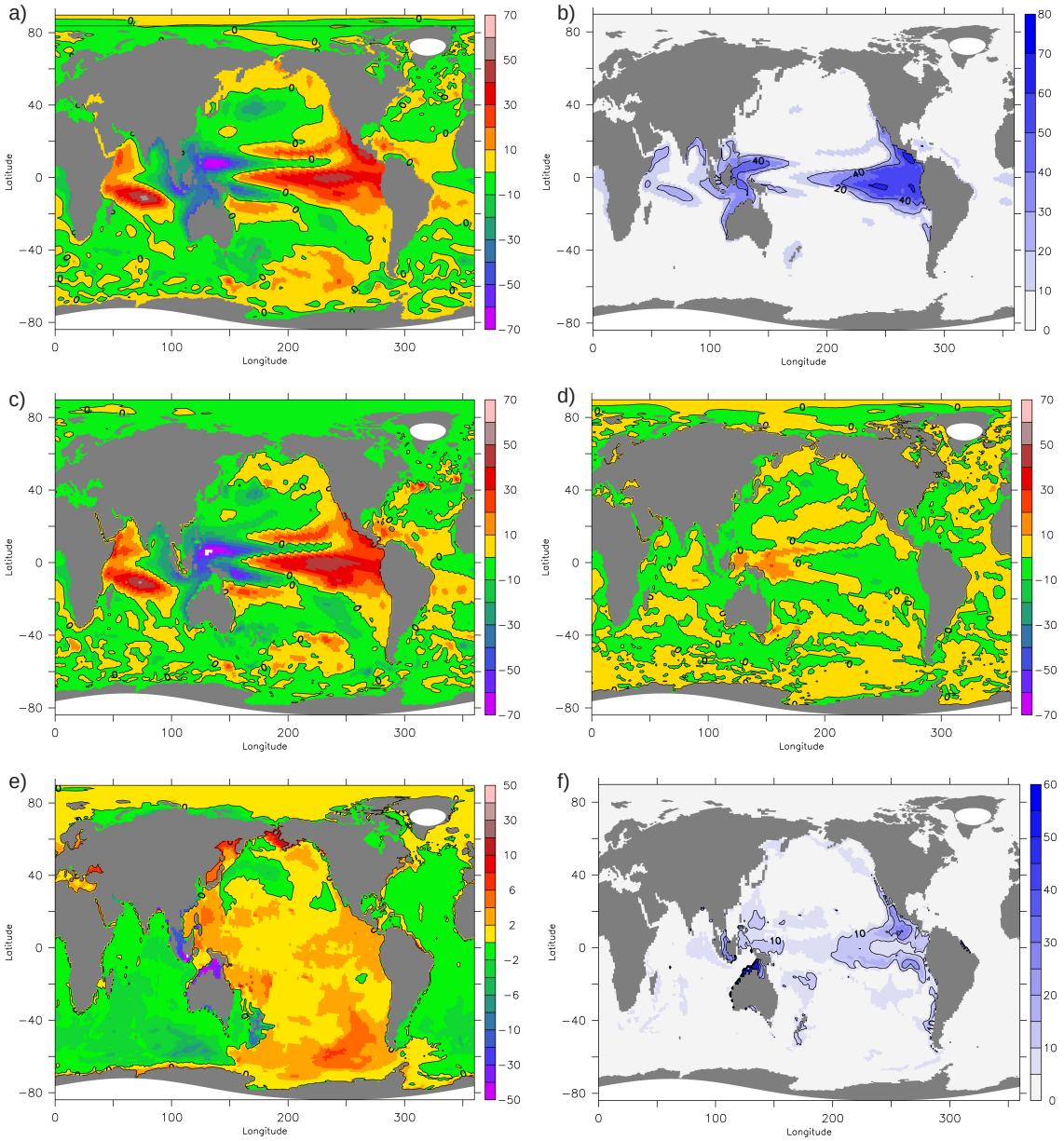

Figure 2.9: *Regression (mm / σ[Nino3]) on the Nino3 index of (a) non-seasonal dynamic sea level (lag=0), and (b) explained variance (in percent); Regression on the Nino3 index of non-seasonal (c) thermosteric and (d) halosteric sea level; Regression of non-seasonal (e) dynamic bottom pressure on the Nino3 index (Nino3 leading by 4 months), and (f) explained variance.*

Atmospheric Surface Pressure

As described in Sec. 2.2.1, atmospheric pressure variations over the oceans cause a spatially uniform mass load anomaly at the ocean bottom, and degree-two geopotential signals from this part of atmospheric variability can be accounted for with Eq. 2.14. The general pattern of the atmospheric surface pressure variations associated with ENSO is well established (e.g., Trenberth and Caron, 2000): during El Niño episodes, lower than normal pressure is observed over the eastern tropical Pacific and higher than normal pressure is found over Indonesia and northern Australia. During La Niña episodes, the pattern reverses: lower than normal air pressure covers Indonesia and the western tropical Pacific and higher than normal air pressure covers the eastern tropical Pacific. This pressure pattern is associated with the anomalous wind pattern described above, and ECHAM5/MPI-OM reproduces it well (Fig. 2.10 a, b). The dipole in the Southern Ocean and the negative anomaly in the northwest Pacific Ocean have large regression amplitudes, but the explained variance in these regions is below 5%.

As the integrated water vapor content was shown to be tightly coupled to ENSO, we estimate its contribution to the total surface pressure separately. The anomaly ENSO-related pattern of this wet atmospheric pressure closely resembles the shifts of precipitation patterns observed during El Niño: positive anomalies in the eastern and central Pacific Ocean, and negative anomalies in the western part and over Indonesia and Australia (Fig. 2.10 c). In the central tropical Pacific Ocean, the regression of vertically integrated water vapor reaches values up to 8 mm/σ(Nino3), with explained variance over 60% (Fig. 2.10 d). Negative regression values over Indonesia and Australia are generally smaller, and explained variances are below 5%. Over the central and eastern part of he tropical Pacific Ocean, the wet atmospheric pressure anomalies partly compensate the dry atmospheric pressure anomalies. However the general pattern and sign of the anomalous dry surface pressure pattern is not changed (e.g. the correlation between the pressure-based dry SOI and dry+wet SOI 0.87).

Continental Water Storage

In contrast to the pattern of atmospheric surface pressure, the large-scale pattern of continental water storage anomalies due to ENSO is less well established. Recent gravity-based measurements from GRACE are yet too short to give the full range of non-seasonal storage variability, but estimates of the seasonal water storage amplitude, e.g. in the Amazon basin, give values close to 400 mm water equivalent height (Schmidt et al., 2006). Here, we find that local continental water storage shows a large scale response of ENSO-related variability with amplitudes between -50 to 30 mm/σ(Nino3), indicating that ENSO modu-

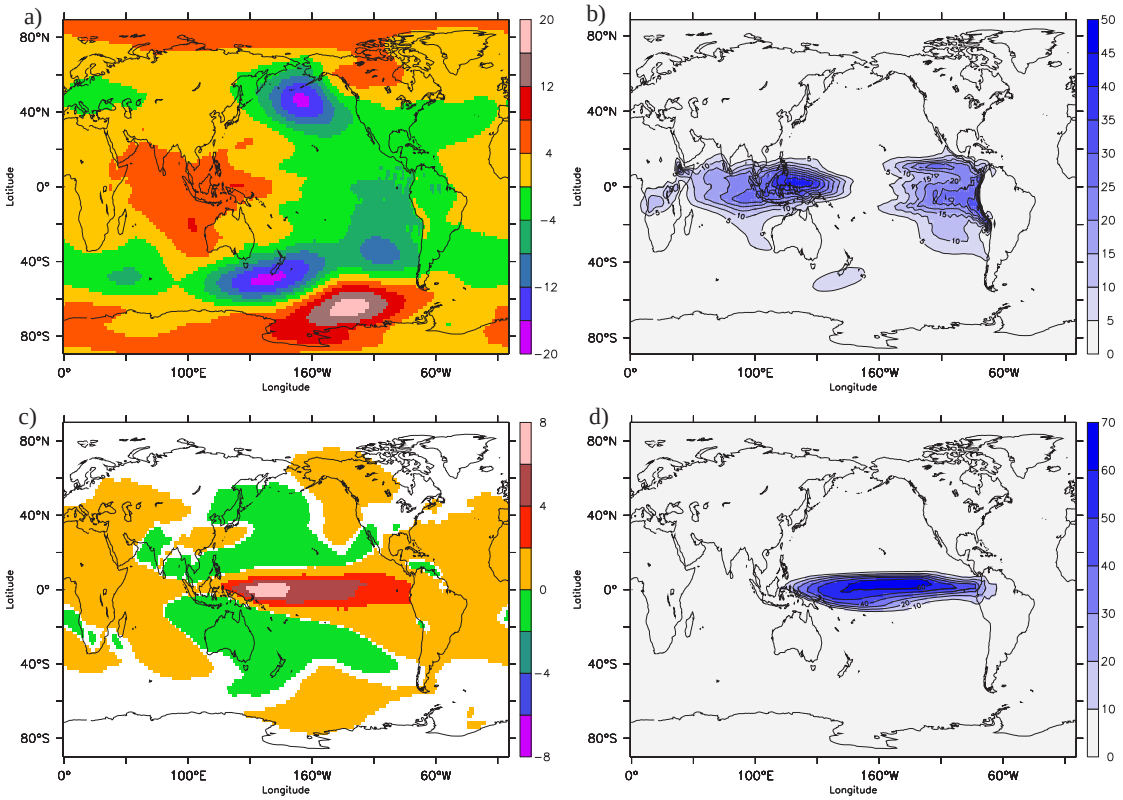

Figure 2.10: *Regression (mm / σ[Nino3]) on the Nino3 index of (a) non-seasonal atmospheric surface pressure anomalies (lag=0), and (b) explained variance (in percent); Regression on the Nino3 index of non-seasonal (c) wet atmospheric surface pressure anomalies (lag=0), and (d) explained variance (in percent).*

lated variability can substantially influence the climatological seasonal signal. The Amazon Basin, south-east Asia and parts of Africa have less soil water in phase with Nino3, while North America, south-eastern Europe, south-eastern South America and parts of western Africa have more soil water in phase with Nino3 (Fig. 2.11). This large scale pattern is roughly consistent with the typical precipitation anomalies expected during the warm and cold ENSO phases. The explained variance of the monthly soil moisture anomalies for these regions is between 10-20%, in parts of the Amazon basin the explained variance reaches up to 30-35%. Unlike soil moisture, the water equivalent snow depth anomaly pattern associated with ENSO is much more geographically confined (not shown). A small dependence of snow depth on ENSO with amplitudes of up to 0.03 m/σ(Nino3) between 0 and +3 months lag is detected in the western Canadian Coast Mountains (negative correlation with ENSO), and in the Himalaya (positive correlation with ENSO); however, the explained variance is always smaller than 10%, indicating that the largest part of the variability is driven by other processes. Note again that snow variability over the Antarctic and Greenland ice sheets is not included here. In principle we also have to account for the pattern of the 'residual runoff' term that was discussed in Sec. 2.3.2. Although we only know its globally integrated value, we can make some inference about its geographical distribution because it is related to the runoff field, but its grid point storage anomalies should be much smaller than those of the total runoff field. We find that the regression of the total runoff field on Nino3 leads to very small regression coefficients (largely well below 2 mm/σ(Nino3)), and the explained variance is negligible at less than 2-3% in most areas. It follows that the 'residual runoff' does not contribute significantly to ENSO-related local continental water storage (not shown).

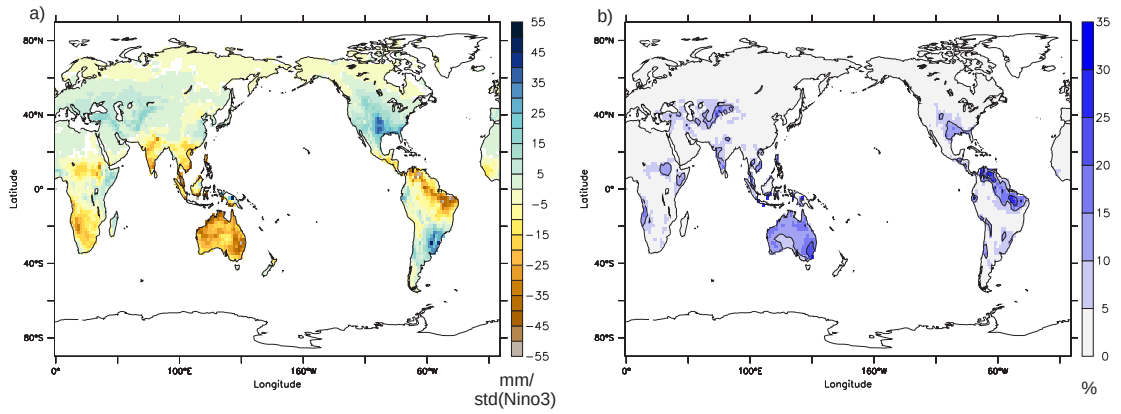

Figure 2.11: *a): Regression of non-seasonal soil moisture anomalies on the Nino3 index (Nino3 leading by 4 months; units: mm / σ[Nino3]); b): explained variance.*

Source	$\sigma(C_{21} \times 10^{-11})$	$\sigma(S_{21} \times 10^{-11})$	$\sigma(C_{20} \times 10^{-11})$
Total signal	1.53	2.66	3.80
Dyn. oc. bottom pres.	0.86	1.42	1.61
Atm. surface pressure	0.68	0.92	2.26
Continental storage	1.21	1.53	1.60
Non-Steric Sea Level	0.11	0.18	0.17
Wet oc. IB loading	0.03	0.04	0.04
Dry oc. IB loading	0.06	0.09	0.09
Combined uniform terms	0.12	0.19	0.18

Table 2.3: *Standard deviation (σ) of the non-seasonal degree-two Stokes coefficients from the combined, individual mass load, and uniform sea level terms (five-month running mean applied).*

2.3.4 Regression of Degree-two Stokes Coefficients on ENSO

We now consider the implications for the degree-two Stokes coefficients based on the individual water storage and mass redistribution signals described in the previous sections (except for the 'residual runoff' term, as its local grid point amplitudes of water storage are negligible).

As in the previous sections, all time series have been smoothed with a five-month running mean before projecting them on the Nino3 index. The non-seasonal root-mean square variability of the degree-two anomalies (separate contributions from all relevant terms and combined signal) is summarized in Table 2.3. The coefficients S_{21} and C_{20} feature larger variability than C_{21} (Fig. 2.12 and Tab. 2.3). While for C_{20} the largest contribution comes from atmospheric loading, S_{21} and C_{21} are mainly influenced by continental water storage, closely followed by dynamic ocean bottom pressure fluctuations. Similar amplitudes of non-seasonal degree-two Stokes coefficients are found by Chen (2005); the amplitudes of degree-two Stokes variations in our simulation at the seasonal time scale is similar to that reported by Chen and Wilson (2003) (not shown). The uniform eustatic and atmospheric ocean loading signals (Fig. 2.7) have a comparatively small contribution to the degree-two Stokes anomalies (Tab. 2.3). Since the total atmospheric signal is much larger than that due to atmospheric loading over the oceans, we conclude that most of the RMS variability of the total atmospheric degree-two Stokes signal is excited over land. Also, there is only minor compensation between the wet atmospheric ocean loading signal and eustatic sea level, because the larger fraction of the eustatic sea level anomaly is balanced with the continental storage (see Fig. 2.5). For the combined signal with all individual contributions taken into account, the single largest monthly degree-two anomalies are positive, but they do not occur concurrently in the different degree-two coefficients (Fig. 2.12). For the two strongest ENSO events in months 1650 and 2200 (see Fig. 2.1), there appears to be a

coherent response in S_{21} and C_{20}, but less so in C_{21}. In the following, we use the lagged regression analysis to project the continental, atmospheric and oceanic, as well as the total degree-two coefficients on the Nino3 index (Fig 2.13) to asses the individual contribution, as well as the total ENSO response.

Regression of C_{21}. For the combined C_{21} signal, the nominally largest contribution comes from soil moisture, but at no lag is the regression coefficient significant above the 95% level (Fig. 2.13 a). The contribution from atmospheric loading, ocean bottom pressure, and snow are about 180° out of phase compared to soil moisture, and they are all significant above the 95% level near zero lag. Thus, the ENSO signal in the full C_{21} coefficient is weak and not significant (Fig. 2.13 d), because the soil moisture signal destroys much of the robust signals from the other sources. Thus, the maximum explained variance for non-seasonal C_{21} anomalies in terms of ENSO variability is extremely low at about 2% (Fig. 2.13 g).

Regression of S_{21}. For the combined S_{21} signal, the largest contribution comes from dynamic ocean bottom pressure (Fig. 2.13 b), and this signal is significant above the 95% level for lags between -5 to +12 months. The soil moisture signal is slightly smaller, lags the ocean bottom pressure signal by about 5 months, and is significant only between lags of +4 to +10 months (Fig. 2.13 b, blue line). Atmospheric loading and snow storage are also significant, but only play a secondary role. Since the individual contributions are largely in phase near zero lag, the regression of the full S_{21} coefficient is much more robust than that of C_{21} (Fig. 2.13 e). The maximum regression of $1.5 \times 10^{-11}/\sigma$(Nino3) is reached at a lag of +4 months, with an explained variance of about 30% (Fig. 2.13 h). Note also that except for two months, all months where the Niño3 index is larger than two have a positive S_{21} anomaly at this lag (not shown).

Regression of C_{20}. For the combined C_{20} signal, the largest contribution comes from soil moisture, with a significant regression between lags of -2 to +13 months. The atmospheric loading contribution is about half that of soil moisture, and the signals are about 90° out of phase to each other (Fig. 2.13 c), so that overlapping significant lags are confined to near zero lag. Note that atmospheric loading has the largest contribution to non-seasonal variability in C_{20} (Tab. 2.3), but apparently much of it is not related to ENSO. Dynamic ocean bottom pressure and snow storage only contribute little to the total C_{20} signal (Fig. 2.13 c). Thus, the total C_{20} signal is largely determined by the amplitude and phase of the soil moisture anomalies, with a maximum regression of $1.3 \times 10^{-11}/\sigma$(Nino3) lagging the Nino3 index by 2 months (Fig. 2.13 f). However, the variance explained with ENSO of the C_{20} anomalies is relatively low at about 11% (Fig. 2.13 i).

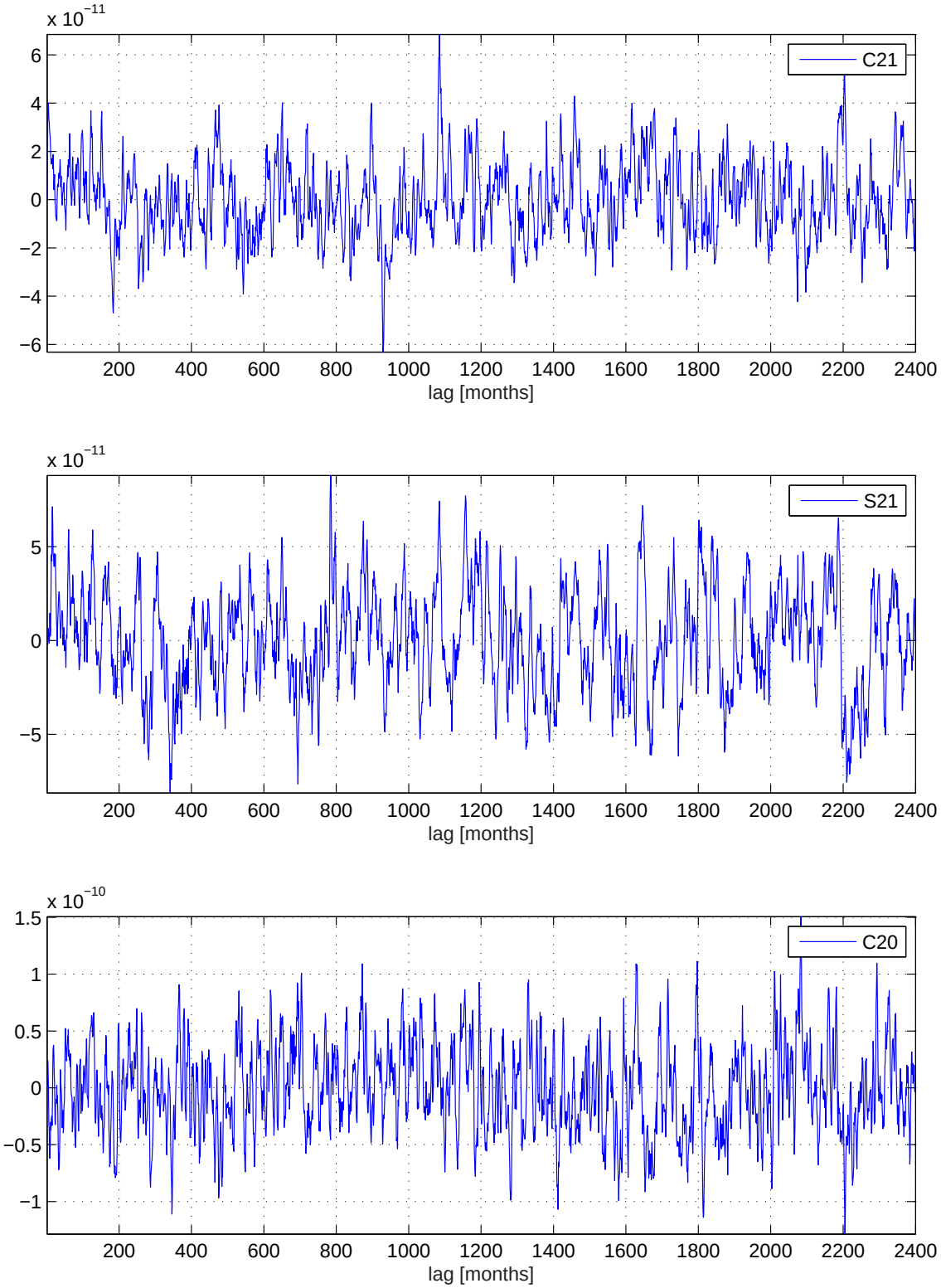

Figure 2.12: *Stokes coefficients: non-seasonal monthly anomalies (five-month running mean applied), with all storage terms included.*

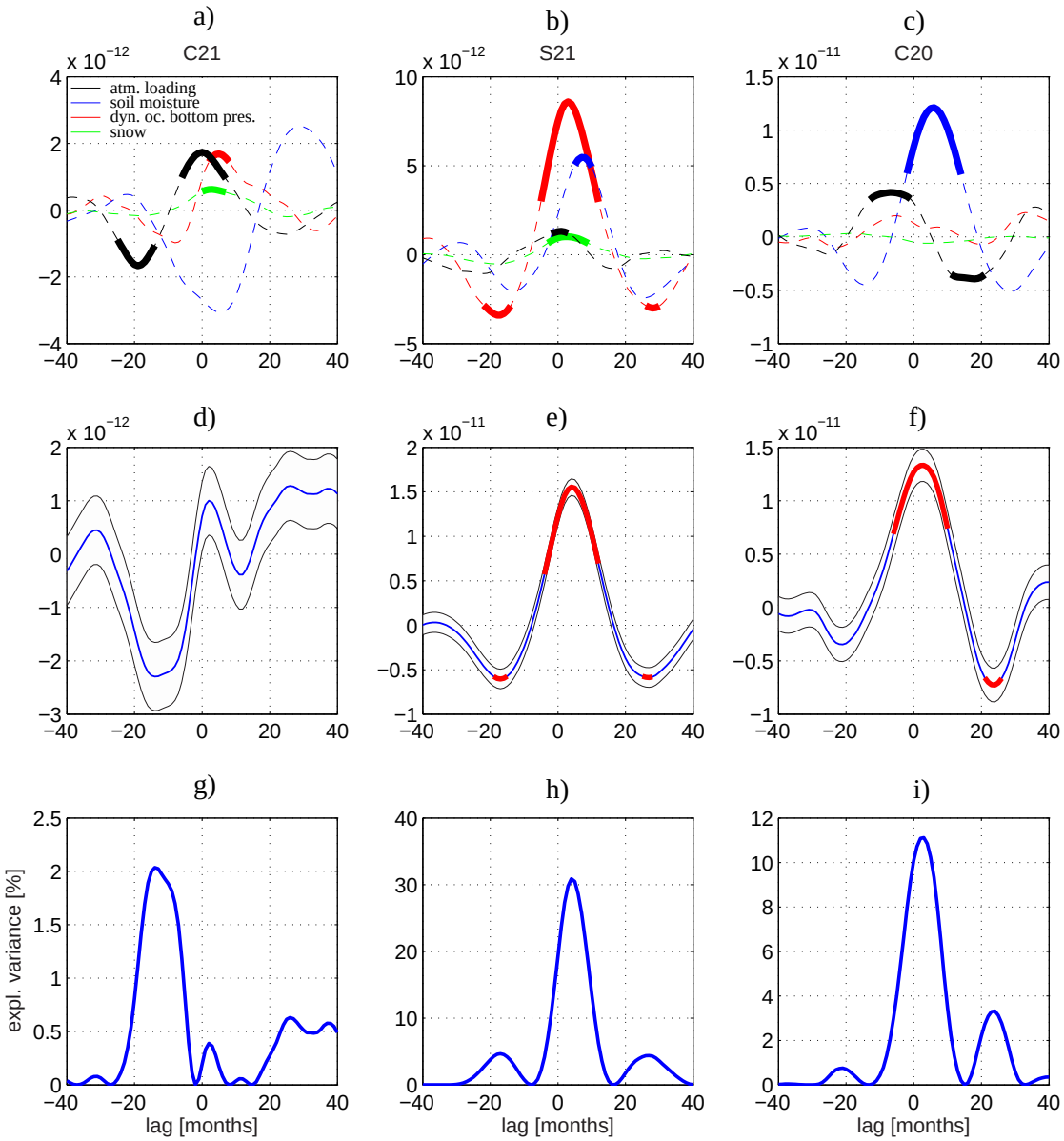

Figure 2.13: *Regression on Nino3 of the individual loading contributions to the non-seasonal Stokes coefficients, of the total Stokes coefficients, and variance explained (in percent) with ENSO of the non-seasonal Stokes coefficients: C_{21} (left row: a, d, g), S_{21} (middle row: b, e, h) and C_{20} (right row: c, f, i). The legend in a) applies to b) and c) as well; dynamic ocean bottom pressure does not include eustatic sea level. In d-f, the red line indicates significant a regression relationship at the 95% level.*

2.4 Discussion

In Sec. 2.3.1, we have demonstrated that an unconstrained coupled climate model without flux adjustments can faithfully represent the seasonal cycling of water between the oceans, atmosphere and continents. This is an important result in its own right, since a realistic seasonal representation is a prerequisite for any assessments of deviations thereof. In the remainder of this paper, we focused on deviations from the monthly climatological mean of steric sea level, eustatic level and the corresponding atmospheric and continental mass balance terms, focusing on ENSO related variability in the global mean of these signals, as well as their spatial distribution.

Integrated over the entire Earth, the atmosphere in ECHAM5 holds about 0.54±0.01 mm/σ(Nino3) more water (in equivalent sea level height), lagging the Nino3 index by +3 months. The increase of global mean atmospheric temperature with ENSO comes mainly from ocean heat loss to the atmosphere through evaporation, where subsequent increased condensation then leads to latent heat release and warming (Trenberth et al., 2002, 2005). The larger fraction of this column-integrated atmospheric water vapor anomaly resides over the tropical Pacific Ocean. Note that in our simulation, the regression of atmospheric water vapor on ENSO holds equally well for cold events (La Niña).

Intuitively, one might think that the positive atmospheric water storage would be balanced with negative eustatic sea level, as the water must evaporate from the oceans. However, our results lead to a different conclusion. We do not find a significant relationship between eustatic sea level and the Nino3 index. Instead, we find that the increased atmospheric storage is mostly balanced by continental water storage, which decreases accordingly at a lag of +3 months, leaving little room for a significant ENSO related eustatic sea level anomaly. However, ENSO effects explain only about 15% of the variance in continental water storage anomalies, either because water storage response to ENSO is not linear, or because other processes than ENSO have a considerable influence. Regardless of the ENSO state, the total atmospheric storage capacity is very limited through the dependence on temperature, while monthly anomalies of eustatic sea level and continental storage can have a much wider range of variability. Therefore, in the absence of other major sinks, eustatic sea level anomalies are almost entirely balanced by soil moisture changes, and the role of the atmosphere is that of a mediator between these two reservoirs. Figures 2.4 a and c represent the regression of time-integrated precipitation minus evaporation over the oceans and continents on Nino3, respectively. Based on this information, we can infer from Figs. 2.4 a and c that there is a general weak tendency during El Niño for reduced precipitation over the continents, and increased precipitation over the ocean which is largely balanced by increased evaporation over the ocean so that eustatic

sea level remains unchanged with ENSO on average.

However, some large ENSO events in our simulation appear to be associated with strong eustatic sea level and opposing continental storage signals: for example, the three largest ENSO events (months 1650, 1800 and 2190 in Fig. 2.1) have large anomalies in both eustatic level and soil moisture. Upon closer examination, the signals appear to be more related to cold La Niña phases following strong El Niños. For other periods, the distribution between soil moisture storage and eustatic sea level is not consistent with ENSO (Fig. 2.5). Global mean precipitation and evaporation anomalies in our simulation are highly correlated with ENSO, with 59% of the non-seasonal monthly variance explained by the Nino3 index (not shown). ENSO as an atmospheric mode can have a profound impact on the large scale precipitation patterns (Trenberth et al., 2002), but apparently this impact is not robust with respect to the geographical location over land or over ocean. Thus, we suggest that ENSO-related eustatic sea level anomalies can be of considerable size (5-7 mm over less than 3 years), but of either sign, or the partitioning of precipitation anomalies can be such that there is no considerable eustatic sea level at all. For steric sea level anomalies, we find a positive, albeit weak regression on ENSO of about 0.9 mm/σNino3, which is consistent with Willis et al. (2004) to within their and our uncertainties. Steric sea level anomalies also correlate positively in phase with atmospheric water vapor anomalies at about 0.29 in our simulation, which gives at least some weak support to the idea that increasing atmospheric water vapor decreases outgoing longwave radiation, and hence increases steric sea level with ENSO (Nerem et al., 1999). The contemporary rate of sea level rise is 3.1 ± 0.7 mm/yr determined from satellite altimetry (Solomon et al., 2007). Since our results suggest that ENSO related variability of eustatic sea level changes can be substantial, but of either sign, it appears there is no 'typical' ENSO response of global mean sea level. Removal of ENSO related sea level signals requires truly global measurements of all Earth system components, if one wishes to separate ENSO related signals from other, possibly anthropogenic, forcings on time scales of 3-8 years.

Another point to note is the relationship between eustatic and steric sea level, and continental water storage. Based on hydrological model simulations (forced with NCEP atmospheric reanalysis data) and global ocean temperature measurements, Ngo-Duc et al. (2005) reported a clear negative correlation (c=-0.84) between steric sea level and the land water contribution at decadal/interdecadal time scales based on 50 years of observational and model data. They explained this negative correlation with rising ocean temperatures leading to increased evaporation, and hence more precipitation over the oceans and land, constituting a negative feedback between steric and eustatic sea level. However, based on 200 years of monthly data from our simulation, we find only a very weak negative correlation of -0.15 between 5-month running mean anomalies of steric sea level and land

water storage, and no correlation based on 5-year averages.

In terms of time-variable gravity, our results show significant regressions of the S21 and C_{20}, but not the C_{21} coefficient on ENSO. In particular, we find that dynamic ocean bottom pressure and continental soil moisture storage are the most important contributors to ENSO-related anomalies in S_{21}. For C_{20}, we find anomalies in continental soil moisture storage to be the main contributor lagging Nino3 by seven months, followed by atmospheric surface pressure. Using a mixture of observations and independent model results, Cheng and Tapley (2004) also highlighted the importance of soil moisture anomalies for C_{20} qualitatively, but we can now quantify this contribution. In their attempt to trace back the origin of the observed 1997/1998 $J_2(= -\sqrt{5}C_{20})$ anomaly, Dickey et al. (2002) found a large contribution from dynamic ocean bottom pressure changes using the ECCO model. From our analysis we conclude that dynamic ocean bottom pressure changes can lead to non-seasonal C_{20} anomalies similar to those given by Dickey et al. (2002), but they do not appear to be significantly related to ENSO. This can, of course, also be a shortcoming of the ECHAM5/MPI-OM model. Recently, Song and Zlotnicki (2007) found signals in ocean bottom pressure in the high-latitude North Pacific in GRACE observations during 2003-04 and model simulations from years 1948-2004, and both observations and simulations appear to be well correlated to ENSO. Qualitatively, the pattern looks similar to the one we report here for this region (Fig. 2.9), but the explained variance of our signal is below 5%. Cox and Chao (2002) speculated that changes of the thermohaline circulation and structure, e.g. possibly related to high latitude sea ice melting, could cause dynamic ocean mass redistributions, which indirectly lead to J_2 anomalies, such as during 1997/1998. However, our results do not show significant bottom pressure anomalies in the Northern Atlantic or Arctic Ocean associated with ENSO; if such an ocean signal was the source of the observed 97/98 anomaly, it would thus most likely have no relation to ENSO. While some similarities in patterns of ocean bottom pressure anomalies are emerging in different models, more research is needed to assess their significance and dynamic link to large scale climate variability, such as ENSO.

We emphasize that it is the geographical *p*attern of water storage and mass load anomalies that matters for the degree-two Stokes signal, not so much the *s*ign of the individual integrated water reservoir anomalies. Also, as the individual reservoir and mass load contributions can be considerably out of phase, it is very important to include all of them in the analysis when comparing model results to observations.

2.5 Summary

We conclude this paper with a summary of our main results:

- A state of-the-art, fully coupled climate model with no flux-adjustments is now capable of simulating the seasonal water storage cycle between the oceans, atmosphere and continents. This is a necessary (though not sufficient) condition for the analysis of deviations from the seasonal cycle.

- The lagged regression analysis with the monthly anomalies of the individual hydrological storage reservoirs shows that in phase with ENSO, the atmospheric water vapor content increases, and the total global soil water storage anomaly is negative. Both signals are significant at the 95% level. The Nino3 index explains about 67% of the total atmospheric water vapor content. Snow storage is not significantly related to ENSO variability (not including Antarctic or Greenland ice sheets).

- The lagged regression analysis also shows that global eustatic sea level is not significantly related to ENSO variability at the 95% level.The global mean atmospheric loading over the oceans, which is equivalent to a uniform ocean bottom pressure signal, can have considerable amplitudes, but is not significantly related to ENSO variability either.

- Since eustatic sea level does not reflect the atmospheric water storage increase, the balance must be closed by reduced continental storage, mainly from soil moisture. This mechanism implies net precipitation and evaporation increase over the oceans, less precipitation over the continents, and consequently reduced continental runoff into the oceans in phase with Nino3.

- Steric sea level increases in phase with Nino3 by about 0.7 mm/σ(Nino3), but since the model underestimates seasonal ocean heat uptake, this value could also be too conservative. Total sea level variability related to ENSO is dominated by steric sea level, but can have a significant eustatic contribution. Thus, continued and improved fully global measurements are necessary to distinguish natural variability from anthropogenic sea level changes.

- The distribution of non-seasonal water mass load anomalies on Earth's surface leads to significant ENSO related changes in the S_{21} and C_{20} Stokes coefficients, but not to a significant change in the C_{21} coefficient. For S_{21}, the main contribution comes from the anomalous distribution of dynamic ocean bottom pressure, closely followed by soil moisture. For C_{20}, the main contribution comes from the anomalous pattern of soil moisture. Our results are not consistent with the attribution of the observed 1997/1998 C_{20} anomaly to ocean bottom pressure anomalies as a typical ENSO response, but instead point to the importance of continental water storage,

especially from soil moisture. However, the regression amplitude of C_{20} is still too small to explain the observed anomaly. Thus, we cannot rule out other excitation sources such as the solid Earth or the large Antarctic and Greenland ice sheets for the observed 1997/1998 C_{20} anomaly.

3 Regional Dynamic and Steric Sea Level Change in Response to the IPCC-A1B Scenario

Abstract

This paper analyzes regional sea level changes in a climate change simulation using the Max Planck Institute for Meteorology coupled Atmosphere Ocean General Circulation Model ECHAM5/MPI-OM. The climate change scenario builds on observed atmospheric greenhouse gas (GHG) concentrations from 1860 to 2000, followed by the International Panel on Climate Change (IPCC) A1B climate change scenario until 2100; from 2100 to 2199, GHG concentrations are fixed at the 2100 level. Compared to the unperturbed control climate, global sea level rises 0.26 m by 2100, and 0.56 m by 2199 through steric expansion; eustatic changes are not included in this simulation. The model's sea level evolves substantially different between ocean basins. Sea level rise is strongest in the Arctic Ocean due to enhanced fresh water input from precipitation and continental run-off, and weakest in the Southern Ocean due to compensation of steric changes through dynamic sea surface height (SSH) adjustments. In the North Atlantic (NA), a complex tripole SSH pattern across the subtropical to subpolar gyre front evolves, which is consistent with a northward shift of the NA current. On interannual to decadal timescales, the SSH difference between Bermuda and the Labrador Sea correlates highly with the combined baroclinic gyre transport in the NA, but only weakly with the meridional overturning circulation (MOC), and thus does not allow for estimates of the MOC on these timescales. Bottom pressure increases over shelf areas by up to 0.45 m (water-column equivalent), and decreases over the Atlantic section in the Southern Ocean by up to 0.20 m. The separate evaluation of thermosteric and halosteric sea level changes shows that thermosteric anomalies are positive over most of the world ocean. Due to increased atmospheric moisture transport from low to high latitudes, halosteric anomalies are negative in the subtropical NA and partly compensate thermosteric anomalies, but are positive in the Arctic Ocean and add to thermosteric anomalies. The vertical distribution of thermosteric and halosteric anomalies is highly non-uniform between ocean basins, reaching deeper than 3000 m in the Southern Ocean, up to 2200 m in the North Atlantic, and only to depths of 500 m in the Pacific Ocean by the end of the 21st century.

3.1 Introduction

The relative sea surface height (SSH) directly reflects the three-dimensional, large scale ocean circulation. On time scales exceeding a few days and length scales larger than 50 km, theory shows that the SSH adjusts to the motions in the deep layers (Wunsch and Stammer, 1998). From the viewpoint of classical oceanography, dynamic SSH is equal to depth integrated specific volume anomalies (when referring to dynamic SSH, we tacitly assume that the geopotential units $m^2\ s^{-1}$ have been converted to geometric distance). The attribute 'dynamic' refers to the geostrophic balance between horizontal flow and SSH gradients or, equivalently, pressure gradients, such that the flow is parallel to contours of equal SSH (Gill, 1982). In most regions of the world ocean, the horizontal pressure gradients do not extend to the ocean bottom; they vanish at some depth due to density compensation, and cause an inverse correlation between SSH and pycnocline depth: a high sea level indicates a deep pycnocline, and vice versa. SSH changes can equivalently be interpreted in terms of the integral response to anomalies of the vertical density distribution (through temperature and salinity variations), in which case the attribute steric is commonly applied to describe these changes. We use the term 'steric' here strictly as pertaining to the temperature, salinity and pressure dependent specific volume of the ocean.

The two perspectives on sea level changes - dynamic and steric - are intimately linked: a local change in the density distribution through temperature and salinity anomalies will alter the horizontal pressure gradients and therefore will be balanced by geostrophic velocity anomalies. Large scale circulation changes, on the other hand, may redistribute characteristic water masses, and thus lead to different steric sea level changes regionally.

One of the most striking features of the present day sea surface topography is the low sea level in the North Atlantic relative to the North Pacific (Reid, 1961; Rio and Hernandez, 2004), a result of the denser deep water formed in the North Atlantic as part of the Atlantic meridional overturning circulation (MOC). If this deep water formation rate was decreased or if the deep water formed became less dense, sea level rise in the North Atlantic region would be expected to be stronger than the global average (Levermann et al., 2005). Since SSH reflects the thermohaline structure and the strength of ocean gyres, it might then be possible to use altimetric SSH observations to asses the state and transport strength of the Atlantic MOC (Häkkinen, 2001). Observations of SSH anomalies from space have been analyzed in connection with heat content changes in the North Atlantic (Häkkinen, 2001; Antonov et al., 2005), the North Atlantic Deep water (NADW) formation rate, and the strength of the thermohaline part of the MOC (Häkkinen, 2001). However, detecting MOC changes through SSH measurements depends on the magnitudes and timescales of

all adjustment processes that influence SSH in a climate change scenario. Mechanisms that influence regional SSH changes have been alluded to in a number of model studies (e.g. Mikolajewicz et al., 1990; Bryan, 1996; Knutti and Stocker, 2000; Mikolajewicz and Voss, 2000; Gregory et al., 2001; Levermann et al., 2005), but the spatial patterns of predicted SSH changes by various models are still inconsistent with each other (Gregory et al., 2001). Thus, there is still considerable need to understand the physical processes behind regional SSH changes to put model differences into perspective. In particular, it is important to understand the connection between SSH variations and important climate indices, such as the transport strength of the Atlantic MOC.

Variations of regional SSH caused by a redistribution of water masses and ocean circulation changes have a near-zero global mean (minor variations arise only from non-linearity in the equation of state). Global sea level rises when the absolute mass of the ocean water is increased (eustatic sources), through variations of the global mean salinity (which depends on eustatic sources, with the exception of melting sea ice), or when the specific volume is modified through net heating or cooling. The ocean heat content would change due to a planetary energy imbalance (Levitus et al., 2000). The issue of global sea level rise has received considerable attention in the last decade (e.g. Gregory et al., 2001; Antonov et al., 2002; Munk, 2002; Cazenave and Nerem, 2004; Antonov et al., 2005). There is, on the other hand, still a lot of uncertainty about the causes of observed global sea level change. This 'enigma' (Munk, 2002) relates to the many unknowns, which introduce large uncertainties in the calculation of a relatively small number. A rise due to ocean warming for the period 1993-2003 has been estimated at 1.6 mm yr^{-1} for the upper 3000 m of the World Ocean, whereas measurements from satellite altimetry suggest an increase of 3.1 mm yr^{-1} for the same period (Antonov et al., 2005), leaving a residual of 1.5 mm yr^{-1} to be accounted for by non-thermosteric effects. Assuming a constant or near constant global mean salinity, halosteric sea level changes are of second order globally, but can be very important regionally due to anomalous fresh water fluxes (Antonov et al., 2002). Interannual to decadal variability of local and global rates of sea level change are significant (Willis et al., 2004; White et al., 2005; Church et al., 2005) and complicate the detection of trends. Gregory et al. (2004) have pointed out, however, that the amplitude of this variability is possibly very sensitive to the treatment of data uncertainties in sparsely sampled regions.

The present study focuses on the analysis of simulated regional sea level changes in response to the IPCC A1B scenario (IPCC, 2001) from two perspectives: firstly, sea level is analyzed in terms of relative, dynamic SSH changes, and the connection of these regional and interbasin SSH adjustments to important oceanic transport indices, such as the MOC and the baroclinic gyre transport in the North Atlantic. Secondly, we calculate SSH changes due to steric effects from temperature and salinity anomalies, estimating the

influence of each property separately on a regional basis, and also with respect to the steric contribution from each depth layer for different ocean basins. These results then provide a reference estimate of regional thermosteric and halosteric sea level anomalies in connection to large scale ocean circulation changes in a realistic climate change simulation. Decadal heat storage variability through volcanic aerosol forcing (Church et al., 2005) and the contribution of eustatic sources (glacial melting and land storage) are not taken into account in our simulation. The simulations were performed using the fully coupled atmosphere ocean circulation model ECHAM5/MPI-OM developed at the Max Planck Institute for Meteorology.

The paper is organized as follows: In section 3.2, we describe the main features of the coupled model, the mean state of the model's SSH in comparison with observations, and the climate scenario that was used for the perturbation simulation. Section 3.3 focuses on the spatial patterns of sea level change, and the link of these to large scale circulation changes, such as the reduction of the Atlantic MOC and the North Atlantic baroclinic gyre transport. In section 3.4, we analyze steric sea level changes, and calculate the bottom pressure anomalies and the contribution of temperature and salinity induced steric changes separately. Conclusions are given in section 3.5.

3.2 Model description, mean state and scenario response

3.2.1 The ECHAM5/MPI-OM coupled model

Our analysis uses results from climate change simulations that are performed with the coupled ECHAM5/MPI-OM atmosphere-ocean general circulation model. The ocean component MPI-OM uses an orthogonal curvilinear grid with its North Pole shifted to Greenland to avoid a singularity at the geographical North Pole. The vertical resolution is 40 z-levels, 20 of which are distributed over the upper 700 m; partial grid cells resolve the bottom topography. Horizontally, the resolution gradually varies between 12 km near Greenland and 180 km in the tropical Pacific. MPI-OM (Marsland et al., 2003) is coupled to the ECHAM5 atmosphere model (Roeckner et al., 2003) at T63 resolution with 31 vertical levels; no flux adjustments are applied. A dynamic/thermodynamic sea ice model with viscous-plastic rheology is embedded in MPI-OM. More details on the ocean model formulation can be found in Marsland et al. (2003) and Jungclaus et al. (2006). Here, we focus on some main features of MPI-OM that are pertinent for the following analysis. MPI-OM uses a prognostic free-surface formulation for the calculation of the SSH ζ. The vertically

integated continuity equation in the Boussinesq approximation reads

$$\frac{\partial \zeta}{\partial t} + \frac{\partial U}{\partial x} + \frac{\partial V}{\partial y} = Q_\zeta(x, y) = P - E + R, \tag{3.1}$$

where U and V are vertically integrated zonal and meridional flows, respectively. The forcing term $Q_\zeta(x, y)$ represents surface freshwater flux due to precipitation (P), evaporation (E) and river run-off (R). River discharge is calculated from the hydrological discharge model from Hagemann and Dümenil (1998), with the limitation that melting of land ice is not considered, effectively excluding eustatic sources in the simulations. To close the mass balance over glaciers, snowfall onto the glaciers is redistributed to the nearest ocean point immediately. At time steps of one month, the prognostic SSH field is recentered to a zero global mean. The continuity equation (3.1) implies volume conservation (Gill, 1982) in the ocean; this formulation yields correct relative horizontal SSH gradients, but a spatially uniform time-varying correction term must be applied in order to adjust the sea level for any net expansion or contraction through changes in the local density structure (Greatbatch, 1994). This term is commonly referred to as the 'steric sea level effect'. More precisely, given that Q_ζ is close to zero when averaged over the global oceans, and that eustatic mass sources are excluded, the global mean salinity will be constant and any net global volume change will be due to changes in ocean temperature only. For its central role in the force balance of geostrophic surface flow, we will refer to the sea level pattern relative to a zero global mean as 'dynamic SSH'.

3.2.2 Model mean state

An unperturbed control simulation is forced with preindustrial greenhouse gas concentrations and serves as a reference for the calculation of changes in ocean circulation and sea level. A detailed description of the general model behavior in terms of comparison with observed ocean properties can be found in Jungclaus et al. (2006). Here, we focus on the processes that control and influence the sea surface topography, both in terms of relative SSH gradient changes, and changes of the global mean. The control simulation exhibits a global mean sea level drift of about 0.4 mm yr^{-1} due to a slow warming of intermediate and deep waters (Jungclaus et al., 2006), which is mainly due to insufficient Antarctic Bottom Water (AABW) formation with correct water mass properties in the model (Jungclaus et al., 2006). The cold AABW cell weakens in the control simulation, thus causing a relative warming of these waters. The ACC region, consistently, experiences a small positive dynamic SSH drift of $\approx$0.15 mm yr^{-1}. In comparison, the drift of the dynamic SSH field in the other ocean basins is at least an order of magnitude smaller (not shown). As we will show in section 3.3, the relative regional SSH changes due to greenhouse gas

(GHG) forcing are 1-2 orders of magnitude larger than any control simulation drift. We thus consider the model's mean dynamic SSH pattern as sufficiently stable in time and use it as a reference for the computation of anomalies.

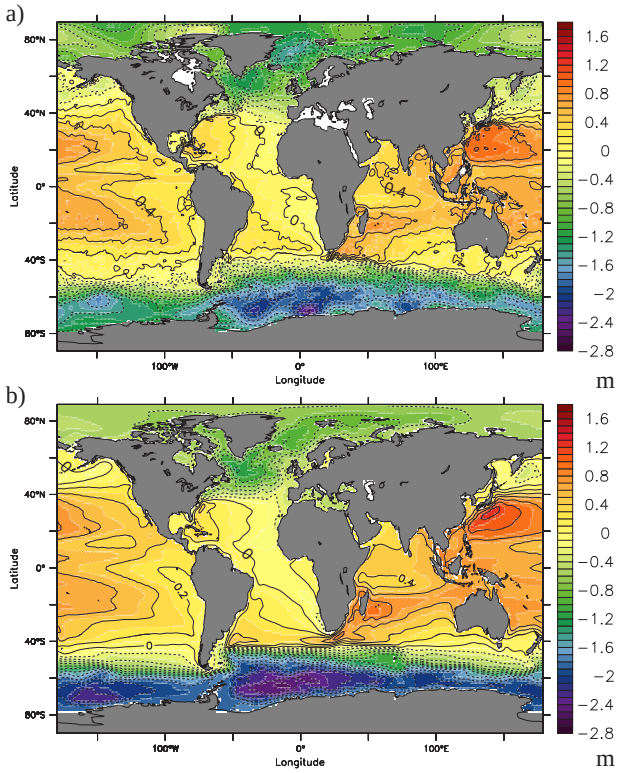

Figure 3.1: *Relative sea surface height (SSH, in meters): (a) Combined Mean Dynamic Topography CMDT-RIO03 from Rio and Hernandez (2004), and (b) mean free surface topography from the control simulation. Both fields are adjusted to zero global mean; the contour line interval is 0.2 m.*

The Combined Mean Dynamic Topography (CMDT) data set (Fig. 3.1a), which is derived from satellite altimetry, in situ measurements, and a geoid model for the averaging period 1993-1999 (Rio and Hernandez, 2004) provides a reference for the dynamic SSH pattern of MPI-OM. The control run of MPI-OM reproduces the main SSH features well (Fig. 3.1b); the largest deviations between the two SSH fields occur in regions of strong currents with high spatio-temporal variability, such as the Gulf Stream, Kuroshio and South Atlantic subpolar gyre. The relative sea level difference between the North Atlantic and North Pacific averaged from 40-65°N over each ocean basin amounts to 0.78 m in our control simulation, compared to 0.72 m in the CMDT data set over the same region. Since barotropic (depth averaged) and baroclinic flows determine local SSH gradients, discrepancies between our model SSH and the CMDT data set arise from insufficiently or inaccurately resolved dynamics in MPI-OM. The North Atlantic Current follows the

45°N latitude band across the Atlantic in our simulations. It is thus located too far south and too zonal in comparison to observations, an issue that is most likely linked to insufficient topographic resolution (Jungclaus et al., 2006). Furthermore, one formation site of North Atlantic Deep Water (NADW) in MPI-OM is located in the southern Labrador Sea, whereas the observed NADW formation takes place further north in the Labrador basin. Deep convection areas are manifested in SSH maps as local minima due to the high density; hence, observed and modeled SSH minima in the North Atlantic do not coincide (Fig. 3.1a and b). In the southern hemisphere, the simulated mass flux of 165 Sv through Drake Passage (Jungclaus et al., 2006) is more than observational estimates of 118-140 Sv (e.g. Whitworth et al., 1982). The SSH gradient from the South Atlantic across the ACC is too steep when compared to observations (Fig. 3.1a and b). This is caused by the cyclonic Weddell Sea gyre, which appears to be too strong in MPI-OM (Jungclaus et al., 2006). Uncertainties of observed SSH in high latitudes regions (above ≈65°) are still relatively large, since satellite altimetry is not available and coverage with hydrographic profiles in the polar regions is comparatively poor (Rio and Hernandez, 2004).

The control integration yields a mean of 19.1±1.1 Sv for the simulated maximum Atlantic MOC at 30°N. This compares to observational estimates of 18±4 Sv (Macdonald, 1998), 18 Sv (Talley, 2003), and 15±2 Sv (Ganachaud and Wunsch, 2000). Maximum global poleward heat transports in MPI-OM reach 1.8 PW near 26°N in the Northern Hemisphere, and -1.7 PW near 10°S in the Southern Hemisphere. For the Atlantic basin, the simulated heat transport of 1.15 PW at 20°N is slightly lower than the 1.27±0.15 PW derived from inverse calculations by Ganachaud and Wunsch (2003). The simulated sea ice extent and its seasonal variation compares favorably with observations (Jungclaus et al., 2006).

Coupled models that do not apply any flux adjustments have deficiencies due to insufficient resolution and/or unresolved processes. In ECHAM5/MPI-OM, deep ocean drift and a lack of Antarctic Bottom and Intermediate Water formation appear to be the most relevant challenges for the simulation of sea level changes (Jungclaus et al., 2006). We will show, however, that the simulated climate change signals are robust features. Within the constraints and limitations mentioned, we are thus confident that there is a certain amount of 'realness' to our results.

3.2.3 Model scenario response

Our analysis is based upon a realization of an Intergovernmental Panel on Climate Change (IPCC) scenario simulation. The coupled experiments were conducted with transient greenhouse gas concentrations and aerosol forcing from preindustrial to present day val-

ues for the period from 1860 to 2000 ('20th century'), followed by the IPCC SRES-A1B scenario (IPCC, 2001) with increasing trace gases and aerosol concentrations from 2001 until 2100. The simulations are then extended for another 100 years with greenhouse gas concentrations fixed at the 2100 level, e.g. CO_2 is at 703 ppmv (Fig. 3.2). This prescribed forcing leads to global mean surface temperature anomalies of 1.7°C by 2040-2060, and 3.4°C by 2080-2100 in the A1B scenario. A transient 1% CO_2 increase simulation with the same model configuration of ECHAM5/MPI-OM yields an effective climate sensitivity of $\sigma_{\text{eff}} = 0.83$ K W^{-1} m^{-2} (Roeckner, personal communication).

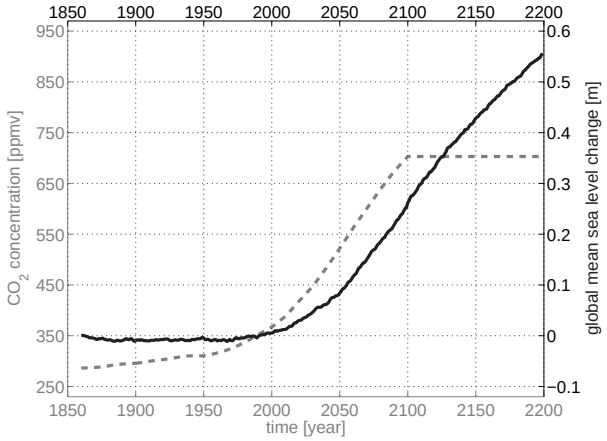

Figure 3.2: *Grey line: atmospheric CO_2 concentration in the 20th century (1860-2000), the A1B scenario simulation (2001-2100), and for the period afterwards (2101-2199); black line: global mean sea level rise in response to the prescribed CO_2 forcing.*

The MOC in the North Atlantic shows no trend in the 20th century simulation, but does exhibit multidecadal variability with amplitudes between 18 Sv and 24 Sv. After the year 2000, however, the Atlantic MOC at 30°N gradually decreases by 25% from its initial mean strength of 19 Sv to 14.5 Sv at the end of the 21st century. The mechanisms that determine the MOC response to greenhouse gas forcing involve air-sea buoyancy fluxes and the advection of salt and temperature anomalies in the ocean (Thorpe et al., 2001). Consequently, a change in ocean circulation pattern and intensity causes a massive redistribution of water mass properties, resulting in significant differences of regional sea level responses. The adjustment of regional SSH will be the focus of our analysis and is described in detail in section 3.3.

While there is only little change until 1960, global mean sea level then rises slowly until 2010 (Fig. 3.2). It then strongly accelerates in the 21st century, rising to a total of 0.26 m by 2100. This implies that the net heat flux into the ocean is increasing steadily (Gregory et al., 2001). Global sea level continues to rise an additional 0.30 m from 2100 to 2199 at stabilized GHG concentrations due to the large heat capacity of the oceans, which continue

to take up heat and hence expand (Meehl et al., 2005), albeit at a slightly decreasing rate (quadratic fit of the control run subtracted; by subtracting the control from the scenario simulation to obtain anomalies, we implicitly assume a linear separability of drifts).

Based on in-situ temperature observations from pentadal composites for the 1955-1959 through 1994-1998 period for the 0-3000 m layer, the global thermosteric linear trend is 0.40 ± 0.05 mm yr^{-1} (Antonov et al., 2005), corresponding to a heat input of 14.5×10^{22} J (Levitus et al., 2005). Our simulation yields a similar global sea level trend of 0.34 ± 0.09 mm yr^{-1} for the same period, but a considerably lower net heat increase of 8.1×10^{22} J. The underestimate of heat uptake might be linked to the too warm deep and intermediate waters in MPI-OM (see section 3.2.2), with the more efficient thermal expansivity at higher temperatures causing a similar global mean sea level rise somewhat by chance. Apart from seasonal variations, Antonov et al. (2005) also observed decadal variability of ocean heat storage, and thus thermosteric sea level change. Church et al. (2005) linked volcanic eruptions with significant decadal variability of ocean heat content and global mean sea level (up to 3×10^{22} J and 5 mm, respectively); our simulation does not include volcanic forcing, and thus cannot represent this effect.

A particularly large climate response occurs in the Arctic Ocean in our simulation: it becomes largely ice free during the summer by 2070, reducing the total annual mean arctic sea ice volume gradually from 3×10^4 km^3 to less than 1×10^4 km^3. We give an order of magnitude estimate of the effects of the inferred freshening to the halosteric anomaly in the Arctic Ocean in section 3.4.

The analysis presented in the following sections is based on annual mean values. Since we are interested in the transient changes under the SRES-A1B scenario, seasonal variability, which is mostly due to air-sea heat and fresh water exchange that affects the upper 100 to 200 m of the water column, is not considered.

3.3 Spatial pattern of SSH adjustments

In this section, we describe and explain SSH changes in the aforementioned scenario integration. The meridional SSH gradient in the Atlantic basin has been associated with the strength of the Atlantic MOC (Thorpe et al., 2001). Another perspective was introduced earlier by Bryan (1996), who described a distinct dipole pattern of sea level change in the western North Atlantic, which he inferred to be consistent with a weakening of the upper branch of the Atlantic MOC once an allowance is made for changes induced by the wind-driven circulation. Decadal variability of SSH in the western North Atlantic has been proposed to reflect predominantly overturning changes through the topographic coupling between depth averaged and baroclinic flows (Häkkinen, 2001). As Gregory et al. (2001) in

their analysis of previous IPCC results have pointed out, most simulated regional sea level changes differed significantly from the global average, but there was a considerable lack of agreement about the distribution of these regional patterns between various models, with only two robust exceptions: firstly, a maximum increase of sea level in the Arctic Ocean due to enhanced fresh water input, and secondly, a minimum reduction of sea level in the Southern Ocean. In the open ocean basins, where geostrophy holds, the change of local and basin scale sea level gradients is a direct measure of large scale circulation changes (Gregory et al., 2001); hence, discrepancies in local sea level change between different model simulations are caused by differences in large scale circulation patterns and deep water formation rates. This, in turn, directly determines the local water mass properties, and hence the steric response through temperature and salinity changes. We will elaborate on this point in section 3.4. Here, we will first describe the global pattern of dynamic sea level changes, and then compare regional SSH features with relevant oceanic circulation indices. For the time period 2090-2099, relative to the control simulation and zero global mean, local extreme amplitudes of regional sea level change range from −0.53 m to +0.6 m (Fig. 3.3); maximum basin-scale changes amount to ± 0.3 m in Arctic Ocean and Southern Ocean (see Fig. 3.4b below). These values do not include the global mean sea level rise (Fig. 3.2, section 3.2.3), which must be added to obtain the full sea level signal.

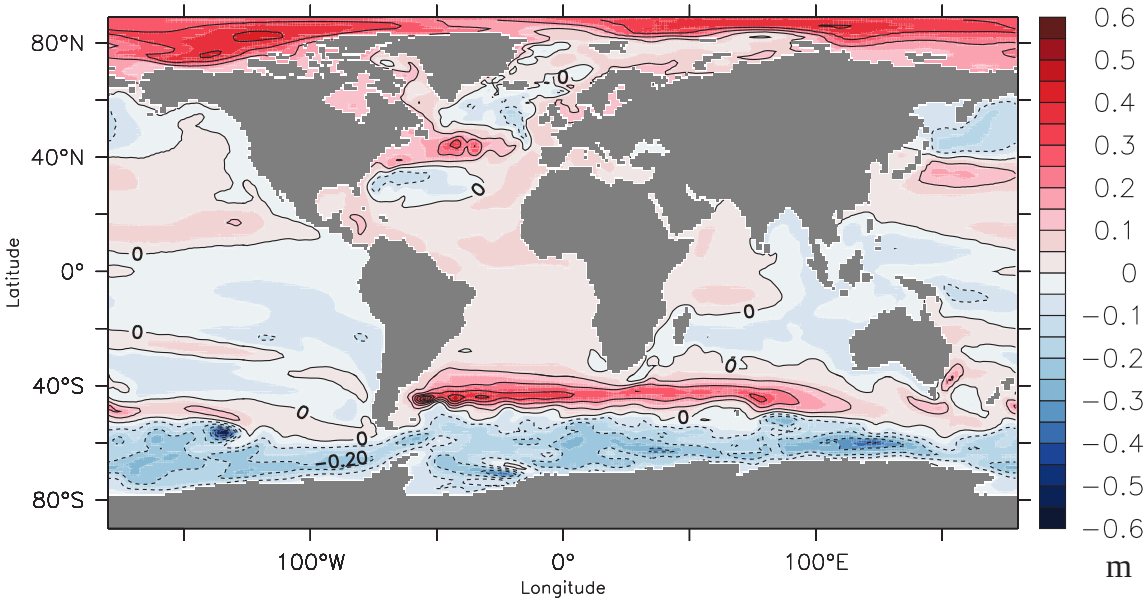

Figure 3.3: *MPI-OM sea surface height anomaly (in meters): relative difference between the mean SSH for the decade 2090-2099 and the control run mean SSH (Fig. 3.1b); contour line interval is 0.1 m. Global mean changes (Fig. 3.2) are not included, and must be added to obtain the full sea level change.*

The most prominent pattern in the North Atlantic resembles a tripole in SW-NE ori-

entation: SSH is lower by up to 0.15 m in the central subtropical area, is higher by 0.4 m along the path of the North Atlantic drift, and is lower again further north in the central part of the subpolar gyre. This pattern is consistent with a northward shift of the North Atlantic Current by some 6°, which is evident from the shift of near surface horizontal velocities (not shown). Along the eastern and western coast lines of the Atlantic basin, dynamic sea level increases everywhere between 0.05 m and 0.15 m. From 30°S to 10°N in the Atlantic, SSH changes by less than 0.05 m; these changes are nearly uniform, so that the relative SSH gradients between these latitudes are not altered (Fig. 3.3). In the Indian and Pacific Ocean, dynamic SSH generally changes by not more than 0.05 m. An exception is the Kuroshio and its extension, where a dipole pattern (Fig. 3.3) indicates an increasing SSH gradient, consistent with a stronger horizontal mass transport in this region (not shown). In contrast to the North Atlantic Current, however, the Kuroshio extension does not shift in latitude. Sea level in the Arctic Ocean increases by up to 0.4 - 0.5 m towards the end of the 21st century (Fig. 3.3). This is nearly twice the global average, and, as will be shown in section 3.4, is mainly due to freshening of the surface layers from increased precipitation and river run-off. The basin average gradient from the Arctic Ocean to the North Atlantic basin increases by 0.2 m accordingly (Fig. 3.4), and the total fresh water export from the Arctic Ocean through Fram Strait and the Canadian Arctic Archipelago rises by 50% (Haak, personal communication); across Bering Strait, the SSH drop is reduced by 0.3 m, but the direction of the gradient is maintained, and fresh water import (referenced to a salinity of S_{ref} =34.8 psu) into the Arctic Ocean through Bering Strait actually increases by 20% during the 21st century (Haak, personal communication). The meridional SSH difference across the ACC increases from a zonal average of 2.6 m to 2.8 m (+7%), which can be associated with a stronger transport of the ACC (e.g. Drake Passage transport increases by 6% from 160 Sv to 170 Sv). In the Atlantic and Indian Ocean section of the ACC, the SSH gradient increases from 2.6 m to 2.92 m (+11%) (Fig. 3.3). We relate this prominent pattern to a strengthening of the combined gyre transport of the anticyclonic South Atlantic subtropical gyre and the cyclonic Weddell Sea gyre. Both gyres contribute about equally to the anomalous transport by purely baroclinic contributions (not shown).

The temporal development of regional integrated relative SSH anomalies (Fig. 3.4) illustrates that the timescales of basin-integrated SSH adjustments are not uniform (note that the mean global sea level rise from Fig. 3.2 must be added to the curves in Fig. 3.4 to obtain the full sea level change). Basin averaged SSHs in the North and South Atlantic exhibit a pronounced multidecadal variability, with maximum rates of change near 15 mm yr^{-1}. Towards 2120, relative SSH in the Atlantic basin has risen by 60 mm in both hemispheres, so that the South to North Atlantic SSH gradient remains

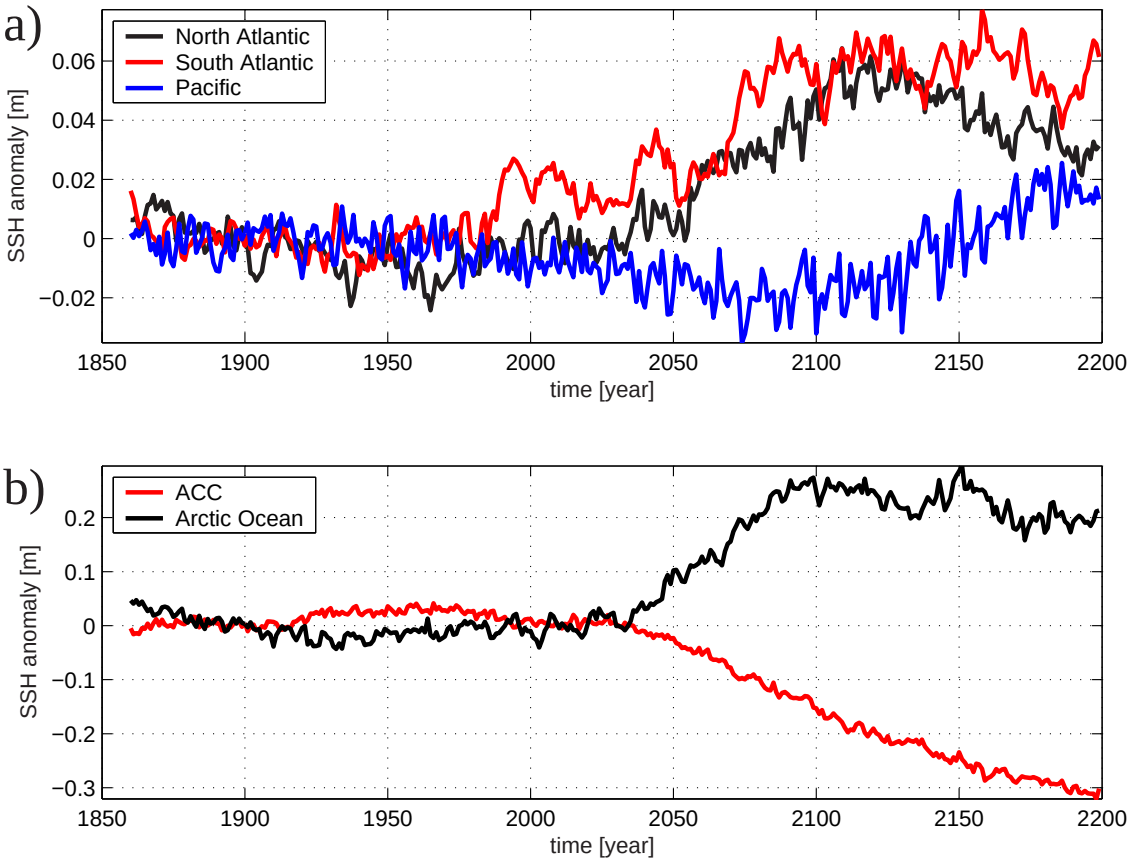

Figure 3.4: *Basin averaged evolution of SSH anomalies: deviation from the global mean change in Fig. 3.2 at corresponding times; a) North Atlantic (0°N-65°N), South Atlantic (40°S-0°S) and Pacific (30°S-65°N) SSH; b) ACC (80°S-55°S) and Arctic Ocean (75°N-90°N) SSH. Note that vertical scales in a) and b) are different.*

largely unchanged. Note, however, that the variability of North and South Atlantic basin-integrated SSH is different. Several modeling studies have empirically found a linear relationship between interhemispheric meridional steric height (or pressure) gradients and the meridional overturning circulation (Hughes and Weaver, 1994; Thorpe et al., 2001; Hu et al., 2004b). This requires a simple relation between zonal and meridional pressure gradients. In the light of an equatorially asymmetric thermohaline flow, however, the theoretical connection between zonal and meridional pressure gradients is not straight forward (Marotzke, 1997, 2000; Marotzke and Klinger, 2000). Whereas it is conceptually plausible that a change in Atlantic overturning is connected to NADW properties and thus also to the meridional density gradient, it is not so obvious how the spatially structured sea surface topography would adjust to MOC changes. It is also apparent from Fig. 3.3 that a simple 'subpolar area up - subtropical area down' pattern, similar to the North Atlantic dipole mentioned by Bryan (1996), is not applicable in the present simulation.

In the Pacific, basin averaged SSH shows a small negative trend in the 21st century, followed by a small positive trend in the 22nd century (Fig. 3.4); the relative difference between North Atlantic and Pacific Ocean SSH (section 3.2.2) thus reaches a minimum value synchronously with the minimum of the North Atlantic MOC around the year 2100 (see Fig. 3.5 below). From 2100 to 2199, this SSH difference has been almost reestablished (within 0.02 m), but without an analog recovery of the North Atlantic MOC. The strongest relative SSH changes occur in the high latitudes: basin average Arctic Ocean SSH has increased 0.25 m by 2100, while SSH in the Southern Ocean decreases uniformly through the 21st and 22nd century, not reaching equilibrium during the simulation period. Additional transient 1% CO_2 increase experiments, using a coarser resolution version of ECHAM5/MPI-OM with separated atmospheric heat fluxes and wind forcing, indicate that the prominent SSH anomaly signal along the South Atlantic-ACC front can be attributed to anomalous wind forcing, without a subsequent change of North Atlantic overturning (not shown); thus, the South Atlantic SSH signal in the present simulation has most likely no predictive skill for the North Atlantic MOC.

What are the implications of this complex SSH adjustment for the large scale circulation patterns? Since the driving mechanisms in the present scenario simulation are a complex interplay of anomalous wind forcing, fresh water and heat fluxes, we do not expect to find a simple linear relationship between sea level changes in the North Atlantic and MOC strength. This is in contrast to the analysis by Levermann et al. (2005), who applied a 0.35 Sv fresh water equivalent negative salt flux for 800 years to invoke a shut down of the North Atlantic overturning cell. In order to assess the connection between the baroclinic components of the North Atlantic subtropical and subpolar gyre circulations and SSH changes, we have calculated potential energy anomalies (PEA's) from temperature and salinity fields following the procedure of Curry and McCartney (2001). The PEA χ is defined as the vertical integral of the specific volume anomaly δ over the top 2000 dbar, multiplied by pressure p and divided by the gravitational constant g:

$$\chi = \frac{1}{g} \int_{p}^{0} p\delta dp \tag{3.2}$$

PEA (in units of J m^{-2}) is similar to dynamic height, but weighted by pg^{-1}, and approximates a stream function for the baroclinic mass transport. The choice of 2000 dbar for the lower level of integration was chosen here to be consistent with Curry and McCartney (2001). An index of the baroclinic mass transport (in units of 10^6 kg s^{-1} = 1 MT s^{-1}, which is equal to 10^6 m^3 s^{-1} = 1 Sv within a few percent) between two locations is then

obtained by the PEA difference, divided by a mean Coriolis parameter f:

$$T_m = \frac{\chi_1 - \chi_2}{f} \tag{3.3}$$

Estimates from the climatological PEA difference between Bermuda (box averaged from 63°W-68°W and 30°N-35°N) and the Labrador Sea (box averaged from 45°W-50°W and 53°N-58°N) yield an mean eastward baroclinic mass transport of 60 MT s^{-1} (Curry and McCartney, 2001) between the two centers, using f at 40°N. This compares to an average combined NA subtropical / subpolar gyre transport of 74.2 MT s^{-1} in our unperturbed control integration, with a maximal change of $\approx$ 21 MT s^{-1} between transport extremes, and pronounced multidecadal variability (Fig. 3.5a, grey line). In the scenario simulation, the mean gyre transport index is reduced to $\approx$ 68 MT s^{-1} by the year 2100 (Fig. 3.5a, black line), and the mean transport from 2100 to 2199 resides around this value. Labrador Basin and Bermuda PEA both increase considerably under the A1B scenario from the year 2000 on; based on the individual PEA gyre histories (not shown), we conclude that the transport reduction between 2060 and 2100 (Fig. 3.5a) can be mainly attributed to more rapid changes in the Labrador Basin PEA in this period. The sea surface height difference ΔSSH calculated between the same Labrador Basin and Bermuda boxes compares well with the gyre transport index in terms of interannual variability (Fig. 3.5b). However, while the gyre transport reduces over the course of 40 years, the SSH difference reduces by 0.15 m around 2070 in less than 5 years. Curiously, this SSH change is mainly caused by a 0.11 m SSH drop in the Bermuda box, and only a 0.04 m SSH change in the Labrador Basin box. We are currently unable to explain this very rapid adjustment in Bermuda SSH; note, however, that this signal is on the order of magnitude of internal variability. The variability in the North Atlantic gyre transport has been partly linked to the atmospheric North Atlantic Oscillation (NAO) index (Curry and McCartney, 2001); the NAO index in the present simulation does indeed coincide with positive and negative NA gyre transport extremes of 6-7 Sv between 1890 and 1940 (not shown), pointing to the importance of wind driven gyre transport anomalies. For the remaining simulation period, however, there is little agreement between the atmospheric and oceanic index. Most importantly, the gyre transport shift from 2060-2100 is not accompanied by a similar regime shift in the NAO index, which does not show a significant corresponding trend. Thus, we focus our analysis here on the connection between the combined baroclinic gyre transport, ΔSSH, and MOC in the North Atlantic.

The maximum of the Atlantic MOC at 30°N weakens gradually, beginning as early as in the year 2000, reaching its minimum value of 14.5 Sv (a 26% reduction) around year 2100, followed by a modest recovery to 16 Sv in the remaining 100 simulation years (Fig. 3.5c).

Significant changes in the combined gyre transport, however, set in around year 2070 (Fig. 3.5a); the weakening MOC during the years 2000 to 2070 does not appear to affect the gyre transport index during this period. Choosing a different latitude for the MOC index does not alter the picture qualitatively. Although the horizontal gyre circulation is related to the MOC due to coupling between barotropic and baroclinic modes through topography (Häkkinen, 2001), it is apparent (Fig. 3.5a and c) that the MOC and combined gyre circulation evolve differently not only in terms of interannual to decadal variability, but also in terms of large scale circulation changes that are associated with a reduction of the North Atlantic overturning rate.

We have calculated a simple lag correlation (Fig. 3.5d) between the normalized time series of gyre transport, ΔSSH and MOC. The apparent trends between 2000 and 2199 in all time series (from the scenario calculation) dominate the correlation values (thin lines in Fig. 3.5d), yielding little information on shorter timescales. The effect of this trend has been removed by subtracting 21-year running means from the original time series, and calculating correlations with the detrended time series (thick lines in Fig. 3.5d). The correlation of the gyre transport index with the dynamic SSH difference between Bermuda and Labrador at zero lag is 0.78 for the detrended, and 0.73 for the original time series, respectively (Fig. 3.5d). The high correlation between gyre transport and ΔSSH at zero lag furthermore indicates that surface velocities can be used to infer the baroclinic part of the combined gyre transport from the surface to 2000 dbar depth, and SSH changes pertain mainly to transport anomalies in this layer. MOC anomalies are not significantly correlated with either ΔSSH or the gyre transport on timescales of less than 21 years (Fig. 3.5d), effectively preventing reliable estimates of MOC strength on these timescales from ΔSSH as defined here. Perhaps, a simple, linear relationship between SSH changes and MOC reduction is masked in the present study due to the interference of a number of processes in the North Atlantic. Furthermore, the MOC as a zonally integrated quantity represents basin scale changes that need not necessarily be present in those locations that we chose for the gyre transport calculations. Analyzing TOPEX/Poseidon altimeter observations, Häkkinen (2001) and Häkkinen and Rhines (2004) reported that SSH in the North Atlantic subpolar gyre increased during the 1990s, indicating a weaker subpolar gyre circulation through the balance of SSH anomalies with geostrophic velocity anomalies. As far as a decline of the baroclinic subpolar gyre circulation originates from local air-sea buoyancy forcing, gyre transport anomalies could also point to a cessation of deep convection processes, which in turn are intimately linked to the MOC strength (Häkkinen and Rhines, 2004).

In our analysis, we have avoided smoothing of the timeseries in Fig. 3.4 and 3.5. All time series exhibit annual to decadal variability, which appears to be of internal origin.

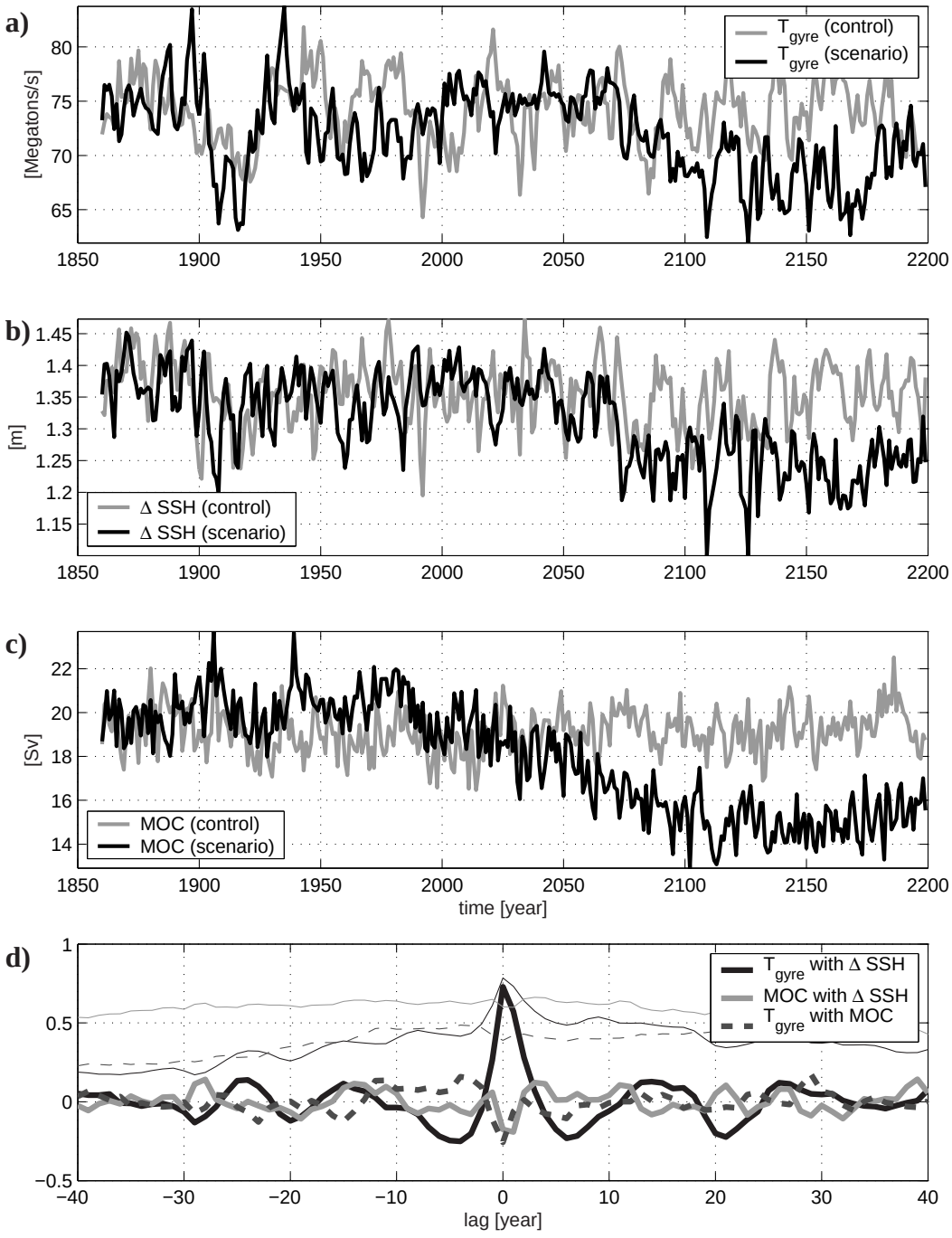

Figure 3.5: *a) NA baroclinic gyre transport index as defined in Curry and McCartney (2001); b) ΔSSH between Bermuda and Labrador Sea; c) NA MOC at 30° N; d) Lag correlation of the scenario time series (black lines in a, b, c) with each other. The thin lines in d) are calculated from the A1B scenario time series as shown above (black lines in a, b, c); the thick lines in d) are calculated from the same A1B scenario time series but with 21 year running means subtracted to remove the longer period trends.*

Sufficient smoothing would certainly bring out the GHG signal more clearly, and thus lead to higher correlation between gyre transport, ΔSSH and the MOC (Fig. 3.5d). However, our comparison of combined gyre transport, ΔSSH and MOC suggests that inferences of the MOC state in the NA from SSH anomalies are difficult, especially on timescales of less than 20 years, where internal climate variability prevents a skillful correlation between gyre transport, ΔSSH and the MOC.

3.4 Thermosteric and halosteric SSH changes

In this section, we describe the global pattern of steric sea level changes under the applied IPCC-A1B scenario. Steric sea level change is associated with vertical expansion or contraction of the water column in response to changes in the local density structure, and the total mass of the global ocean is kept constant (our simulation does not include eustatic contributions from land sources). We frame our discussion in terms of variations (with respect to time, indicated by a prime) from a mean or control state of the vertically integrated hydrostatic balance, as in Gill and Niiler (1973). The deviation of the sea surface elevation ζ' is then the sum of three terms

$$\zeta' = \zeta'_a + p'_b g^{-1} \rho_0^{-1} + \zeta'_s, \tag{3.4}$$

where ζ'_a is the barometric correction to sea level, $p'_b g^{-1} \rho_0^{-1}$ is the contribution from bottom pressure changes, and ζ'_s is defined as the steric level deviation

$$\zeta'_s = -\int_{-H}^{0} \frac{\rho'}{\rho_0} dz, \tag{3.5}$$

where ρ_0 is usually referenced to a temperature of 0°C and a salinity of 35 psu. In the present analysis, $\zeta'_a = 0$. Equation 3.4 implies that the dynamic sea surface height and steric height (or, analogous, their horizontal gradients) are only equivalent if bottom pressure changes are zero. Otherwise, the flow field calculated through the geostrophic relation is not physically acceptable, as it fails to conserve mass in the presence of a non-zero vertically averaged background flow (Wunsch and Stammer, 1998). From the difference between the dynamic (ζ': prognostically calculated as described in section 3.2) and steric (ζ'_s: from equation 3.5) sea level fields we obtain the bottom pressure changes for the period 2090-2099 relative to the control run mean (Fig. 3.6). As the model does not include eustatic sources, all bottom pressure changes occur solely due to mass redistribution within the global ocean. Most prominently, all shelf regions (less than ≈500

m depth) experience an additional mass loading of up to 0.45 m (Fig. 3.6). The very shallow water columns only permit a purely steric expansion much smaller than that of deepwater columns. The resulting strong steric SSH gradients across shelfs cannot be balanced by geostrophy; instead, mass redistribution ($p_b' g^{-1} \rho_0^{-1}$ term in equation 3.4) onto the shelfs occurs, effectively reducing the total gradient in sea level across the shelfs. Another salient feature is the pronounced negative bottom pressure anomaly of up to 0.2 m in the Atlantic section of the Southern Ocean, which we relate to the intensified gyre circulation as described in section 3.3.

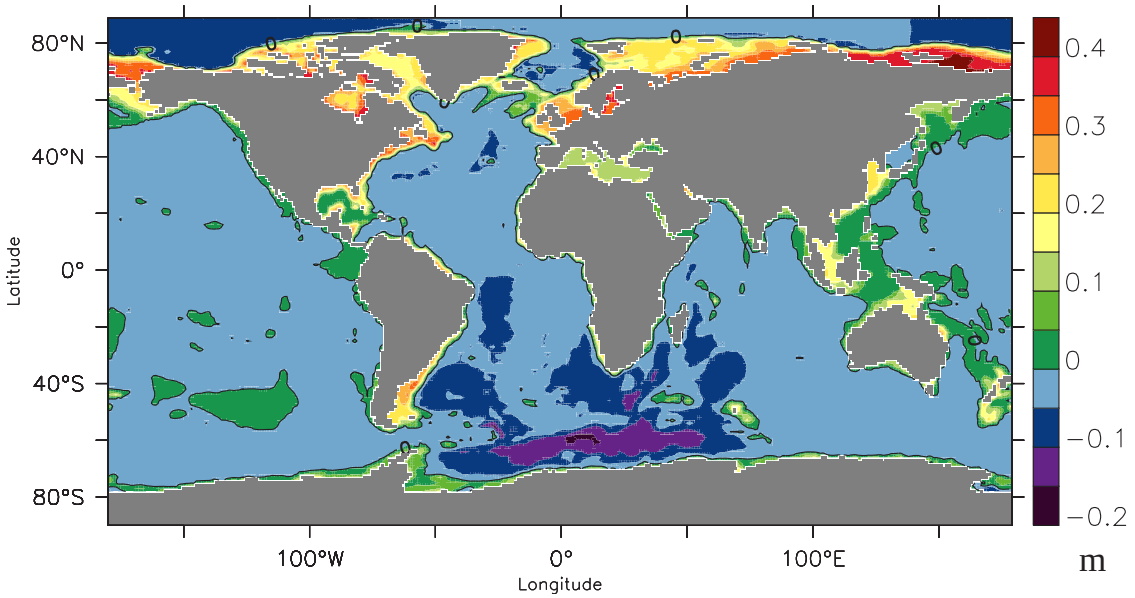

Figure 3.6: *Mean bottom pressure changes $p_b' g^{-1} \rho_0^{-1}$ (in meters water column equivalent) for the decade 2090-2099 relative to the control simulation, as defined in equation 3.4.*

From equation 3.4, we evaluate the individual contribution of temperature and salinity to the steric anomalies in reference to the temperature and salinity fields of the unperturbed control integration. These thermosteric (ζ_s^{thermo}) and halosteric (ζ_s^{halo}) sea level changes are then calculated from

$$\zeta_s^{\text{thermo}} = \int_{-H}^{0} \frac{\rho(S_C, T_C, p) - \rho(S_C, T_{EX}, p)}{\rho(S_C, T_C, p)} dz \tag{3.6}$$

$$\zeta_s^{\text{halo}} = \int_{-H}^{0} \frac{\rho(S_C, T_C, p) - \rho(S_{EX}, T_C, p)}{\rho(S_C, T_C, p)} dz \tag{3.7}$$

where the subscripts EX and C refer to the scenario experiments and control run fields, respectively, and the in situ density ρ is a time dependent, non-linear function of salin-

ity, temperature and pressure (Gill, 1982). Combining the two different temperature and salinity fields from control and scenario experiments potentially introduces an error in the density calculation through non-linearity in the equation of state. However, we have computed the difference between the full steric height field and the sum of the two individual fields, and found that the deviation is at least two orders of magnitude smaller than the actual steric signals (not shown).

For the period 2090-2099, the mean thermosteric sea level change is positive for most regions in all oceans (Fig. 3.7a). In the southern hemisphere, a few isolated patches in the Pacific and Southern Ocean have a negative thermosteric anomaly; in the northern hemisphere, two small negative anomalies are located in the North Atlantic subpolar gyre and north of the Kuroshio. The eastern part of the subpolar NA gyre responds with a minimum thermosteric sea level rise. Thermosteric sea level change in the North Atlantic basin and along the South Atlantic edge of the ACC is largely above 0.55 m, which is significantly stronger than in the Pacific at comparable latitudes, where values mostly do not exceed 0.25 m. Such differing responses reflect the formation of deep water and enhanced ventilation, by which the warming signal can penetrate to the deeper layers in those regions, and then be advected horizontally.

Considerable redistribution of salt within and between ocean basins has been observed over annual to decadal periods (Levitus, 1990), leading to significant halosteric anomalies on regional scales Antonov et al. (2002). Here, we will focus our analysis on transient local salinity changes and the implied halosteric signal under the A1B scenario. As expected, the sign of the halosteric sea level signal is alternating between the different ocean basins (Fig. 3.7b). We find the most pronounced signals in the subtropical North Atlantic and in the Arctic Ocean, which exhibit a similar absolute halosteric sea level change of 0.5 m, but with negative and positive signs, respectively (Figs. 3.7b and c). The Pacific basin shows a small net increase (with local maxima around 0.1 m) reflecting increased fresh water import from the Atlantic basin (Latif et al., 2000), and in the Antarctic Ocean the halosteric change is slightly negative (with minima around -0.15 m). What are the origins of the simulated halosteric expansion and contraction? Regional salinity changes are a consequence of changes in the local fresh water balance, e.g. induced by changes in the hydrological cycle (precipitation, evaporation and river run-off: $P-E+R$), anomalous salt advection in the ocean or altered sea ice volume. Increased atmospheric moisture transport from lower to high latitudes is a common feature of many climate scenario simulations (Bryan, 1996; Mikolajewicz and Voss, 2000; Thorpe et al., 2001), and can account for the large negative salinity anomaly in the Atlantic subtropical region and the positive salinity anomaly in the Arctic Ocean. For the Arctic Ocean, an additional positive halosteric source is melting sea ice. Compared to the 20th century, some additional 7.8×10^4 km^3

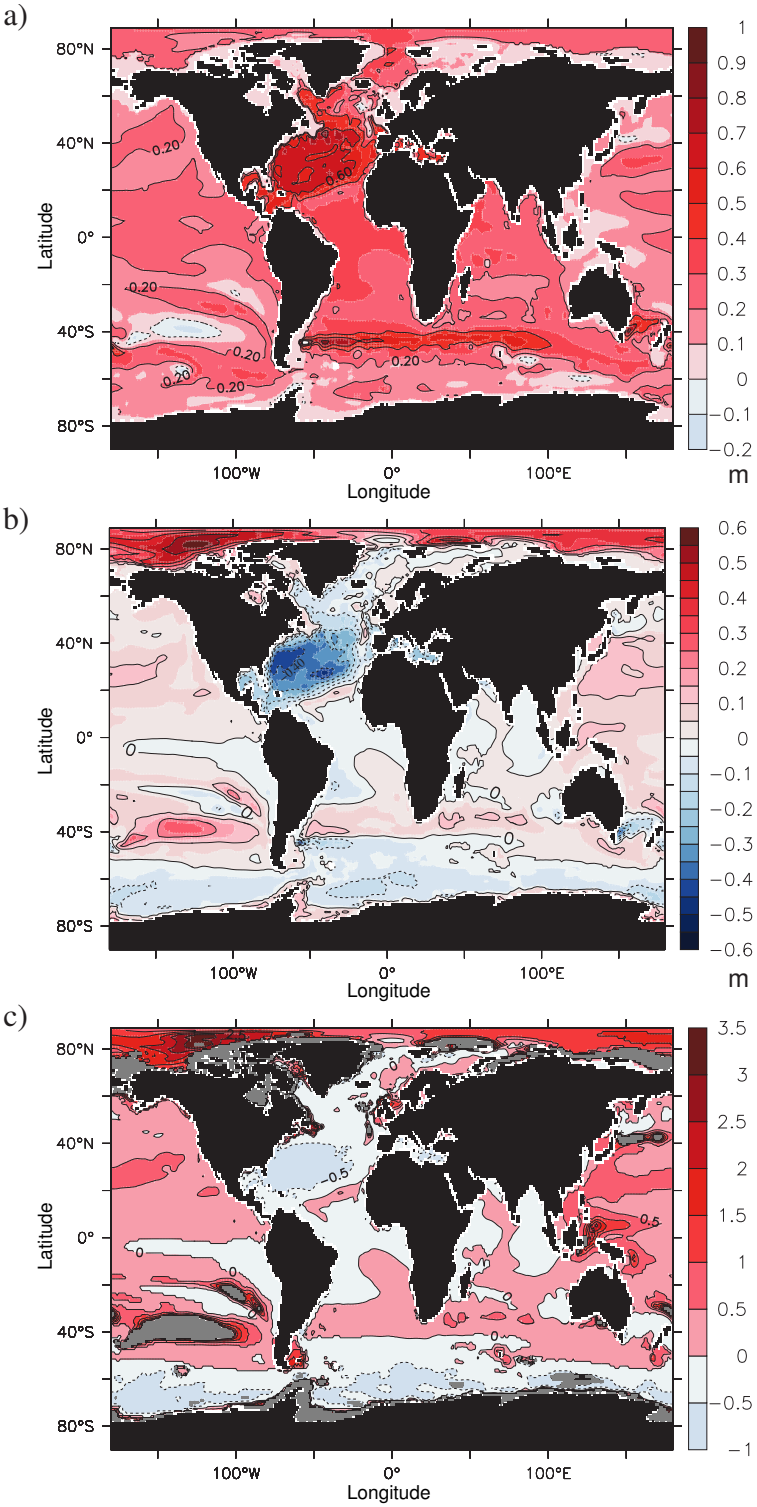

Figure 3.7: *Steric sea level difference for the period 2090-2099 relative to the control run, as defined in equation 3.6. (a) Thermosteric (ζ_s^{thermo}) contribution; (b) halosteric (ζ_s^{halo}) contribution; (c) ratio $\zeta_s^{halo}/\zeta_s^{thermo}$, with values above 3.5 and below -1 in grey.*

freshwater have been put into the Arctic Ocean through $P - E + R$ changes by the end of the 21st century, while melting sea ice contributes about 1.8×10^4 km^3 of anomalous freshwater. If we assume, for the sake of argument, that these freshwater anomalies simply replace existing Arctic waters, a maximum of 20% of the halosteric anomaly in the Arctic Ocean by 2090-2099 can be attributed to disappearing sea ice. Curry and Mauritzen (2005) found a freshening of the Nordic Seas and subpolar basins in the Atlantic between 1965 and 1995 in the upper 1000 m. This would imply a positive halosteric signal. In our A1B simulation, the halosteric signal in this region changes sign from positive (fresher) to negative (saltier) around 2040, indicating that a net negative fresh water balance prior to 2040 is then converted in sign and dominated by salt advection from the subtropical NA. Thorpe et al. (2001) suggested that this mechanism might also function as a stabilizing feedback for the MOC in the Atlantic.

Finally, we consider the vertical structure of the steric signals. Starting at the sea surface, the thermosteric and halosteric contributions from each level are cumulatively summed up to a depth of 3000 m for different ocean subdomains for the period 2090-2099 (Fig. 3.8). Generally, the thermosteric signal is larger than any halosteric change, with the exception of the Arctic Ocean. There, the freshening of the 0-250 m layer contributes about 55% to the total steric sea level change, whereas the deeper layers from 250-1500 m mainly add to the thermosteric signal (Fig. 3.8e). This subsurface warming of the Arctic Ocean under increasing GHG forcing is due to increased northward heat transport north of ≈60°N, similar to the anomalous advection mechanism described by Hu et al. (2004a). In spite of the reduced MOC, subtropical and subpolar Atlantic water masses still modulate the deeper Arctic Ocean layers significantly in our simulation. This is in contrast to an earlier study of (Bryan, 1996), who found that the reduction of the overturning in the Atlantic would isolate the Arctic Ocean from the warmer and saltier subtropical Atlantic water masses. In the Atlantic, halosteric and thermosteric changes tend to compensate each other, but the thermosteric signal is 1.5 to 3 times stronger than any halosteric change (Fig. 3.8a and b). Due to deep water formation, the thermosteric expansion in the subpolar North Atlantic is very homogeneous up to the depth of NADW (≈2000 m), whereas the thermosteric signal in the subtropical North Atlantic has its largest contribution within the upper 1000 m. The Pacific response is much smaller in amplitude, and the steric changes are largely confined to the upper 500-700 m (Fig. 3.8c and d). In the Southern Ocean, thermo- and halosteric changes occur over the entire depth range of 0-3000 m (Fig. 3.8f). This demonstrates the intense vertical transfer in the ACC, by which the water properties are changed throughout the water column. Notice the reversal of the halosteric change at a depth of 200 m from positive (fresher) to negative (saltier) in the Southern Ocean. The response in the upper layers is likely linked

to the increased atmospheric moisture transport from low to high latitudes (similar to the change in the Arctic Ocean fresh water balance), whereas the deeper layer changes are most likely influenced by saltier upwelling NADW (compare to Fig. 3.8a). Qualitatively, the differences in the vertical extent of thermosteric changes between ocean basins agree well with recent observations from Barnett et al. (2005), who find that the vertical structure of a warming signal, penetrating the oceans since 1960, varies widely by ocean.

Our results show that salinity anomalies have a significant influence on regional steric sea level changes. Among others, Antonov et al. (2002) have pointed out that estimates of heat content or temperature changes from altimetry can be seriously biased for certain regions, when halosteric effects are not considered. It will become increasingly more important to take salinity changes into account beyond their natural variability in the evaluation of regional and global sea level change. One may also view this as a problem of hydrographic versus altimetric measuring systems.

3.5 Conclusions

Based on our analysis of dynamic and steric sea surface height (SSH) changes in the IPCC A1B scenario as simulated with ECHAM5/MPI-OM, we conclude the following:

1. We confirm previous results that global sea level change is not an accurate measure of regional sea level change in simulated climate change scenarios, because regional sea level anomalies are of a similar order of magnitude (Fig. 3.2 and 3.4). Possible eustatic sources for sea level change are not considered in this study.

2. We also confirm previous results that basin integrated SSH adjustments yield the strongest increase in the Arctic Ocean due to enhanced freshwater input from precipitation and river run-off; SSH changes are minimal in the Southern Ocean due to increased wind stress, which leads to a stronger ACC transport and a subsequent dynamic SSH adjustment.

3. The basin integrated SSH difference of 0.78 m between the North Atlantic and Pacific Ocean is reduced by 0.06 m by the year 2100, coinciding with a minimum North Atlantic overturning, but is reestablished within 100 years through a Pacific Ocean SSH rise and a North Atlantic SSH drop, without an analog recovery of the North Atlantic overturning.

4. The sea surface height difference between Bermuda and the Labrador Sea correlates highly at zero lag with the combined North Atlantic gyre transport on interannual to decadal timescales. Overturning changes in the North Atlantic, on the other hand,

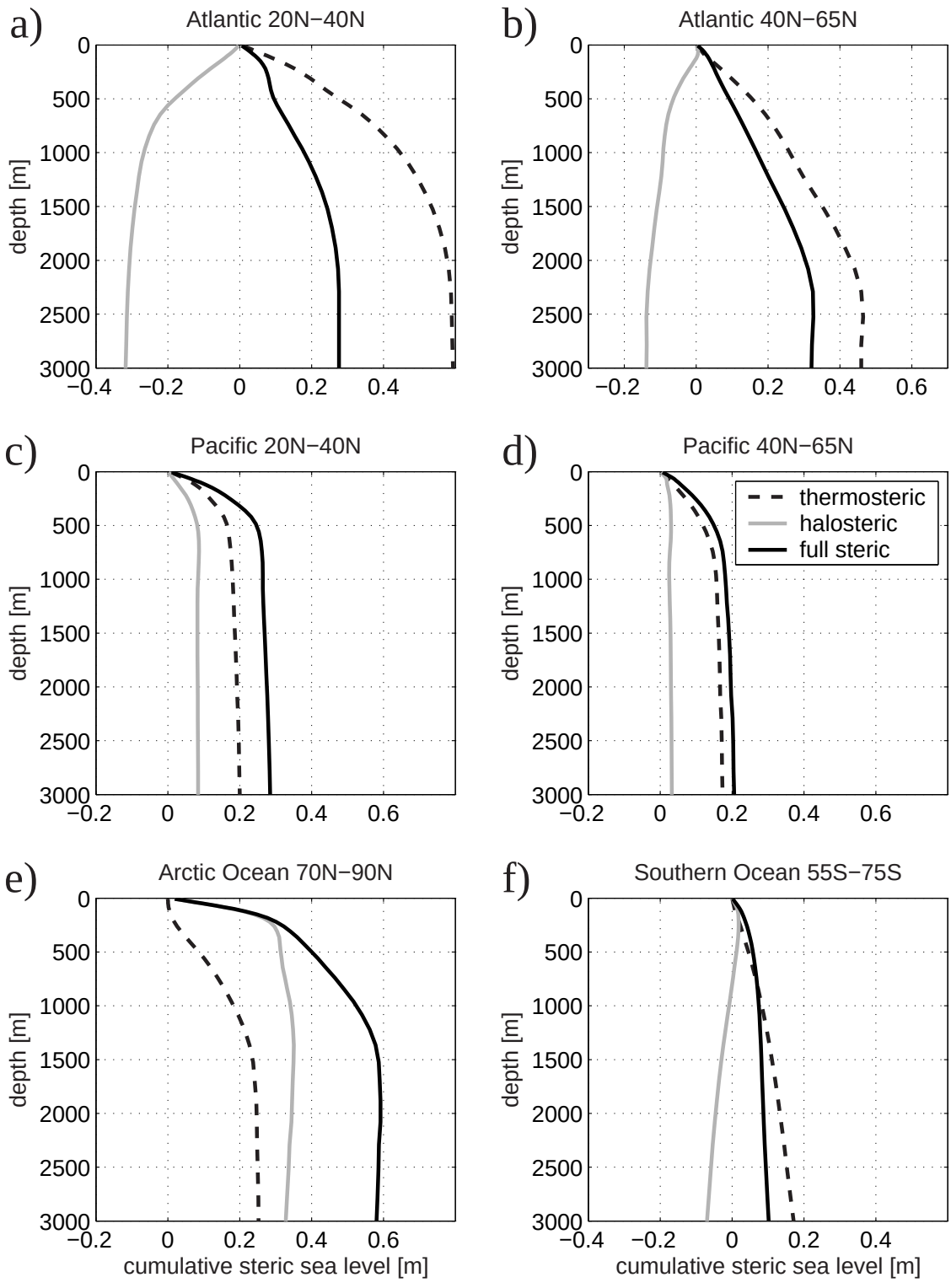

Figure 3.8: *Cumulative sum of thermosteric (dashed line), halosteric (grey line) and total steric (black line) anomalies for different ocean areas. Starting at the surface, the steric anomaly from each depth layer is added up. Note that the abscissa has the same width in all plots.*

evolve on different timescales, and cannot be reliably inferred from SSH gradient and gyre transport changes.

5. Mass redistribution within the global ocean by 2090-2099 causes bottom pressure increases of up to 0.45 m across shallow shelf areas; the Atlantic section of the ACC responds with a negative bottom pressure anomaly of up to -0.2 m due to the intensified gyre circulation. It remains to be analyzed how these large-scale mass redistributions would affect the geoid, for example changes of the earth's dynamic oblateness (J_2) and regional isostatic adjustment.

6. Thermosteric sea level change by 2100 is positive in almost all ocean regions, but varies considerably by region. Halosteric effects in the North Atlantic subtropical region partly compensate thermosteric sea level rise. In contrast, freshening in the Arctic Ocean leads to an additional halosteric sea level rise. Steric anomalies in the Pacific Ocean are positive, but of smaller magnitude.

7. The vertical distribution of thermosteric and halosteric anomalies that contribute to sea level change is very different between ocean basins. In the North Atlantic, the steric anomalies reach to depths of the North Atlantic Deep Water (2000 m), whereas steric anomalies in the entire Pacific Ocean occur mainly in the upper 500 m. In the Southern Ocean, steric anomalies occur throughout the entire water column, reflecting the strong vertical exchange of buoyancy in this region.

Acknowledgement Johanna Baehr provided valuable comments on the manuscript. We wish to thank Uwe Mikolajewicz and Detlef Stammer for stimulating discussions. We also thank two anonymous reviewers for their very constructive comments and suggestions. This work was supported by the Max Planck Society and the International Max Planck Research School on Earth System Modelling. The computer simulations were performed at the DKRZ (Deutsches Klimarechenzentrum) in Hamburg, Germany.

4 Ocean Bottom Pressure Changes Lead to a Decreasing Length-of-Day in a Warming Climate

Abstract

We use a coupled climate model to evaluate ocean bottom pressure changes in the IPCC-A1B climate scenario. Ocean warming in the 21st and 22nd centuries causes secular oceanic bottom pressure anomalies. The essential feature is a net mass transfer onto shallow shelf areas from the deeper ocean areas, which exhibit negative bottom pressure anomalies. We develop a simple mass redistribution model that explains this mechanism. Regionally, however, distinct patterns of bottom pressure anomalies emerge due to spatially inhomogeneous warming and ocean circulation changes. Most prominently, the Arctic Ocean shelves experience an above-average bottom pressure increase. We find a net transfer of mass from the southern to the northern hemisphere, and a net movement of mass closer towards Earth's axis of rotation. Thus, ocean warming and the ensuing mass redistribution change the length-of-day by -0.12 ms within 200 years, demonstrating that the oceans are capable of exciting nontidal length-of-day changes on decadal and longer timescales.

4.1 Introduction

Sea level changes can be attributed to changes of the total ocean mass (e.g. through the input of land water from glaciers), and to changes of the ocean density at constant ocean mass (steric changes). Steric changes occur through heating or cooling of the ocean; in a warming climate, the oceans take up most of the additional heat and hence thermosteric (temperature related) sea level rises significantly (Gregory et al., 2001). Steric changes do not alter the total global ocean mass, and are thus usually not associated with ocean bottom pressure (OBP) changes. However, heat uptake by the ocean varies locally, so a certain adjustment and redistribution of the mass of water can be expected. Specifically, it is interesting to consider how a thermosteric anomaly in the deep ocean transfers onto shallower shelf regions. Ponte et al. (2002) already pointed to a shift of mass from deep to shallow ocean areas in their study, but they did not analyze the pattern or processes in detail.

Changes in ocean bottom pressure that are caused by ocean warming and circulation changes have not received much attention. The objective of our study is twofold: (1) We develop a simple conceptual model that relates ocean warming to secular bottom pressure changes, and we compare the simple model to the bottom pressure changes simulated in a coupled climate model; (2) We estimate the length-of-day changes (ΔLOD) associated with the change of Earth's moment of inertia through the simulated bottom pressure changes at constant global ocean mass.

4.2 Model and Methods

We use the coupled Atmosphere-Ocean General Circulation-Model ECHAM5/MPI-OM from the Max Planck Institute of Meteorology in the setup that was used for the Intergovernmental Panel on Climate Change (IPCC) 4th assessment report. The general model behavior is discussed in detail by Jungclaus et al. (2006). The horizontal resolution of the ocean/sea ice component MPI-OM varies between 12 km near Greenland and 180 km in the tropical Pacific; MPI-OM consists of 40 fixed vertical levels, 20 of which are distributed over the upper 700 m (Marsland et al., 2003). MPI-OM is coupled to the ECHAM5 atmosphere model at T63 horizontal resolution (corresponding to roughly 1.9°) with 31 vertical levels (Roeckner et al., 2003); no flux adjustments between the ocean and atmosphere model components are applied. Following the IPCC-A1B emission scenario (IPCC, 2001), the atmospheric CO_2 concentration rises from 367 ppmv in the year 2000 to 703 ppmv by the year 2100; in the 22nd century, the atmospheric CO_2 concentration is held constant at 703 ppmv. Relative to preindustrial conditions, global mean thermosteric

sea level rises 0.26 m by the year 2100, and 0.56 m by the year 2199 under the prescribed forcing (Landerer et al., 2007b).

In our calculation of bottom pressure we follow Ponte (1999). Bottom pressure is approximated by integrating the hydrostatic relation from the bottom $-H$ to the sea surface η, plus a spatially averaged barometric contribution $\bar{p_a}$, giving

$$p_b = g\rho_0\eta + g\int_{-H}^{0} \rho\, dz + \bar{p_a}, \tag{4.1}$$

where ρ_0 is a reference density for ocean water (here $\rho_0 = 1028kg/m^3$), g is the gravitational acceleration on Earth's surface. Rearranging terms, the bottom pressure anomaly in time (indicated by a prime) with respect to a mean or unperturbed state is given by

$$\frac{p'_b}{g\rho_0} = \eta' - \eta'_s + \frac{\bar{p'_a}}{g\rho_0}, \tag{4.2}$$

where η' is the anomalous sea surface height (SSH), and $\eta'_s = g\int_{-H}^{0} \rho'\, dz$ is the anomalous steric height. Note that the steric height deviation also includes local steric changes due to salinity anomalies, which can regionally be similar in magnitude to thermosteric signals, but often with opposite sign (Landerer et al., 2007c). At periods longer than a few days, the ocean predominantly responds to atmospheric pressure anomalies isostatically like an inverted barometer (IB), so that p_a variations have no influence on the ocean dynamics (Wunsch and Stammer, 1997). Consequently, the sea surface height term η in MPI-OM does not contain the IB effect. For present purposes, we set the mean atmospheric anomaly $\bar{p'_a}$ in equation 4.2 to zero, because we are interested in the pure oceanic signal. However, $\bar{p'_a}$ can vary in time and would have to be taken into account if one was interested in the atmospheric loading effect on ocean bottom pressure (de Viron et al., 2002; Ponte, 1999).

Furthermore, the formulation of the continuity equation in MPI-OM implies volume conservation rather than mass conservation. To ensure ocean mass conservation, we apply a time-varying but spatially uniform correction to the SSH to account for global mean sea level changes from global mean density changes (Greatbatch, 1994; Ponte, 1999). In what follows, all anomalies are annual means and are taken relative to an unperturbed control climate (CO_2 concentration of 280 ppmv). We refer to bottom pressure changes in their normalized form ($p'_b/(g\rho_0)$, equation 4.2), so that units are meters (of equivalent water column height).

4.3 Simple Redistribution Model

Before we analyze the spatial pattern of bottom pressure changes in the IPCC-A1B scenario, we develop a simple conceptual model that explains to first order how a deep ocean warming can change bottom pressures at depths below and above the steric anomaly (Figure 4.1). In this approach, we assume that density changes occur uniformly in a certain depth layer, i.e. the density (and thus steric) anomalies are a function of depth only. The total ocean mass does not vary in time. To derive the model, it is sufficient to consider one layer at depth z_i with a height h_i and areal extent A_i, in an ocean with just three layers. Warming of this layer causes a negative density anomaly ρ_i' (Figure 4.1a), corresponding to a positive specific volume anomaly $\delta_i = \rho_i'/\rho_0$. Thus, the specific volume anomaly δ_i

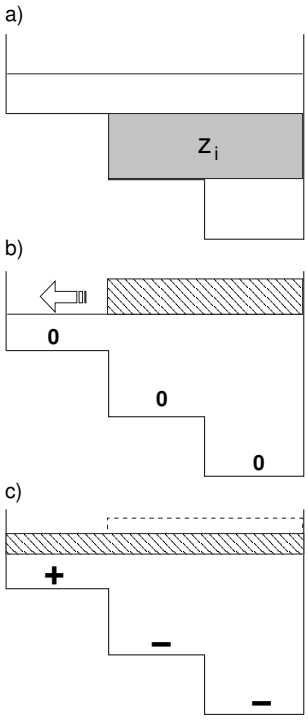

Figure 4.1: *Simple redistribution model. a) The shaded layer z_i is subject to a density anomaly ρ_i'. b) The steric anomaly from layer z_i raises the sea surface locally. c) The steric anomaly from layer z_i is spread over the entire ocean surface, leading to positive and negative bottom pressure changes as indicated (the steric anomaly is greatly exaggerated).*

would raise the sea surface throughout the horizontal extent of layer i by $\delta_i h_i$, and lead to a sharp SSH gradient where the bathymetry becomes shallower (Figure 4.1b). With no forces present to balance this SSH gradient, we can assume that fast barotropic gravity waves immediately distribute the steric anomaly from layer z_i evenly across the entire ocean surface area A_s (Figure 4.1c). At this point, the deep warming and concurrent ther-

mal expansion has led to a uniform global sea level rise, but mass redistribution within the basin has led to non-uniform bottom pressure changes. The gain in bottom pressure for the upper shallow layer is $\delta_i h_i (A_i/A_s)$, while the loss in bottom pressure for the layer z_i and each layer below is $\delta_i h_i [1 - (A_i/A_s)]$. Since mass is conserved, the sum of all bottom pressure changes is zero (e.g in Figure 4.1, substitute $A_i/A_s = 2/3$, and sum up for all three layers). Generalizing this mechanism to n layers, and allowing for steric anomalies in all layers, we derive a discrete formulation for horizontally uniform, but vertically varying bottom pressure changes:

$$\frac{\Delta p_b(z_i)}{g\rho_0} = \sum_{i+1}^{n} \eta_s'(i) - \sum_{1}^{i} (\frac{A_s}{A_i} - 1)\eta_s'(i), \tag{4.3}$$

where $i = 1, ..., n$ counts downward from the surface, and $\eta_s'(i) = (A_i/A_s)\delta_i h_i$ represents the steric sea level change contribution from layer i. Equation 4.3 states that a layer gains mass from the expansion of all layers below, and loses mass from its own expansion and expansion of all layers above. Equivalently, this statement also holds for negative expansion (contraction, or cooling), exchanging gains with losses and vice versa. Note, however, that steric expansion through warming is a very slow process compared to barotropic adjustment timescales in the real ocean. Therefore, the redistribution would always be immediate, and a SSH gradient as described in Figure 4.1b would not build up.

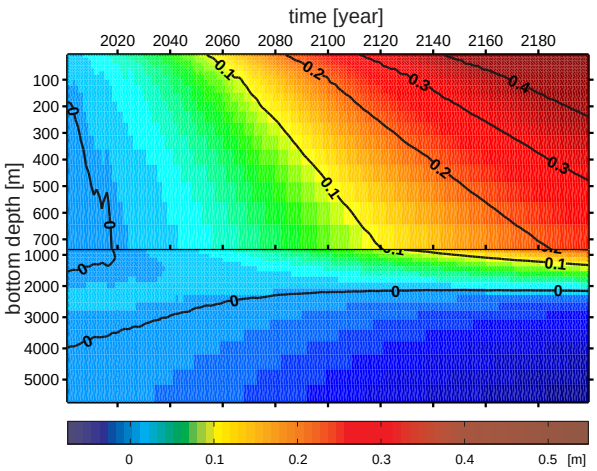

Figure 4.2: *Bottom pressure changes with depth over time in the IPCC-A1B scenario as calculated from the simple redistribution model (Equation 4.3). Pressure is expressed in terms of equivalent water column height. Note split depth axis.*

In order to estimate the magnitude of bottom pressure anomalies from ocean warming as a function of depth and time in an ocean with realistic topography, we use equation 4.3 and apply it to the horizontally averaged steric changes in our IPCC-A1B scenario for

each model layer (Figure 4.2). As the warming penetrates deeper into the ocean over time, positive bottom pressure anomalies develop above the warming, with highest amplitudes at the shallowest depths. The positive anomaly around 2500 m depth for the years 2001 to 2020 is due to a relative cooling (and thus negative steric anomaly) between 200 m and 1500 m depth, and might be linked to aerosol induced cooling carried over from the 20th century. After the year 2020, positive bottom pressure anomalies do not reach deeper than 2200 m, which approximately corresponds to the maximum depth where steric anomalies occur (with the exception of the Southern Ocean).

4.4 Spatial Pattern of p_b Anomalies

Using equation 4.2, we have calculated the spatial pattern of bottom pressure anomalies for the time mean of the years 2090-2099 (Figure 4.3a). In many areas, bottom pressure anomalies correlate well with the ocean floor topography. While the deeper ocean areas show negative bottom pressure anomalies, larger positive anomalies up to 0.4 m appear in marginal seas and across shallow shelf areas. To examine how the simulated bottom pressure anomalies deviate locally from the simple redistribution model, we subtract the horizontally averaged $p_b(z_i)$ profile (time mean from 2090-2099 in Figure 4.2) from each simulated p_b anomaly in Figure 4.3a for corresponding bottom depths. This map reveals that regional bottom pressure anomalies can deviate by a similar order of magnitude from the global mean (Figure 4.3b). Especially the North Atlantic and Arctic Ocean shelves stand out: bottom pressure there increases substantially more than, for example, in the shelf areas of the Indonesian archipelago, where Δp_b is less than the global average. In the Indonesian archipelago, projected dynamic sea level changes are negative, consistent with the pattern of atmospheric circulation changes in the equatorial Pacific region (Müller and Roeckner, 2007).

On a basin wide scale, the Atlantic and Pacific Oceans behave differently. Deep bottom pressure changes in the Atlantic have a larger amplitude than in the Pacific, which, together with the larger positive shelf signals in the Atlantic, is consistent with deeper reaching steric signals in the Atlantic Ocean as described in Landerer et al. (2007c). The pronounced negative anomaly in the Atlantic section of the Antarctic Circumpolar Current (ACC) can be associated with a spin up of the circulation through increased wind stress in the IPCC-A1B scenario (Landerer et al., 2007c). By construction, the simple redistribution model cannot capture bottom pressure changes caused by circulation changes.

A scatter plot of bottom pressure anomalies versus depth resolves basin wide and even regional variations (Figure 4.3c). For example, Baffin Bay and Labrador Sea bottom pressure changes (purple markers in Figure 4.3c) split into two branches below 650 m

depth, which corresponds to the sill depth of Davis Straight. The deeper waters in Baffin Bay are isolated from the deep reaching steric anomaly signal that penetrates the central Labrador Sea through convection. In agreement with the horizontally averaged picture elucidated above (Figure 4.1), water would flow into Baffin Bay, increasing mass and hence bottom pressure there. A similar mechanism can explain the positive bottom pressure changes in the deep Gulf of Mexico and the Mediterranean.

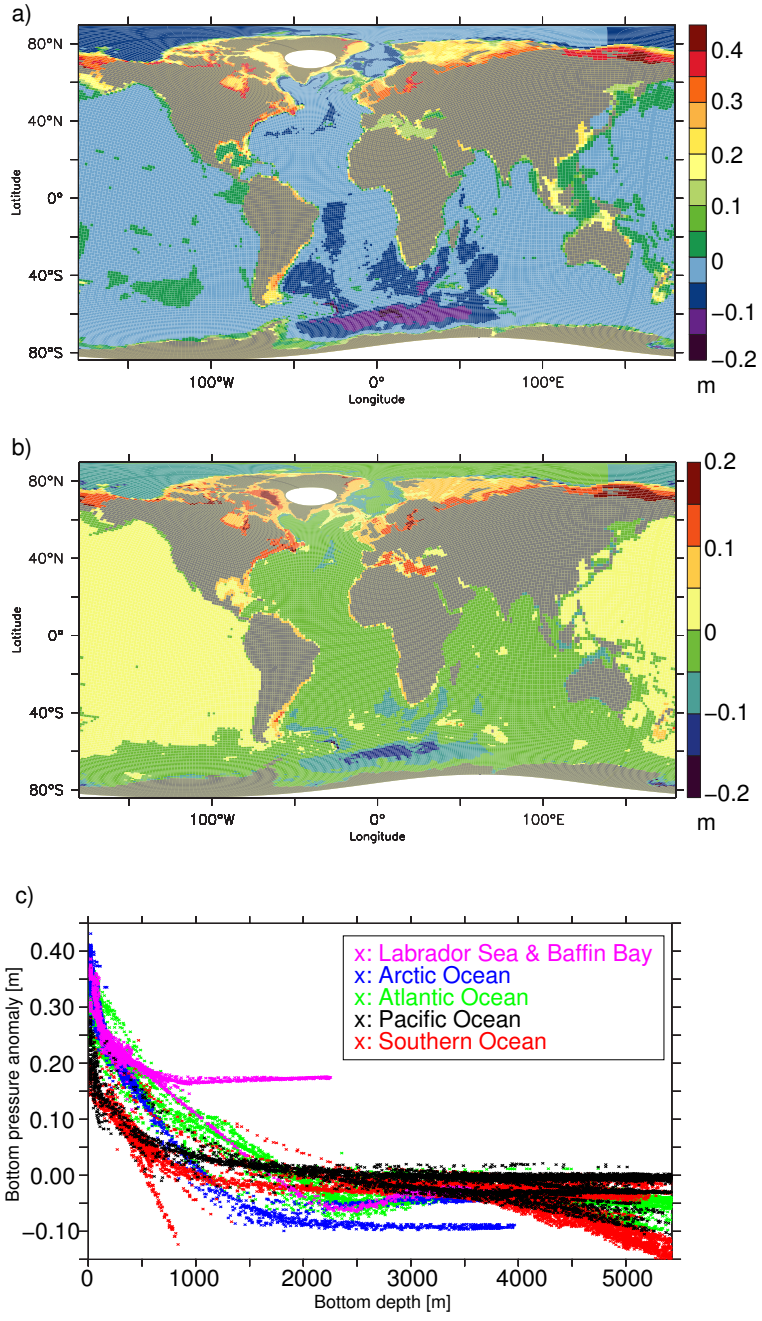

Figure 4.3: *Bottom pressure anomalies for the years 2090-2099 (time mean): a) Simulated bottom pressure changes; b) Regional deviations: simulated anomalies minus 'simple redistribution' anomalies from Figure 4.2; c) Simulated bottom pressure anomalies (from panel a) versus topographic depth, color coded for different basins/regions. Pressure is expressed in terms of equivalent water column height.*

4.5 ΔLOD from p_b Anomalies

Bottom pressure anomalies are directly proportional to mass load anomalies, thus affecting Earth's gravity field and its moment of inertia (Chao, 1994; Wahr et al., 1998). Since the angular momentum (AM) of the total Earth system is conserved, Earth's rotation rate changes if its moment of inertia is altered via a redistribution of mass in the oceans. Note, however, that the atmosphere significantly influences the total AM budget under global warming on decadal and longer time scales (de Viron et al., 2002).

Following Barnes et al. (1983), we estimate the Earth rotational excitation χ_3^{mass} related to changes about Earth's polar axis from

$$\chi_3^{mass} = \frac{0.70 R_e^4}{I_{zz} g} \iint \Delta p_b(\theta, \lambda) \cos^3\theta \, d\theta \, d\lambda \tag{4.4}$$

where R_e is the Earth's mean radius, I_{zz} is the principal moment of inertia, g is the gravitational acceleration, Δp_b are the bottom pressure anomalies described in sections 3 and 4, and θ and λ are latitude and longitude, respectively. The analysis reveals a clear secular trend in χ_3^{mass} (Figure 4.4), which corresponds to a length-of-day anomaly (ΔLOD) of nearly -0.12 ms by the year 2199 (for comparison, the motion term from ocean currents in the present simulation corresponds to ΔLOD $\approx$ 0.026 ms by 2199). The zonally integrated bottom pressure anomalies indicate a net transfer of mass from

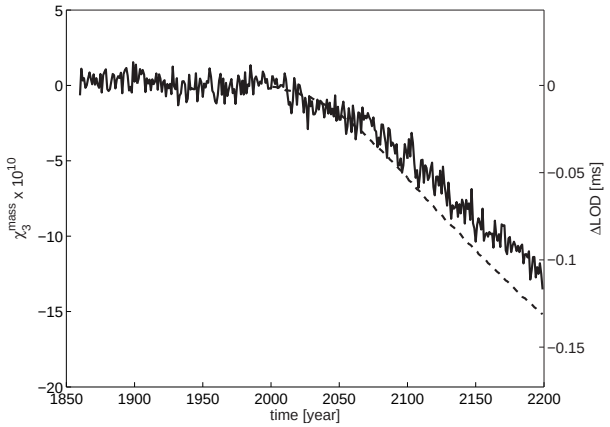

Figure 4.4: *Oceanic Earth rotational excitation (left axis) and corresponding length-of-day changes (right axis) from the simulated pattern of bottom pressure anomalies (solid line), and from the simple redistribution model (dashed line).*

the southern to the northern hemisphere (not shown). However, this mass transfer is not completely antisymmetric between the hemispheres, thus giving rise to a residual χ_3^{mass} anomaly. Essentially, mass is moved closer to the axis of rotation by means of

redistribution within the ocean. To obtain a simple approximation to the χ_3^{mass} anomaly, we have re-calculated χ_3^{mass} with the horizontally averaged bottom pressure anomalies from the simple redistribution model (Figure 4.2), inserted into equation 4.4. Although the previous section showed that regional bottom pressure anomalies can deviate substantially from the horizontally averaged profile (Figure 4.3b), the simple redistribution model does capture a substantial part of the actual χ_3^{mass} signal (Figure 4.4, dashed line), but generally overestimates the amplitude by about 20%.

4.6 Concluding Discussion

We have shown that ocean warming and circulation changes lead to significant secular bottom pressure changes in a warming climate. While the steric expansion does not change the total global ocean mass, mass is redistributed within and between ocean basins. An essential feature of our simulation is the strong positive bottom pressure anomaly on almost all shelf areas, while deep ocean regions show negative bottom pressure anomalies. Part of this mass redistribution can be explained by a simple redistribution model, which describes the bottom pressure anomalies as they should occur due to the decreasing ocean area with increasing depth, assuming in a first order approximation that steric anomalies from all depths are distributed evenly across the entire ocean surface. However, local bottom pressure anomalies can deviate by a similar order of magnitude from the global mean. This heterogeneous pattern reflects the differences in deep water formation in different ocean basins, thus affecting the penetration depth of the steric anomalies.

Our simulated pattern of ocean bottom pressure anomalies leads to secular Earth rotational excitation of the axial component on relatively long time scales, corresponding to ΔLOD of nearly -0.12 ms after 200 years. Due to the somewhat fortuitous averaging out of longitudinal differences of bottom pressure anomalies between ocean basins (there is no dependence on longitude in the integration kernel in equation 4.4), changes in χ_3^{mass} can be largely explained by the simple redistribution model. This finding implicitly links a global mean sea level rise to a reduction of LOD.

In a slightly different warming scenario, de Viron et al. (2002) analyzed ΔLOD from an ensemble of coupled models. Under the assumption that the total mass term (atmosphere and ocean) is given only by the atmospheric mass term and the IB term over the ocean, they derive a mean ΔLOD trend of -0.75μs/year for the mass term (their Table 2). However, as we show here, taking into account the term $\eta' - \eta'_s$ in equation 4.2 for the ocean mass term yields an additional trend of similar magnitude of -0.57 μs/yr. Ideally, this comparison should be done with the atmosphere mass term of the current generation IPCC-AR4 models, but this is beyond the scope of this paper. Our results are somewhat

in contrast to Ponte et al. (2002), who did not detect significant LOD trends from ocean bottom pressure changes in a similar warming scenario simulation. We speculate that the discrepancy could be attributed to differences of the ocean warming patterns between the two simulations, and also to model improvements in ECHAM5/MPI-OM over HadCM2, which was used by Ponte [R. Ponte, 2006, personal communication].

On timescales of a few years and shorter, nontidal LOD variations are on the order of a few milliseconds, caused primarily by atmospheric angular momentum changes (Gross et al., 2004). Nontidal LOD variations on decadal and longer periods are primarily related to core-mantle interaction, with the atmosphere and oceans being relatively ineffective in exciting variations at these low frequencies (Gross et al., 2004). However, as we demonstrate here, ocean warming and the ensuing mass redistribution on these long time scales lead to a sizeable nontidal LOD anomaly. In principle, this anomaly is large enough to be measured and, in conjunction with observations of ocean thermal expansion, could help to constrain residuals (e.g. from core-mantle interaction) of future ΔLOD measurements.

Acknowledgments We thank E. Maier-Reimer for interesting discussions and the reviewers for helpful comments. This work was supported by the Max Planck Society and the International Max Planck Research School on Earth System Modelling. The computer simulations were performed at the DKRZ (Deutsches Klimarechenzentrum) in Hamburg, Germany.

4.7 Appendix

4.7.1 Associated Mass Transport

The proposed mass redistribution process in section 4.3 must be accomplished by a corresponding transport. In the simple horizontally averaged model, this transport is given by

$$T = \frac{d}{dt} \sum_i \eta_s (A_s - A_i), \tag{4.5}$$

with the definition of the terms as in Eq. 4.3. Defined this way, negative transports are from shallow to deep regions, and positive transports are from deep to shallow regions (the direction associated with a depth penetrating warming signal). Maximum transports reach values of 0.007 Sv for short time intervals, but are usually confined to less than 0.005 Sv for most of the times. This transport is extremely small compared to typical transport magnitudes in the ocean (10-150 Sv), and could not be detected as current anomalies.

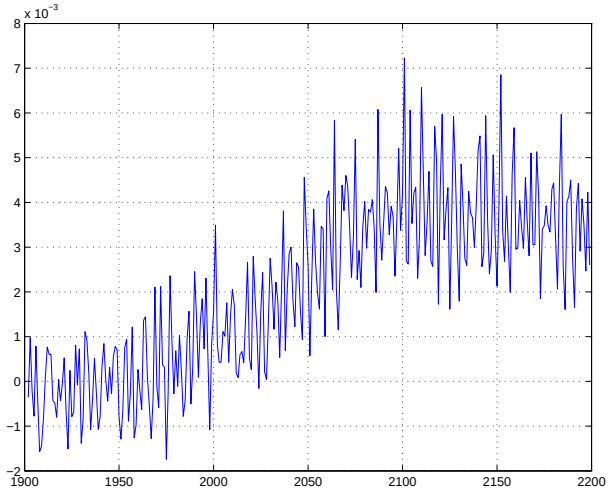

Figure 4.5: *Volume transport (in Sv) computed from the simple redistribution model.*

4.7.2 Effect of mass redistribution on clathrate

The clathrate inventory at the ocean floor is highly sensitive to temperature, and weakly sensitive to the pressure at the sea floor. Increasing the bottom pressure at the seafloor by changes in sea level increases the thickness of the gas hydrate stability zone, whereas higher bottom temperatures reduce the thickness of the stability zone (Buffett and Archer, 2004). In a global warming scenario as described here, higher temperatures at the bottom

will always produce a net decrease in the seafloor clathrate inventory, regardless of the bottom pressure increase through mass redistribution. Therefore, the mass redistribution associated with ocean warming cannot mitigate dangerous clathrate release from the ocean to the atmosphere, which would feed back positively onto the greenhouse effect.

5 The Effect of Steric Sea Level Changes on the Excitation of Polar Motion and Length-of-Day

Abstract

We calculate ocean angular momentum (OAM) changes that arise (1) from horizontal mass redistribution within the global oceans, and (2) from large-scale current changes in the 21st century as simulated with a coupled climate model. We find that the OAM signals are mainly excited by the mass terms, while ocean current changes play a secondary role. Previously, we showed that ocean thermal expansion leads to secular horizontal mass redistribution within the oceans, without changing the total ocan mass (Landerer et al., 2007b). The simulated long-term oceanic polar motion excitation from steric sea level rise is nearly linearly polarized along the 30°E-150°W plane, similar to the polarization of observed decadal polar motion (post-glacial rebound signal subtracted). However, polar motion inferred from observed thermal expansion during the last 50 years is too small to account for the observed polar motion during the last 50 years, suggesting that other mechanisms play a more important role in exciting the observed decadal variations in polar motion. The simulated secular increase of eastward Antarctic-Circumpolar-Current (ACC) transport is reflected in a pronounced positive length-of-day (LOD) contribution from this latitude, but a westward oriented return flow just north of the ACC largly balances the LOD signal from the ACC spin up. The latitudinal LOD excitation from ocean mass redistribution is negative from 90°S to 20°N, and positive between 20°N to 90°N, reflecting the sign of the zonally integrated ocean mass load anomalies.

5.1 Introduction

Geophysical processes on or near Earth's surface, including the atmosphere, oceans and continents, can significantly influence Earth's angular momentum budget on a variety of time-scales (e.g., Barnes et al., 1983; Celaya et al., 1999; Gross et al., 2004). Due to the requirement that the total angular momentum of the Earth system be conserved, changes in the large-sale atmospheric flow or oceanic current pattern, or surface mass redistribution, can excite motion of Earth's rotation axis (polar motion, from here on denoted as PM), and changes of Earth's rotation rate or length-of-day (LOD). Atmospheric angular momentum (AAM) and oceanic angular momentum (OAM) effects have been studied extensively, and are found to excite complex motions of Earth's rotation axis on a variety of time-scales (Chao, 1994; Ponte et al., 2002; de Viron et al., 2002; Gross et al., 2003, 2004). Ponte et al. (1998) found that ocean circulation and mass field variability play an important role in fortnightly to seasonal polar motion, and the most prominent polar motion wobble, the annual so-called free Chandler wobble, is excited mainly by ocean bottom pressure variations (Gross, 2000; Gross et al., 2003). Larger discrepancies between observed and simulated polar motion variations remain for the interannual to decadal frequency band (Gross et al., 2003). Model results suggest that on periods longer than 10 years, the oceans appear to be capable of exciting some nontrivial polar motion, yet the mechanisms are poorly understood (Celaya et al., 1999). In particular, the excitation sources for quasi-periodic wobbles (commonly referred to as 'Markowitz' wobble) of Earth's rotation pole with a period of about 30 years and amplitudes of nearly 30 mas (milli-arcseconds) are poorly understood (Gross et al., 2003). The polarization orientation of the observed Markowitz wobble is approximately along 45°E-135°W (Celaya et al., 1999), which is fairly close to the polar motion that a simple eustatic sea level change with uniform load variations over land is expected to excite (Wilson, 1993). Therefore, the oceans are a prime suspect as a cause for this wobble, but attempts to link eustatic sea level changes to the observed wobble amplitudes have not met with much success, either because the eustatic sea level changes required are too large, or because the sources for a realistic eustatic sea level change are not observed to contribute to sea level in the way they would need to in order to drive the excitation (Celaya et al., 1999). The conflict between astronomical constraints and observed sea level rise in the 20th century has become known as the 'sea level enigma' (Munk, 2002).

Steric sea level changes are usually not considered to give rise to sizable geodynamic effects, due to a lack of significant geophysical mass redistribution (e.g., Chao, 1994). However, we have recently analyzed the response of the global ocean to anthropogenic warming, both in terms of the pattern of dynamic and steric sea level changes and of large-

scale circulation changes (Landerer et al., 2007c). Based on these results, we proposed a simple effective mechanism by which ocean warming (and hence steric expansion) leads to significant horizontal mass redistribution within the oceans, and thus to sizeable changes of Earth's moment of inertia. The general pattern of the steric mass redistribution in the ocean is such that shallow ocean areas generally gain mass, while the deep ocean regions generally loose mass when steric sea level rises (Landerer et al., 2007b). Since ocean warming is a relatively slow process, this provides a gateway for an effective OAM excitation on relatively long time-scales, but it does not require eustatic sea level sources, and is thus subject to weaker constraints.

Under anthropogenic climate change from continued emission of greenhouse gases, the oceans are expected to respond with circulation changes as well as significant heat uptake and steric sea level rise (Church et al., 2001). Recently, we have reported on a decreasing length-of-day signal as a consequence of horizontal mass redistribution from simulated ocean warming (Landerer et al., 2007b). Here, we extend this analysis and examine the effect of the same horizontal ocean mass redistribution on polar motion; additionally, we examine the latitudinal contribution to the simulated length-of-day changes, and we calculate the excitation of relative OAM from the simulated changes of the large-scale oceanic flow under an anthropogenic warming scenario.

5.2 Model and Methods

5.2.1 The ECHAM5/MPI-OM Model

We use results from a simulation performed with coupled atmosphere-ocean general circulation model ECHAM5/MPI-OM (Marsland et al., 2003; Roeckner et al., 2003; Jungclaus et al., 2006), forced with the A1B scenario from the Intergovernmental Panel on Climate Change (IPCC) (Nakicenovic and Swart, 2000). The model's sea level response to the A1B scenario has been extensively analyzed in (Landerer et al., 2007c); using the same simulated data in a previous paper, we have also analyzed length-of-day changes resulting from horizontal mass redistribution that arise from ocean warming and steric expansion (Landerer et al., 2007b). We refer the reader to these papers for a detailed discussion on these topics. Note that the total ocean mass is constant in our analysis: eustatic sea level change, e.g. from ice sheet melting, is not considered. Global mean sea level varies only due to ocean heat uptake. All following data are annual means, and represent deviations from a mean preindustrial climate state (before the year 1860).

5.2.2 Effective Angular Momentum Functions

The angular momentum (AM) vector of the Earth's fluid envelope (atmosphere and ocean) can be split into two terms: a mass term, which relates the solid body rotation to the surface mass loads induced by atmospheric surface and ocean bottom pressure, and a motion term, which relates Earth's rotation to relative angular momentum carried by fluid motion relative to the solid earth. The so-called effective angular momentum (EAM) functions describe these Earth rotation signals. They are obtained by integrating mass load and fluid flow anomalies over the surface of the sphere (Barnes et al., 1983):

$$\chi_1^{mass} = -\frac{R_e^2}{(I_{zz}-I_{xx})g}\iint \Delta p \sin\theta\cos\theta\cos\lambda\, dS \tag{5.1}$$

$$\chi_2^{mass} = -\frac{R_e^2}{(I_{zz}-I_{xx})g}\iint \Delta p \sin\theta\cos\theta\sin\lambda\, dS \tag{5.2}$$

$$\chi_3^{mass} = \frac{R_e^2}{I_{zz}g}\iint \Delta p \cos^2\theta\, dS \tag{5.3}$$

$$\chi_1^{motion} = -\frac{1.43R}{(I_{zz}-I_{xx})\Omega_0 g}\iint (\Delta U \sin\theta\cos\lambda - \Delta V \sin\lambda)\, dS \tag{5.4}$$

$$\chi_2^{motion} = -\frac{1.43R}{(I_{zz}-I_{xx})\Omega_0 g}\iint (\Delta U \sin\theta\sin\lambda + \Delta V \cos\lambda)\, dS \tag{5.5}$$

$$\chi_3^{motion} = \frac{R_e}{I_{zz}\Omega_0 g}\iint \Delta U \cos\theta\, dS \tag{5.6}$$

where R_e is the Earth's mean radius, $dS = R_e^2\cos\theta\, d\theta\, d\lambda$ is the area element, I_{zz} and I_{xx} are the polar and equatorial moments of inertia of Earth's mantle, respectively, Ω_0 is the mean angular velocity, g the gravitational acceleration, and Δp is the pressure anomaly; ΔU and ΔV are the vertically integrated meridional and zonal ocean transport anomalies, respectively. In the derivation of the EAM functions, the axial symmetric approximation has been made ($I_{xx} = I_{yy}$). The total effective angular momentum for each vector component ($i = 1, 2, 3$) is simply the sum of the mass and motion term:

$$\chi_i = \chi_i^{mass} + \chi_i^{motion}. \tag{5.7}$$

The vector components $\chi_{1,2}$ represent changes about the equatorial plane and are chosen to point to the 0° (Greenwich) and 90°E meridian, respectively. Thus, $\chi_{1,2}$ describes the magnitude and direction of motion of Earth's rotation pole. The component χ_3 describes variations of the angular velocity of Earth's rotation axis, and can be expressed in terms of length-of-day anomalies (ΔLOD), with $\Delta\text{LOD} = \text{LOD}\,\chi_3$, where LOD = 86400 s is the nominal reference length-of-day. Note that the χ_{mass} terms are related to the time-variable geopotential field, and are proportional to the degree-two Stokes geopotential coefficients

(Chen, 2005).

5.3 Results

5.3.1 Excitation of Polar Motion Anomalies

While interannual variability is stronger in χ_2^{mass} compared to the χ_1^{mass} component, the secular response to the A1B scenario is larger in χ_1^{mass} by a factor of about 2.5. Stronger interannual variability in the χ_2^{mass} component (corresponding to the 90°E - 90°W plane) was also found by (Gross et al., 2003), but it appears not to be entirely clear why this direction should be preferred. We note, however, that the 90°E - 90°W plane roughly separates the Atlantic and Indian Oceans from the Pacific Ocean. Previously, we could show that there is considerable interannual ocean bottom pressure variability between the Atlantic and Indian Oceans on the one hand, and the Pacific Ocean on the other hand. Part of this large scale pattern can be related to interannual tropical Pacific Ocean climate variability, and this pattern emerges mainly in the χ_2^{mass} component (Landerer et al., 2007a). Note also that the mass and motion terms of χ_2 vary in phase on interannual time scales, indicating that pressure-driven geostrophic circulation variability is closely connected to the dynamic mass redistribution (Ponte and Stammer, 1999; Celaya et al., 1999). Apart from interannual variations, both polar motion components, χ_1 and χ_2, show significant negative trends from about the year 2000 on, and these trends are primarily related to the mass term (Fig. 5.1). The motion term χ_1^{motion} shows a small increase from about the year 2000 on, and thus reduces the overall χ_1 signal by about 10%, whereas the motion term χ_2^{motion} shows a small decrease and thus increases the overall χ_2 signal by about 20%.

As described in detail in Landerer et al. (2007b), the response of the mass terms is related to horizontal mass redistribution occurring concurrently with thermosteric sea level rise. Since ocean warming and global mean steric sea level rise does not reach significant amplitudes during the 20th century in our simulation (Landerer et al., 2007c), the polar motion signal in both, χ_1 and χ_2 is evident only from about the year 2000 on. From the total oceanic polar motion contribution of χ_1 and χ_2, we infer that the trace of the long-term polar motion at the pole is, to a very good approximation, linearly polarized along the 30°E-150°W plane (Fig. 5.1 d). A linear regression of the simulated polar motion vector magnitude on steric sea level rise yields an excitation power of about 7.4×10^{-9} rad per 10 mm of steric sea level rise. Leaving aside for now the fact that our simulated polar motion excitation does not wobble (because the sea level change is in one direction), and that there is no significant signal simulated in the 20th century, the general amplitude of

the long-period motion for the 21st century in Fig. 5.1 d is quite similar to observed polar motion variations for the 20th century, e.g., as reported in Celaya et al. (1999) (their Fig. 5). We will return to this point in Sec. 5.4.

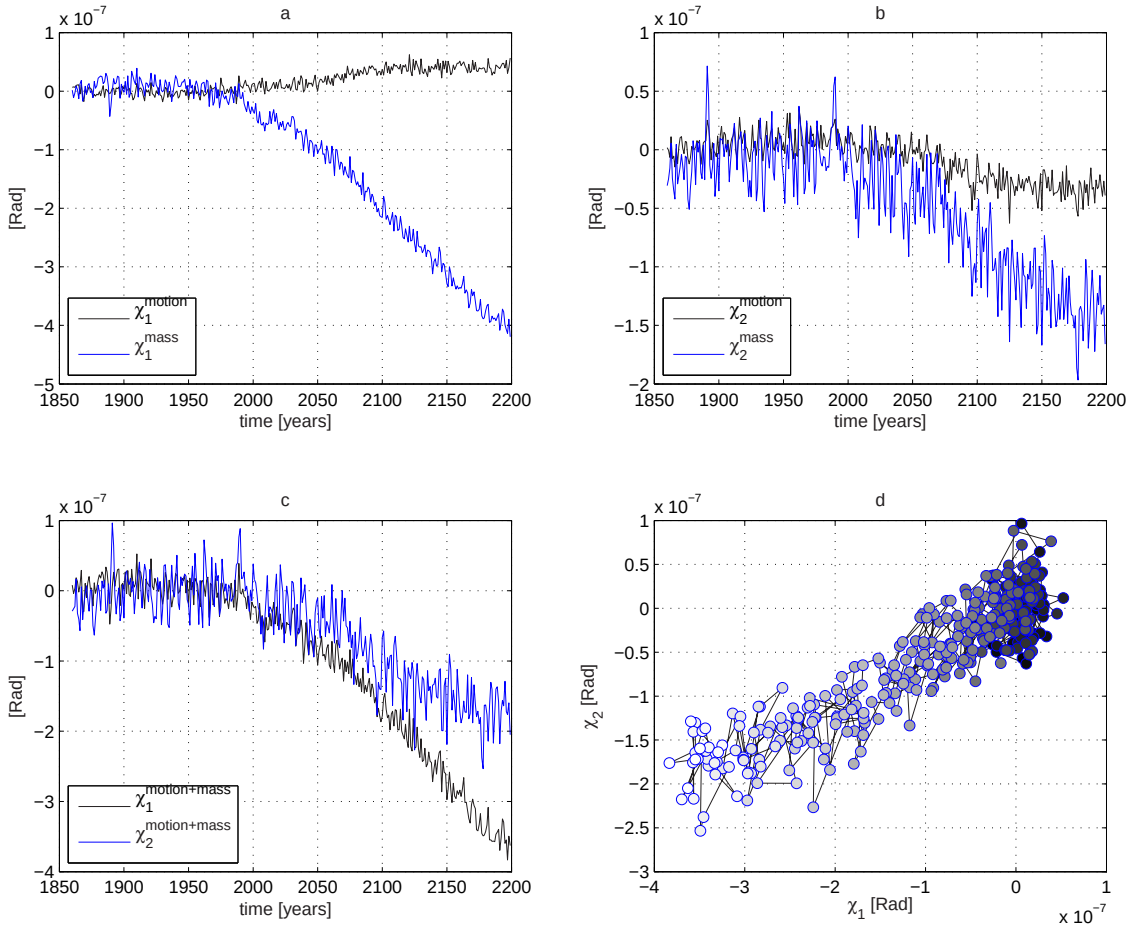

Figure 5.1: *a) χ_1 mass and motion excitation terms; b) χ_2 mass and motion excitation terms; c) Total oceanic polar motion excitation χ_1 and χ_2 as the sum of mass and motion terms; d) Trace of polar motion at the pole. The marker color indicates the time evolution (darkest grey: year 1860; lightest grey: year 2199). Shown are the deviations relative to the preindustrial (pre-1860) climate.*

5.3.2 Excitation of Length-of-Day Anomalies

We recently analyzed the length-of-day signal resulting from the horizontal mass redistribution by ocean steric expansion (Landerer et al., 2007b). Here, we add the contribution from zonal current changes, and evaluate the distribution with latitude of the integral of both components (χ_3^{motion} and χ_3^{mass}; Eq. 5.1).

The horizontal mass redistribution in the ocean leads to decrease in the length-of-day

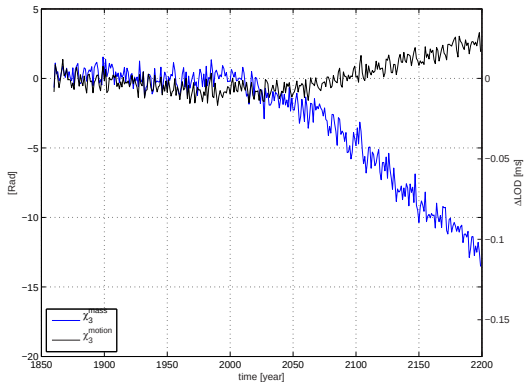

Figure 5.2: *Mass and motion term of the axial OAM χ_3 excitation. Shown is the deviation relative to the preindustrial (pre-1860) climate.*

signal of about 0.12 ms towards the year 2199, whereas the motion term shows a small increase of about 0.026 ms at that time (Fig. 5.2). A decrease of the length-of-day mass term suggests a net movement of mass closer to Earth's rotation axis. The distribution with latitude of the mass-related length-of-day trend ($\chi_3^{mass} \times$ LOD with the meridional integration not performed) reveals that the signal is not symmetric between the southern and northern hemisphere (Fig. 5.3 a): throughout the southern hemisphere, negative trends indicate that there is a net movement of mass to the northern hemispheres; in the northern hemisphere, negative values between 0°N and 20°N (except for a small strip around 10°N) and positive values above 20°N are consistent with a net movement of mass closer to the rotation axis. The asymmetric signal between the two hemispheres is a direct consequence of the ocean-continent distribution, which also results in considerably more shallow shelf area in the northern latitudes.

An increase of the LOD motion term suggests a net increase of eastward barotropic currents in the ocean. Except for the Southern Ocean, all ocean basins have zonal boundaries. Therefore, net zonal flows require a matching zonal return flow at some other latitude. As pointed out by Brosche and Sündermann (1985), this does not preclude OAM excitation from these currents, since the return flow can be at a different latitude and thus have a different radius vector. For example, the large-scale subtropical and subpolar ocean gyres have a net angular momentum, so changes of these could be a source for OAM excitation. However, the Antarctic Circumpolar Current (ACC) is a largely zonal current that has no zonal boundaries and hence no compensating return flow. It therefore carries considerable OAM with it, and is a prime source for OAM due to current anomalies (Brosche and Sündermann, 1985). In the present warming scenario simulation, the ACC eastward transport increases moderately by about 6% (170 Sv at year 2100 compared to 160 Sv preindustrial value (Landerer et al., 2007c)).

Based on the simulated ocean current changes, we find that the distribution with latitude of the motion-related length-of-day trend ($\chi_3^{motion} \times \Delta$LOD with the meridional integration not performed) has large positive contributions in the latitude band from 45°S to 70°S, consistent with an ACC spin up. However, an equally prominent, but opposite signal between 30°S and 45°S cancels the ACC signal almost completely when the integration over latitude is performed, so that the remaining net positive length-of-day signal of the integrated motion term is mostly excited at latitudes between 30°S and the equator (Fig. 5.3 b). Based on previous results, we can relate the negative excitation between 30°S and 45°S to westward oriented velocity changes along the ACC front in the Atlantic and Indian Ocean sector, which are also evident in a prominent pattern of sea surface height changes in this region (Landerer et al., 2007c).

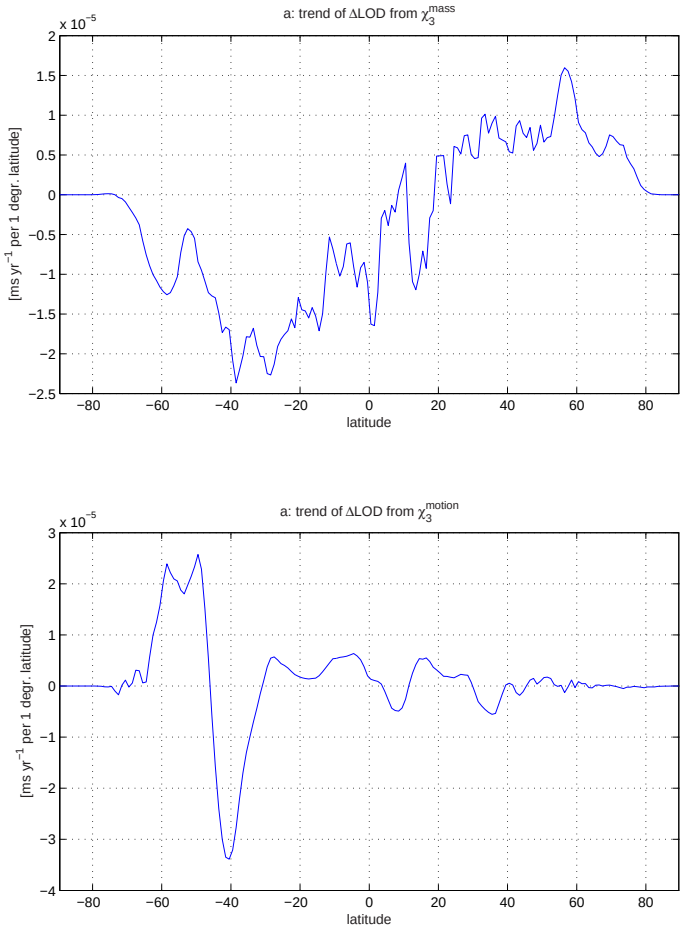

Figure 5.3: *Trend of the distribution with latitude of (a) the χ_3 mass and (b) the χ_3 motion term in equivalent ΔLOD. Units: ms yr^{-1} per 1 degr. latitude. Shown are the deviations relative to the preindustrial (pre-1860) climate.*

5.4 Summary and Conclusion

We have shown that OAM on decadal to centennial time scales is significantly influenced by ocean warming and corresponding steric sea level rise. The OAM mass terms have the largest excitation power, whereas the relative motion terms due to ocean current changes are considerably smaller in amplitude and play a secondary role. The pertinent point here is that the detected OAM signal evolves at constant ocean mass, and so does not require any eustatic sea level changes from melting of large ice-sheets or glaciers.

For the polar motion excitation, we find that the detection of an oceanic warming signal is more likely in χ_1 than in χ_2, because the χ_2 trend is smaller, and additionally masked by stronger interannual variability. The simulated oceanic long-term polar motion is nearly linearly polarized along the 30°E-150°W plane. A simple eustatic sea level change with uniform load variations over land would result in a polar motion trace oriented along the 53°E-128°W plane (Wilson, 1993), and the observed long-term polar motion (corrected for polar motion due to post-glacial rebound) is oriented approximately along 45°E-135°W (Celaya et al., 1999). The orientation of the polar motion that we relate to steric sea level changes is surprisingly similar to both the polar motion orientations expected from a eustatic sea level change, and the observed polarization. A priori, there appears to be no reason that a steric and eustatic sea level should lead to a similar polarization of the polar motion trace, because the mechanisms involved are completely different. So far, it has been difficult to find an adequate eustatic sea level source that would provide a reasonable source for the sea level change necessary to drive the polar motion (Celaya et al., 1999; Munk, 2002, ; and references therein). Since our calculation does not involve eustatic sea level change, we thus avoid the need of a source for a eustatic sea level change, and our results suggest that steric sea level changes and the associated mass redistribution provide a mechanism to excite long-term polar motion along a trace similar to what is observed. The question now is: if the suggested mechanism of ocean warming and steric expansion leading to OAM excitation is real, what would the OAM signal from observed ocean warming during the last 50 years be? The thermal expansion of the global oceans during the last 50 years is estimated to lie between 0.3-0.7 mm/yr (Cazenave and Nerem, 2004). Taking a central value of 0.5 mm/yr and the regression value of 7.4×10^{-10} rad/mm from Sec. 5.3.1, the warming signal during the last 50 years would have resulted in an average polar motion excitation of about 3.7×10^{-10} rad/yr. While the polarization of this excitation is broadly consistent with what is observed (Fig. 5 in Celaya et al. (1999)), the amplitude falls short by roughly two orders of magnitude. Thus, ocean warming and resulting horizontal mass redistribution would have had only a minute influence on decadal polar motion during the last 50 years. Note, however, that beyond the Markowitz

wobble, the observed polar motion spectrum features also longer-period, more irregular signals (Schuh et al., 2001). Likely other causes for decadal polar motion variations are global mass redistribution in the atmosphere, hydrosphere and cryosphere, as well as core-mantle interaction within the solid Earth and post-glacial rebound (Schuh et al., 2001, and references therein).

For length-of-day excitation, we find a considerable hemispheric asymmetry in the latitudinal contributions to the mass and motion term. Ocean mass redistribution due to ocean warming is from the southern to the northern hemisphere, but also to high northern latitudes. Through this process, mass is effectively moved closer to Earth's rotation axis, resulting in a decreasing length-of-day signal of about 0.12 ms after 200 years, when steric sea level has risen about 0.56 m relative to its preindustrial value (Landerer et al., 2007b). The length-of-day motion term has large amplitudes between 45°S to 70°S, but the signals have opposing sign and largely cancel. Therefore, the net positive length-of-day signal from the motion mainly originates from the latitude band between 30°S and the equator, but plays only a secondary role in the combined length-of-day excitation.

Essentially, the proposed horizontal mass redistribution through steric sea level changes eliminates a degree of freedom that has proven troublesome in the reconciliation between observations and model predictions of Earth rotational excitation and observed sea level change. However, while the inferred sign of the length-of-day signal and the inferred direction of the polar motion work towards closing the gap highlighted by Munk (2002), the inferred amplitudes are too small. Thus, a full solution of the 'sea level enigma' awaits further study.

6 Conclusions and Outlook

In the introduction to this thesis, I brought up a set of research questions. I conclude the thesis by briefly answering these questions, and by giving an outlook on implications and possible future extension of the results presented here.

6.1 Conclusions

Natural Variability

- **Can a fully coupled climate model simulate the observed seasonal cycling of water between the oceans, atmosphere and continents?**

  The simulated seasonal cycling of water between the oceans, atmosphere and continents in the coupled atmosphere–ocean general circulation model ECHAM5/MPI-OM compares well with observations and uncoupled model results.

  The simulated seasonal eustatic sea level varies with an amplitude of 9.1 ± 2.8 mm. The continental water storage balances most of the eustatic sea level variation, with nearly equal maximal contributions from soil moisture and snow of about 6 mm. Atmospheric water vapor has a comparatively small contribution to the seasonal water cycle with an amplitude of 2.2 ± 0.6 mm.

  These numbers agree well with observational estimates (within error bars). This is a particular important result since ECHAM5/MPI-OM is not constrained by observations, and does not require any flux adjustments. The model can therefore be regarded as an independent tool to assess climate variability.

- **Can the El Niño-Southern Oscillation (ENSO) as an important, large-scale coupled ocean–atmosphere mode, generally be associated with a sea level change, and if so, does this sea level anomaly have an eustatic contribution and how is it balanced? What is the ENSO-related water budget of the continents and atmosphere?**

Based on monthly data of simulated natural climate variability over 200 years, I do not find a statistically significant eustatic sea level change associated with ENSO. Steric sea level variations, essentially representing ocean heat content changes, have a small positive, but significant regression relation with ENSO (represented in this study by the Nino3 index): steric sea level increases by about 0.7 mm/σ(Nino3), leading the Nino3 index by one month (σ denotes the standard deviation). However, only 7.5% of the simulated steric sea level variance can be explained with the Nino3 index, indicating that other processes substantially influence non-seasonal steric sea level variations. Nonetheless, the combined steric and eustatic sea level change with ENSO is close to 1 mm/σ(Nino3), lagging the Nino3 index by four months.

The simulated atmospheric water vapor content is highly correlated with the Nino3 index: nearly 67% of its variance can be explained with the Nino3 index. Lagging the Nino3 index by 3 months, atmospheric water vapor increases by 0.54 ± 0.01 mm/σ(Nino3). Water storage on the continents is reduced during ENSO by nearly 1 mm/σ(Nino3), but although this regression signal is statistically significant, the variance of the continental water storage explained with Nino3 is only 14%.

The analysis of non-seasonal monthly continental and atmospheric water storage and eustatic sea level anomalies show that the water budget is mostly balanced between eustatic sea level and continental water storage (in the form of soil moisture), because the atmospheric water storage capacity is very limited by the temperature dependent saturation pressure. Examining individual simulated ENSO events and the concurrent continental water storage and eustatic sea level anomalies, I find that large continental water storage and eustatic sea level changes occur for individual ENSO events, but neither their sign nor their magnitude is consistent. Whether or not ENSO events cause an eustatic sea level change depends on the location of large-scale precipitation anomalies over the continents or over the oceans. This atmospheric pattern can vary for different ENSO events, and henceforth no significant eustatic sea level signal is detected by the linear regression on ENSO.

- **Can hydrological mass redistribution from the El Niño-Southern Oscillation generally be associated with a significant degree-two geopotential signal, and if so, what are the geographical patterns and contributions in the atmosphere and on the continents that lead to this anomaly?**

  As outlined in the introduction, the degree-two geopotential Stokes coefficients (denoted by C_{21}, S_{21} and C_{20}) are very important because they are linked to polar

motion and length-of-day (e.g., Chao, 1994), providing two independent methods to determine large-scale mass redistribution in the Earth system.

Based on monthly data of simulated natural climate variability over 200 years, I find that the distribution of non-seasonal water mass load anomalies on Earth's surface leads to significant ENSO related changes in the S_{21} and C_{20} Stokes coefficients, but not to a significant change in the C_{21} coefficient. For S_{21}, the main contribution comes from the anomalous distribution of dynamic ocean bottom pressure, closely followed by soil moisture. For C_{20}, the main contribution comes from the anomalous pattern of soil moisture.

Starting in 1997, a pronounced C_{20} anomaly, lasting for about four years, was observed (Cox and Chao, 2002), and it was inferred that the oceans or large ice-sheets could be an important source for the observed anomaly (Dickey et al., 2002). Since the period 1997/1998 was marked by a strong ENSO event, it was hypothesized that ENSO typically leads to large-scale mass redistribution in the Earth system, in particular within the oceans. However, I do not find a significant contribution to C_{20} from ocean bottom pressure anomalies as a typical ENSO response. Instead, the simulation points to the importance of continental water storage, especially from soil moisture. However, the regression amplitude of C_{20} is still too small to explain the observed C_{20} anomaly. Therefore, I cannot rule out other excitation sources such as the solid Earth or the large Antarctic and Greenland ice sheets for the observed 1997/1998 C_{20} anomaly.

Anthropogenic Signals

- **What are the dynamic processes that lead to the projected geographical pattern of sea level change under anthropogenic warming? In particular, in light of an expected slow down of the meridional overturning circulation (MOC) in the North Atlantic under anthropogenic warming (e.g., Marotzke, 2000), can the observation of regional sea level change in the North Atlantic be utilized to detect changes of the MOC?**

  Similar to results in previous studies, I also find that the geographical pattern of projected sea level change is highly variable. In the Arctic Ocean, sea level experiences the strongest increase due to enhanced freshwater input from precipitation, river runoff and melting sea ice. Sea level changes are minimal in the Southern Ocean due to increased wind stress, which leads to a stronger Antarctic Circumpolar Current transport and a subsequent dynamic sea level adjustment.

In an anthropogenically unperturbed climate, the simulated sea level difference between the North Atlantic and Pacific Ocean is about 0.78 m. This difference is reduced under the IPCC-A1B scenario by 0.06 m towards the year 2100, coinciding with a minimum of the North Atlantic meridional overturning rate. However, the basin-integrated sea level difference between the North Atlantic and Pacific Ocean is reestablished within 100 years through a Pacific Ocean sea level rise and a North Atlantic sea level drop, without an analogous recovery of the North Atlantic meridional overturning rate.

Additionally, I find that on interannual to decadal timescales, the sea level difference between Bermuda and the Labrador Sea correlates highly at zero lag with the combined North Atlantic gyre transport. On the other hand, changes of the meridional overturning circulation in the North Atlantic evolve on different timescales and cannot be reliably inferred from observations of sea level pattern or gyre transport changes.

- **What is the horizontal and vertical structure of the contribution to steric changes? How do temperature and salinity contribute to this structure, and what mechanisms are involved?**

  I find that thermosteric sea level change by 2100 is positive in almost all ocean regions, but varies considerably by region. Halosteric effects in the North Atlantic subtropical region partly compensate thermosteric sea level rise. In contrast, freshening in the Arctic Ocean leads to an additional halosteric sea level rise. Steric anomalies in the Pacific Ocean are generally positive, but of smaller magnitude.

  The vertical distribution of thermosteric and halosteric anomalies that contribute to sea level change is very different between ocean basins. In the North Atlantic, the steric anomalies reach to depths of the North Atlantic Deep Water (2000 m), whereas steric anomalies in the entire Pacific Ocean occur mainly in the upper 500 m. In the Southern Ocean, steric anomalies occur throughout the entire water column, reflecting the strong vertical exchange of buoyancy in this region. The heterogeneous pattern of thermosteric sea level indicates the geographical variation of ocean heat uptake and redistribution, whereas the pattern of halosteric sea level changes reflects changes of the large-scale hydrological cycle, and to a lesser extent anomalous salinity advection in the ocean.

Earth Rotational Signals

- **Does the simulated sea level change under the IPCC-A1B scenario lead to detectable signals in ocean angular momentum such as Polar Motion and Length-of-Day? What mechanisms of mass redistribution in the ocean are involved? Can this at least partially resolve the 'sea level enigma'?**

  Ocean warming and the associated steric expansion does not affect the total ocean mass. Therefore, steric sea level change has so far not been related to significant large-scale mass redistribution on Earth's surface (Chao, 1994). However, I find that ocean warming and circulation changes lead to significant secular bottom pressure changes in a warming climate. The bottom pressure changes are due to a horizontal mass redistribution that can partly be related to a newly developed simple redistribution model. This conceptual model estimates bottom pressure anomalies as they should occur in a warming (or cooling) ocean due to the decreasing ocean area with increasing depth. An essential feature of the resulting geographical pattern are the strong positive bottom pressure anomalies on almost all shelf areas, while deep ocean regions show negative bottom pressure anomalies. Large-scale bottom pressure changes related to barotropic current changes are also seen in the climate change simulation, in particular in the Antarctic-Circumpolar-Current region.

  The simulated pattern of ocean bottom pressure anomalies leads to significant secular changes of ocean angular momentum (OAM). The excitation of the axial OAM component, related to Earth's angular velocity, is equivalent to a decrease in the length-of-day of nearly -0.12 ms towards the end of the 22nd century (global mean sea level is simulated to rise 0.56 m by then). The excitation of the equatorial OAM component, related to horizontal motions of Earth's rotation pole, is linearly oriented towards 150°W, with a rate of 7.4×10^{-9} rad per 10 mm of steric sea level rise (equivalent to a lateral rotation pole displacement of about 50 mm per 10 mm of steric sea level rise, or about 1.5 mas (milli-arcseconds) per 10 mm of steric sea level rise). With an observed thermosteric sea level rise of about 0.5 mm/year during the last 50 years, the secular polar motion rate due to ocean warming would be about 0.08 mas/year. This is arguably a small value compared to what is observed (something on the order of 1-3 mas/yr (e.g., Schuh et al., 2001)), but the simulated amplitudes are large enough to be observed and place tighter constraints on unknown long-period excitation sources, such as core–mantle interaction. A similar argument holds for the inferred length-of-day changes from ocean warming. As the thermal expansion of the oceans is projected to continue and accelerate into the next century, it will become more important to consider the effects of the simulated ocean mass redistribution in the interpretation of observed Earth rotational signals.

6.2 Final Remarks and Outlook

The simulation of dynamic and steric sea level changes with a coupled climate model has highlighted some aspects that potentially have direct consequences for strategies of future ocean observations. First, as the steric contributions to sea level change reach down to maximum depths of 2500 m in the Atlantic Ocean, and down to depths of at least 3000 m in the Southern Ocean, hydrographic measurements must encompass these depths for a reliable estimate of long-term steric sea level change. This observational requirement is largely fulfilled with the ARGO float system. Second, accurate measurements of salinity become increasingly important, both as a contribution to steric sea level, but also as a measure of changes of the hydrological cycle in a warming climate. Third, the projected pattern of ocean bottom pressure changes in a warming ocean could in principle be detected by time-variable gravity measurements. However, the largest bottom pressure signals are confined to shallow shelf areas, and thus to continental margins. Since geopotential field coefficients are estimated from the GRACE campaign only up to degree and order 120 (equivalent to a wavelength of 300 km), smaller scale features cannot be resolved. In particular, the transition from land to ocean is problematic: load variations on land can leak into the ocean signal, and vice versa. Therefore, it is most likely not possible to isolate the secular ocean bottom pressure signals on the shelves described in this thesis from continental signals (D. Chambers, 2007, pers. communication; Chambers et al., 2007). Fourth, Earth rotational observations should be accurately monitored for the postulated effects from the secular pattern of bottom pressure changes. Since Earth rotation signals are an integrated response of changes in the entire Earth system, it is difficult to estimate the actual detection feasibility of these signals. Arguably, the projected signals are small, but within measurement accuracy. Fifth, the analysis of natural non-seasonal variability of sea level and mass redistribution in the Earth's hydrosphere has highlighted that long, continuous measurements of all components are necessary for the reliable estimate of long-term, presumably anthropogenic, trends of sea level or water storage.

Future research would benefit from an ocean model that is mass-conserving, rather than volume-conserving (as implied by the Boussinesq approximation), because simulated bottom pressure can be somewhat influenced by making the Boussinesq approximation (Huang and Jin, 2002). Also, the largest sea level changes are likely to arise from unbalanced mass budgets of the Antarctic and Greenland ice sheets. Their dynamics are currently not sufficiently understood to be included into climate models, adding a large deal of uncertainty to the simulated projected signals. Closing this gap would greatly improve climate models and projections derived from them.

Bibliography

Antonov, J. I., S. Levitus, and T. P. Boyer, 2002: Steric sea level variations during 1957-1994: Importance of salinity. *J. Geophys. Res.*, **107**, doi:10.1029/2001JC000964.

— 2005: Thermosteric sea level rise, 1957-2003. *Geophys. Res. Lett.*, **32**, L12602, doi:10:1029/2005GL023112.

Barnes, R. T. H., R. Hide, A. A. White, and C. A. Wilson, 1983: Atmospheric angular momentum fluctuations, length-of-day changes and polar motion. *Proc. R. Soc. London A*, **387**, 31–73.

Barnett, T. P., D. W. Pierce, K. M. AchutaRao, P. J. Gleckler, B. D. Santer, J. M. Gregory, and W. M. Washington, 2005: Penetration of human-induced warming into the world's oceans. *Science*, **309**, 284–287.

Brosche, P. and J. Sündermann, 1985: The Antarctic Circumpolar Current and its influence on the Earth's rotation. *Dt. hydrogr. Z.*, **H.1.**, 1–6.

Bryan, K., 1996: The steric component of sea level rise associated with enhanced greenhouse warimng: a model study. *Climate Dyn.*, **12**, 545–555.

Buffett, B. and D. Archer, 2004: Global inventory of methane clathrate: sensitivity to changes in the deep ocean. **227**, 185–199.

Cazenave, A. and R. S. Nerem, 2004: Present-day sea level change: observations and causes. *Rev. Geophys.*, **42**, RG3001.

Cazenave, A., F. Remy, K. Dominh, and H. Douville, 2000: Global ocean mass variation, continental hydrology and the mass balance of Antarctica ice sheet at seasonal time scale. *Geophys. Res. Lett.*, **27**, 3755–3758.

Celaya, M. A., J. M. Wahr, and F. O. Bryan, 1999: Climate-driven polar motion. *J. Geophys. Res.*, **104**, 12,813–12,829.

Chambers, D. P., M. E. Tamisiea, R. S. Nerem, and J. C. Ries, 2007: Effects of ice melting on GRACE observations of ocean mass trends. *Geophys. Res. Lett.*, **34**, L05610, doi:10.1029/2006GL029171.

Chambers, D. P., J. Wahr, and R. S. Nerem, 2004: Preliminary observations of global ocean mass variations with GRACE. *Geophys. Res. Lett.*, **31**, L13310, doi:10.1029/2004GL020461.

Chao, B. F., 1994: The geoid and earth rotation. *Geoid and its geophysical interpretations*, P. Vanicek and N. T. Christou, eds., CRC Press, 285–298.

Chao, B. F., A. Y. Au, J. P. Boy, and C. M. Cox, 2003: Time-variable gravity signal of an anomalous redistribution of water mass in the extratropic Pacific during 1998-2002. *GEOCHEMISTRY GEOPHYSICS GEOSYSTEMS*, **4**, doi:10.1029/2003GC000589.

Chen, J., 2005: Global mass balance and the length-of-day variation. *J. Geophys. Res.*, **110**, B08404, doi:10.1029/2004JB003474.

Chen, J. L. and C. R. Wilson, 2003: Low degre gravitational changes freom earth rotation and geophysical models. *Geophys. Res. Lett.*, **30**, doi:10.1029/2003GL018688.

Chen, J. L., C. R. Wilson, D. P. Chambers, R. S. Nerem, and B. D. Tapley, 1998: Seasonal global water mass budget and mean sea level variations. *Geophys. Res. Lett.*, **25**, 3555–3558, doi:10.1029/98GL02754.

Chen, J. L., C. R. Wilson, X. G. Hu, and B. D. Tapley, 2003: Large-scale mass redistribution in the oceans, 1993-2001. *Geophys. Res. Lett.*, **30**, doi:10.1029/2003GL018048.

Chen, J. L., C. R. Wilson, and B. D. Tapley, 2005: Interannual variability of low-degree gravitational change, 1980-2002. *J. Geodesy*, doi:10.1007/s00190-004-0417-y.

Cheng, M. and B. D. Tapley, 2004: Variation's in the earth's oblatness during the past 28 years. *J. Geophys. Res.*, **109**, B09402, doi:10.1029/2004JB003028.

Church, J., J. M. Gregory, P. Huybrechts, M. Kuhn, K. Lambeck, M. T. Nhuan, D. Qin, and P. L. Woodworth, 2001: *Climate Change 2001: The Scientific Basis*, Cambridge University Press, Cambridge, England, chapter Changes in sea level. 639–693.

Church, J. A. and N. J. White, 2006: A 20th century acceleration in global sea-level rise. *Geophys. Res. Lett.*, **33**, L01602, doi:10.1029/2005GL024826.

Church, J. A., N. J. White, and J. M. Arblaster, 2005: Significant decadal-scale impact of volcanic eruptions on sea level and ocean heat content. *Nature*, **438**, 86–89.

Condi, F. and C. Wunsch, 2004: Measuring gravity field variability, the geoid, ocean bottom pressure fluctuations, and their dynamical implications. *J. Geophys. Res.*, **109**, C02013, doi:10.1029/2002JC001727.

Cox, C. M. and B. F. Chao, 2002: Detection of large-scale mass redistributions. *Science*, **297**, 831–833, doi:10.1126/science.1072188.

Curry, R. G. and C. Mauritzen, 2005: Dilution of the Northern North Atlantic Ocean in recent decades. *Science*, **308**, 1772–1774.

Curry, R. G. and M. S. McCartney, 2001: Ocean gyre circulation changes associated with the North Atlantic Oscillation. *J. Phys. Oceanogr.*, **31**, 3374–3400.

de Viron, O., V. Dehant, H. Goosse, M. Crucifix, and P. C. M. Groups, 2002: Effect of global warming on the length-of-day. *Geophys. Res. Lett.*, **29**.

Dickey, J. O., S. L. Marcus, O. de Viron, and I. Fukumori, 2002: Recent Earth oblateness variations: unraveling climate and postglacial rebound effects. *Science*, **298**, 1975–1977, doi:10.1126/science.1077777.

Dümenil, L. and E. Todini, 1992: A rainfall-runoff scheme for use in the hamburg climate model. *Advances in Theoretical Hydrology, A Tribute to James Dooge*, J. O'Kane, ed., Elsevier, Amsterdam, volume 1, 129?157.

Eubanks, T. M., 1993: Variations in the orientation of the earth. *Contributions of Space Geodesy to Geodynamics: Earth Dynamics*, D. L. Turcotte and D. E. Smith, eds., American Geophysical Union, volume 24 of *Geodynamics Series*, 1–54.

Ganachaud, A. and C. Wunsch, 2000: Improved estimates of global ocean ciculation, heat transport and mixing from hydrographic data. *Nature*, **408**, 453–457.

— 2003: Large-scale ocean heat and freshwater transports during the World Ocean Circulation Experiment. *J. Climate*, **16**, 696–705.

Gill, A. E., 1982: *Atmosphere-Ocean Dynamics*. International Geophysics Series, Academic Press, New York.

Gill, A. E. and P. P. Niiler, 1973: The theory of the seasonal variability in the ocean. *Deep-Sea Res.*, **20**, 141–177.

Gleckler, P. J., K. R. Sperber, and K. AchutaRao, 2006: Annual cycle of global ocean heat content: Observed and simulated. *J. Geophys. Res.*, **111**.

Greatbatch, R. J., 1994: A note on the representation of steric sea level in models that conserve volume rather than mass. *J. Geophys. Res.*, **99**, 12767–12771.

Gregory, J. M., H. T. Banks, P. A. Stott, J. A. Lowe, and M. D. Palmer, 2004: Simulated and observed decadal variability in ocean heat content. *Geophys. Res. Lett.*, **31**, L15312, doi:10.1029/2004gl020258.

Gregory, J. M., J. A. Church, G. J. Boer, K. W. Dixon, G. M. Flato, D. R. Jackett, J. A. Lowe, S. P. O'Farrell, E. Roeckner, G. L. Russell, R. J. Stouffer, and M. Winton, 2001: Comparison of results from several AOGCMs for global and regional sea-level change 1900-2100. *Climate Dyn.*, **18**, 225–240.

Gross, R., 2000: The excitation of the Chandler wobble. *Geophys. Res. Lett.*, **27**, 2329–2332.

Gross, R. S., I. Fukumori, and D. Menemenlis, 2003: Atmospheric and oceanic excitation of earth's wobbles during 1980-2000. *J. Geophys. Res.*, **108**, doi:10.1029/2002JB002143.

— 2004: Atmospheric and oceanic excitation of length-of-day variations during 1980-2000. *J. Geophys. Res.*, **109**, B01406, doi:10.1029/2003JB002432.

Guilyardi, E., 2006: El Ninø mean state seasonal cycle interactions in a multi-model ensemble. *J. Climate*, **26**, 329–348, doi:10.1007/s00382-005-0084-6.

Hagemann, S., 2002: An improved land surface parameter dataset for global and regional climate models. MPI Report 336, Max Planck Institute for Meteorology.

Hagemann, S., K. Arpe, and E. Roeckner, 2006: Evaluation of the hydrological cycle in the ECHAM5 model. *J. Climate*, **19**, 3810–3827.

Hagemann, S. and L. Dümenil, 1998: A parameterization of the lateral waterflow for the global scale. *Climate Dyn.*, **14**, 17–31, doi:10.1007/s003820050205.

Häkkinen, S., 2001: Varibility in sea surface height: A qualitative measure for the meridional overturning in the North Atlantic. *J. Geophys. Res.*, **106**, 13837–13848.

Häkkinen, S. and P. B. Rhines, 2004: Decline of Subpolar North Atlantic Circulation during the 1990s. *Science*, **304**, 555–559.

Heiskanen, W. A. and H. Moritz, 1967: *Physical Geodesy*. W. H. Freeman and Company.

Hinrichsen, D., 1998: *Coastal Waters of the World: Trends, Threats, and Strategies*. Island Press, Washington D.C.

Hu, A., G. A. Meehl, W. M. Washington, and A. Dai, 2004a: Response of the Atlantic thermohaline circulation to increased atmospheric CO_2 in a coupled model. *J. Climate*, **17**, 4267–4279.

Hu, A. X., G. A. Meehl, and W. Q. Han, 2004b: Detecting thermohaline circulation changes from ocean properties in a coupled model. *Geophys. Res. Lett.*, **31**, L13204.

Huang, R. X. and X. Jin, 2002: Sea surface elevation and bottom pressure anomalies due to thermohaline forcing, part I: isolated pertubations. *J. Phys. Oceanogr.*, **32**, 2131–2150.

Hughes, C. W. and V. N. Stepanov, 2004: Ocean dynamics associated with rapid J_2 fluctuations: Importance of circumpolar modes and identification of a coherent Arctic mode. *J. Geophys. Res.*, **109**, doi:10.1029/2003JC002176.

Hughes, T. M. C. and A. J. Weaver, 1994: Multiple equilibria of an asymetric two-basin ocean model. *J. Phys. Oceanogr.*, **24**, 619–637.

IPCC, 2001: *Climate Change 2001: The Scientific Basis*. Intergovernmental Panel on Climate Change, Cambridge University Press, Cambridge, England.

Jungclaus, J. H., N. Keenlyside, M. Botzet, H. Haak, J.-J. Luo, M. Latif, J. Marotzke, U. Mikolajewicz, and E. Roeckner, 2006: Ocean circulation and tropical variability in the coupled model ECHAM5/MPI-OM. *J. Climate*, **19**, 3952–3972.

Knutti, R. and T. F. Stocker, 2000: Influence of the thermohaline circulation on projected sea level rise. *J. Climate*, **13**, 1997–2001.

Landerer, F. W., J. H. Jungclaus, and J. Marotzke, 2007a: Non-seasonal variability in sea level, hydrological mass redistribution, and degree-two geoid coefficients. *in preparation*.

— 2007b: Ocean bottom pressure changes lead to a decreasing length-of-day in a warming climate. *Geophys. Res. Lett.*, **34**, L06307, doi:10.1029/2006GL029106.

— 2007c: Regional dynamic and steric sea level change in response to the IPCC-A1B scenario. *J. Phys. Oceanogr.*, **37**, 296–312, doi:10.1175/JPO3013.1.

Latif, M., E. Roeckner, U. Mikolajewicz, and R. Voss, 2000: Tropical stabelization of the thermohaline circulation in a greenhouse warming simulation. *J. Climate*, **13**, 1809–1813.

Levermann, A., A. Griesel, M. Hoffmann, M. Montoya, and S. Rahmstorf, 2005: Dynamic sea level changes following changes in the thermohaline circulation. *Climate Dyn.*, **24**, 347–354, doi:10.1007/s00382-004-0505-y.

Levitus, S., 1990: Interpentadal variability of steric sea-level and geopotential thickness of the North-Atlantic Ocean, 1970-1974 versus 1955-1959. *J. Geophys. Res.*, **95**, 5233–5238.

Levitus, S., J. Antonov, and T. Boyer, 2005: Warming of the world ocean, 1955-2003. *Geophys. Res. Lett.*, **32**, L02604, doi:10:1029/2004GL21592.

Levitus, S., J. I. Antonov, T. P. Boyer, and C. Stephens, 2000: Warming of the world ocean. *Science*, **287**, 2225–2229, doi:10.1126/science.287.5461.2225.

Lombard, A., D. Garcia, G. Ramillien, A. Cazenave, R. Biancale, J. M. Lemome, F. Flechtner, R. Schmidt, and M. Ishii, 2006: Estimation of steric sea level variations from combined GRACE and Jason-1 data. *EARTH AND PLANETARY SCIENCE LETTERS*, **254**, 194–202, doi:10.1016/j.epsl.2006.11.035.

Macdonald, A. M., 1998: The global ocean circulation: a hydrographic estimate and regional analysis. *Prog. Oceanogr.*, **41**, 281–382.

Marotzke, J., 1997: Boundary mixing and the dynamics of three-dimensional thermohaline circulations. *J. Phys. Oceanogr.*, **27**, 1713–1728.

— 2000: Abrupt climate change and thermohaline circulation: Mechanisms and predictability. *Proc. Nat. Acad. Sci. USA*, **97**, 1347–1350.

Marotzke, J. and B. A. Klinger, 2000: The dynamics of equatorially asymmetric thermohaline circulations. *J. Phys. Oceanogr.*, **30**, 955–970.

Marsland, S. J., H. Haak, J. Jungclaus, M. Latif, and F. Röske, 2003: The Max-Planck-Institute global ocean-sea ice model with orthogonal curvilinear coordinates. *Ocean Modelling*, **5**, 91–127.

McPhaden, M. J., S. E. Zebiak, and M. H. Glantz, 2006: ENSO as an integrating concept in earth science. *Science*, **314**, 1740–1745.

Meehl, G.A., T. Stocker, W. Collins, P. Friedlingstein, A. Gaye, J. Gregory, A. Kitoh, R. Knutti, J. Murphy, A. Noda, S. Raper, I. Watterson, A. Weaver, and Z.-C. Zhao, 2007: *Climate Change 2007: The Physical Science Basis. Contribution of Working Group I to the Fourth Assessment Report of the Intergovernmental Panel on Climate Change*, Cambridge University Press, Cambridge, United Kingdom and New York, NY, USA, chapter Global Climate Projections. 19–91.

Meehl, G. A., W. M. Washington, W. D. Collins, J. M. Arblaster, A. Hu, L. E. Buja, W. G. Starnd, and H. Teng, 2005: How much more global warming and sea level rise? *Science*, **307**, 1769–1772.

Mikolajewicz, U., B. D. Santer, and E. Maier-Reimer, 1990: Ocean response to greenhouse warming. *Nature*, **345**, 589–593.

Mikolajewicz, U. and R. Voss, 2000: The role of the individual air-sea flux components in the CO_2-induced changes of the ocean's circulation and climate. *Climate Dyn.*, **16**, 627–642.

Müller, P. and H. von Storch, 2004: *Computer Modelling in Atmospheric and Oceanic Sciences - Building Knowledge*. Springer Verlag, Berlin - Heidelberg - New York.

Müller, W. and E. Roeckner, 2007: ENSO teleconnections in projection of future climate. *Climate Dyn.*.

Munk, W., 2002: Twentieth century sea level: An enigma. *Proc. Nat. Acad. Sci. USA*, **99**, 6550–6555.

Nakicenovic, N. and R. Swart, eds., 2000: *Emissions Scenarios*. Cambridge University Press.

Nerem, R. S., D. P. Chambers, E. W. Leuliette, G. T. Mitchum, and B. S. Giese, 1999: Variations in global mean sea level associated with the 1997-1998 ENSO event: Implications for measuring long term sea level change. *Geophys. Res. Lett.*, **26**, 3005–3008, doi:10.1029/1999GL002311.

Ngo-Duc, T., K. Laval, J. Polcher, A. Lombard, and A. Cazenave, 2005: Effects of land water storage on global mean sea level oder the past half century. *Geophys. Res. Lett.*, **32**, L09704, doi:10.1029/2005GL022719.

Ponte, R. M., 1999: A preliminary model study of the large-scale seasonal cycle in bottom pressure over the global ocean. *J. Geophys. Res.*, **104**, 1289–1300.

Ponte, R. M., J. Rajamony, and J. M. Gregory, 2002: Ocean angular momentum signals in a climate model and implications for Earth rotation. *Climate Dyn.*, **19**, 181–190, doi:10.1007/s00382-001-0216-6.

Ponte, R. M., D. Salstein, and R. Rosen, 1991: Sea level response to pressure forcing in a barotropic numerical model. *J. Phys. Oceanogr.*, **21**, 1043–1057.

Ponte, R. M. and D. Stammer, 1999: Role of ocean current and bottom pressure variability on seasonal polar motion. *J. Geophys. Res.*, **104**, 23393–23409.

Ponte, R. M., D. Stammer, and J. Marshall, 1998: Oceanic signals in observed motions of the earths' pole of rotation. *Nature*, **391**, 476–479.

Reid, J. L., 1961: On the temperature, salinity, and density differences between the Atlantic and Pacific oceans in the upper kilometre. *Deep-Sea Res.*, **7**, 265–275.

Rio, M.-H. and F. Hernandez, 2004: A mean dynamic topography computed over the world ocean from altimetry, in situ measurements, and a geoid model. *J. Geophys. Res.*, **109**, C12032.

Roeckner, E., G. Bäuml, L. Bonaventura, R. Brokopf, M. Esch, M. Giorgetta, S. Hagemann, I. Kirchner, L. Kornblueh, E. Manzini, A. Rhodin, U. Schlese, U. Schulzweida, and A. Tompkins, 2003: The atmospheric general circulation model ECHAM5, part I: Model description. Technical Report 349, Max-Planck-Institute for Meteorology.

Roesch, A. and E. Roeckner, 2006: Assessment of snow cover and surface albedo in the ECHAM5 general circulation model. *J. Climate*, **19**, 3828?3843.

Schmidt, R., P. Schwintzer, F. Flchtner, C. Reigber, A. Günter, P. Döll, G. Ramillien, A. Cazenave, S. Petrovic, H. Jochmann, and J. Wünsch, 2006: Grace observations of changes in continental water storage. *Global nd Planetary Change*, **50**, 112–126, doi:10.1016/j.gloplacha.2004.11.018.

Schuh, H., S. Nagel, and T. Seitz, 2001: Linear drift and periodoc variations observed in long time series of polar motion. *J. Geodesy*, **74**, 701–710.

Solomon, S., D. Qin, M. Manning, R. Alley, T. Berntsen, N. Bindoff, Z. Chen, A. Chidthaisong, J. Gregory, G. Hegerl, M. Heimann, B. Hewitson, B. Hoskins, F. Joos, J. Jouzel, V. Kattsov, U. Lohmann, T. Matsuno, M. Molina, N. Nicholls, J. Overpeck, G. Raga, V. Ramaswamy, J. Ren, M. Rusticucci, R. Somerville, T. Stocker, P. Whetton, R. Wood, and D. Wratt, 2007: *Climate Change 2007: The Physical Science Basis. Contribution of Working Group I to the Fourth Assessment Report of the Intergovernmental Panel on Climate Change*, Cambridge University Press, chapter Technical Summary.

Song, Y. T. and V. Zlotnicki, 2007: Subpolar ocean-bottom-pressure oscillation and its links to the tropical ENSO. *Intl. J. Remote Sensing*.

Talley, L. D., 2003: Shallow, intermediate, and deep overturning components of the global heat budget. *J. Phys. Oceanogr.*, **33**, 530–560.

Tapley, B. D., S. Bettadpur, J. R. Ries, P. F. Thompson, and M. M. Watkins, 2004: GRACE measurements of mass varaibility in the Earth system. *Science*, **305**, 503–505.

Thompson, D. J., 1982: Spectrum estimation and harmonic analysis. *IEEE Proc*, volume 70, 1055–1056.

Thorpe, A. J., J. M. Gregory, T. C. Johns, R. A. Wood, and J. F. B. Mitchell, 2001: Mechanisms determining the Atlantic thermohaline circulation response to greenhouse gas forcing in a non-flux-adjusted coupled climate model. *J. Climate*, **14**, 3102–3116.

Trenberth, K. E., 1984: Some effects of finite sample size and persistence in meteorological statistics. part i: autocorrelations. *Monthly Waether Review*, **112**, 2359–2368.

— 1997: The definition of El Niño. *Bull. Amer. Meteor. Soc.*, **78**, 2771–2777.

Trenberth, K. E., G. W. Branstator, D. Karoly, A. Kumar, N.-C. Lau, and C. Ropelewski, 1998: Progress during TOGA in understanding and modeling global teleconnections associated with tropical sea surface temperatures. *J. Geophys. Res.*, **103**, 14291–14324.

Trenberth, K. E. and J. M. Caron, 2000: The Southern Oscillation revisited: Sea level pressures, surface temperatures, and precipitation. *J. Climate*, **13**, 4358–4365.

Trenberth, K. E., J. M. Caron, D. P. Stepaniak, and S. Worley, 2002: The evolution of ENSO and global atmospheric surface temperatures. *J. Geophys. Res.*, **107**, doi:10.1029/2000JD000298.

Trenberth, K. E., D. P. Stepaniak, and L. Smith, 2005: Interannual variability of patterns of atmospheric mass distribution. *J. Climate*, **18**, 2812–2825.

Vinogradova, N. T., R. M. Ponte, and D. Stammer, 2007: Relation between sea level and bottom pressure and the vertical dependence of oceanic variability. *Geophys. Res. Lett.*, **34**, L03608, doi:10.1029/2006GL028588.

von Storch, H. and F. W. Zwiers, 1999: *Statistical Analysis in Climate Research*. Cambridge University Press.

Wahr, J., M. Molenaar, and F. Bryan, 1998: Time variability of the earth's gravity field: hydrological and oeanic effects and their possible detection using GRACE. *J. Geophys. Res.*, **103**, 30205–30229.

White, N. J., J. A. Church, and J. M. Greogory, 2005: Coastal and global averaged sea level rise for 1950 to 2000. *Geophys. Res. Lett.*, **32**, L01601.

Whitworth, T., W. D. Nowlin, and S. J. Worley, 1982: The net transport of Antarctic Circumpolar Current through Drake Passage. *J. Phys. Oceanogr.*, **12**, 960–971.

Willis, J. K., D. Roemmich, and B. Cornuelle, 2004: Interannual variability in upper ocean heat content, temperature, and thermosteric expansion on global scales. *J. Geophys. Res.*, **109**, C12036, doi:10.1029/2003JC002260.

Wilson, C. R., 1993: Contributions of water mass redistribtuion to polr motion excitation. *Contributions of Space Geodesy to Geodynamics: Earth Dynamics*, D. L. Turcotte and D. E. Smith, eds., American Geophysical Union, volume 24 of *Geodynamics Series*, 77–82.

Wunsch, C. and D. Stammer, 1997: Atmospheric loading and the oceanic 'inverted barometer' effect. *Rev. Geophys.*, **35**, 79–107.

— 1998: Satellite altimetry, the marine geoid, and the oceanic general circulation. *Ann. Rev. Earth Planet. Sci.*, **26**, 219–253.

Acknowledgements

Before anyone else, I thank Jochem Marotzke for showing me how to do science. With his constant and encouraging, yet challenging support, I enjoyed the great freedom to do exciting research, not to mention invaluable side projects along the way.

Many thanks go to Johann Jungclaus, who supported my work with valuable inspiring comments and suggestions, and essential help with numerous scientific and technical issues. I very much appreciate his encouraging and open-minded interest in my work.

During the last three years, I have benefited from professional and moral support from Helmuth Haak, Johanna Baehr, Jin Song von Storch, Ernst Maier-Reimer, Uwe Mikolajewicz, Erich Roeckner, Wolfgang Müller, Stefan Hagemann, Michael Botzet, Micheal Boettinger, Monika Esch, Daniela Jacob and many others, who cannot all be listed here.

I am grateful to all my colleagues who endured my (more or less) scientific screed during the weekly group meetings. Their comments and suggestions are highly appreciated. Special thanks go to Dirk Notz for providing the 'stress release tool' in his office, and for helping to both keep faith in and a critical distance to the science that we do.

I am also grateful to Antje Weitz, Kornelia Müller and Cornelia Kampmann for their organizational backup.

The CIS group, library and administration staff provided invaluable assistance.

I am deeply indebted to my mother and my grandparents for their absolute and constant support throughout the years.

Birthe and Anton have been the most precious joy during the last three years. Thank you for being there.

Publikationsreihe des MPI-M
„Berichte zur Erdsystemforschung“ , „*Reports on Earth System Science*“, ISSN 1614-1199
Sie enthält wissenschaftliche und technische Beiträge, inklusive Dissertationen.

Berichte zur Erdsystemforschung Nr.1 Juli 2004	**Simulation of Low-Frequency Climate Variability in the North Atlantic Ocean and the Arctic** Helmuth Haak
Berichte zur Erdsystemforschung Nr.2 Juli 2004	**Satellitenfernerkundung des Emissionsvermögens von Landoberflächen im Mikrowellenbereich** Claudia Wunram
Berichte zur Erdsystemforschung Nr.3 Juli 2004	**A Multi-Actor Dynamic Integrated Assessment Model (MADIAM)** Michael Weber
Berichte zur Erdsystemforschung Nr.4 November 2004	**The Impact of International Greenhouse Gas Emissions Reduction on Indonesia** Armi Susandi
Berichte zur Erdsystemforschung Nr.5 Januar 2005	**Proceedings of the first HyCARE meeting, Hamburg, 16-17 December 2004** Edited by Martin G. Schultz
Berichte zur Erdsystemforschung Nr.6 Januar 2005	**Mechanisms and Predictability of North Atlantic - European Climate** Holger Pohlmann
Berichte zur Erdsystemforschung Nr.7 November 2004	**Interannual and Decadal Variability in the Air-Sea Exchange of CO2 - a Model Study** Patrick Wetzel
Berichte zur Erdsystemforschung Nr.8 Dezember 2004	**Interannual Climate Variability in the Tropical Indian Ocean: A Study with a Hierarchy of Coupled General Circulation Models** Astrid Baquero Bernal
Berichte zur Erdsystemforschung Nr9 Februar 2005	**Towards the Assessment of the Aerosol Radiative Effects, A Global Modelling Approach** Philip Stier
Berichte zur Erdsystemforschung Nr.10 März 2005	**Validation of the hydrological cycle of ERA40** Stefan Hagemann, Klaus Arpe and Lennart Bengtsson
Berichte zur Erdsystemforschung Nr.11 Februar 2005	**Tropical Pacific/Atlantic Climate Variability and the Subtropical-Tropical Cells** Katja Lohmann
Berichte zur Erdsystemforschung Nr.12 Juli 2005	**Sea Ice Export through Fram Strait: Variability and Interactions with Climate**- Torben Königk
Berichte zur Erdsystemforschung Nr.13 August 2005	**Global oceanic heat and fresh water forcing datasets based on ERA-40 and ERA-15** Frank Röske
Berichte zur Erdsystemforschung Nr.14 August 2005	**The** HAM**burg** O**cean** C**arbon** C**ycle Model HAMOCC5.1 - Technical Description Release 1.1** Ernst Maier-Reimer, Iris Kriest, Joachim Segschneider, Patrick Wetzel
Berichte zur Erdsystemforschung Nr.15 Juli 2005	**Long-range Atmospheric Transport and Total Environmental Fate of Persistent Organic Pollutants - A Study using a General Circulation Model** Semeena Valiyaveetil Shamsudheen

Publikationsreihe des MPI-M
„Berichte zur Erdsystemforschung“ , „*Reports on Earth System Science*“, ISSN 1614-1199
Sie enthält wissenschaftliche und technische Beiträge, inklusive Dissertationen.

Berichte zur Erdsystemforschung Nr.16 Oktober 2005	**Aerosol Indirect Effect in the Thermal Spectral Range as Seen from Satellites** Abhay Devasthale
Berichte zur Erdsystemforschung Nr.17 Dezember 2005	**Interactions between Climate and Land Cover Changes** Xuefeng Cui
Berichte zur Erdsystemforschung Nr.18 Januar 2006	**Rauchpartikel in der Atmosphäre: Modellstudien am Beispiel indonesischer Brände** Bärbel Langmann
Berichte zur Erdsystemforschung Nr.19 Februar 2006	**DMS cycle in the ocean-atmosphere system and its response to anthropogenic perturbations** Silvia Kloster
Berichte zur Erdsystemforschung Nr.20 Februar 2006	**Held-Suarez Test with ECHAM5** Hui Wan, Marco A. Giorgetta, Luca Bonaventura
Berichte zur Erdsystemforschung Nr.21 Februar 2006	**Assessing the Agricultural System and the Carbon Cycle under Climate Change in Europe using a Dynamic Global Vegetation Model** Luca Criscuolo
Berichte zur Erdsystemforschung Nr.22 März 2006	**More accurate areal preciption over land and sea, APOLAS Abschlussbericht** K. Bumke, M. Clemens, H. Graßl, S. Pang, G. Peters, J.E.E. Seltmann, T. Siebenborn, A. Wagner
Berichte zur Erdsystemforschung Nr.23 März 2006	**Modeling cold cloud processes with the regional climate model REMO** Susanne Pfeifer
Berichte zur Erdsystemforschung Nr.24 Mai 2006	**Regional Modeling of Inorganic and Organic Aerosol Distribution and Climate Impact over Europe** Elina Marmer
Berichte zur Erdsystemforschung Nr.25 Mai 2006	**Proceedings of the 2nd HyCARE meeting, Laxenburg, Austria, 19-20 Dec 2005** Edited by Martin G. Schultz and Malte Schwoon
Berichte zur Erdsystemforschung Nr.26 Juni 2006	**The global agricultural land-use model KLUM – A coupling tool for integrated assessment** Kerstin Ellen Ronneberger
Berichte zur Erdsystemforschung Nr.27 Juli 2006	**Long-term interactions between vegetation and climate -- Model simulations for past and future** Guillaume Schurgers
Berichte zur Erdsystemforschung Nr.28 Juli 2006	**Global Wildland Fire Emission Modeling for Atmospheric Chemistry Studies** Judith Johanna Hoelzemann
Berichte zur Erdsystemforschung Nr.29 November 2006	**CO_2 fluxes and concentration patterns over Eurosiberia: A study using terrestrial biosphere models and the regional atmosphere model REMO** Caroline Narayan

Publikationsreihe des MPI-M
„Berichte zur Erdsystemforschung“ , „*Reports on Earth System Science*“, ISSN 1614-1199
Sie enthält wissenschaftliche und technische Beiträge, inklusive Dissertationen.

Berichte zur Erdsystemforschung Nr.30 November 2006	**Long-term interactions between ice sheets and climate under anthropogenic greenhouse forcing Simulations with two complex Earth System Models** Miren Vizcaino
Berichte zur Erdsystemforschung Nr.31 November 2006	**Effect of Daily Surface Flux Anomalies on the Time-Mean Oceanic Circulation** Balan Sarojini Beena
Berichte zur Erdsystemforschung Nr.32 November 2006	**Managing the Transition to Hydrogen and Fuel Cell Vehicles – Insights from Agent-based and Evolutionary Models –** Malte Schwoon
Berichte zur Erdsystemforschung Nr.33 November 2006	**Modeling the economic impacts of changes in thermohaline circulation with an emphasis on the Barents Sea fisheries** Peter Michael Link
Berichte zur Erdsystemforschung Nr.34 November 2006	**Indirect Aerosol Effects Observed from Space** Olaf Krüger
Berichte zur Erdsystemforschung Nr.35 Dezember 2006	**Climatological analysis of planetary wave propagation in Northern Hemisphere winter** Qian Li
Berichte zur Erdsystemforschung Nr.36 Dezember 2006	**Ocean Tides and the Earth’s Rotation - Results of a High-Resolving Ocean Model forced by the Lunisolar Tidal Potential** Philipp Weis
Berichte zur Erdsystemforschung Nr.37 Dezember 2006	**Modelling the Global Dynamics of Rain-fed and Irrigated Croplands** Maik Heistermann
Berichte zur Erdsystemforschung Nr.38 Dezember 2006	**Monitoring and detecting changes in the meridional overturning circulation at 26°N in the Atlantic Ocean- The simulation of an observing array in numerical models** Johanna Baehr
Berichte zur Erdsystemforschung Nr.39 Februar 2007	**Low Frequency Variability of the Meridional Overturning Circulation** Xiuhua Zhu
Berichte zur Erdsystemforschung Nr.40 März 2007	**Aggregated Carbon Cycle, Atmospheric Chemistry, and Climate Model (ACC2) – Description of the forward and inverse modes –** Katsumasa Tanaka, Elmar Kriegler
Berichte zur Erdsystemforschung Nr.41 März 2007	**Climate Change and Global Land-Use Patterns — Quantifying the Human Impact on the Terrestrial Biosphere** Christoph Müller
Berichte zur Erdsystemforschung Nr.42 April 2007	**A Subgrid Glacier Parameterisation for Use in Regional Climate Modelling** Sven Kotlarski

Publikationsreihe des MPI-M
„Berichte zur Erdsystemforschung“ , „*Reports on Earth System Science*“, ISSN 1614-1199
Sie enthält wissenschaftliche und technische Beiträge, inklusive Dissertationen.



ISSN 1614-1199